The Pennsylvania State University

The Graduate School

Department of Energy and Geo-Environmental Engineering

STUDY OF STRUCTURAL TRANSFORMATIONS

AND

HYDROGEN EVOLUTION FROM BALL MILLED COALS

A Thesis in

Energy and Geo-Environmental Engineering

by

Apurba Sakti

Submitted in Partial Fulfillment
of the Requirements
for the Degree of

Master of Science

May 2008

The thesis of Apurba Sakti was reviewed and approved* by the following:

Angela Lueking
Assistant Professor of Energy and Geo-Environmental Engineering
Thesis Adviser

Caroline E. Burgess Clifford
Senior Research Associate
EMS (Earth and Mineral Sciences) Energy Institute

Semih Eser
Professor of Energy and Geo-Environmental Engineering

Yaw D. Yeboah
Professor of Energy and Geo-Environmental Engineering
Head of the Department of Energy and Geo-Environmental Engineering

* Signatures are on file in the Graduate School

ABSTRACT

To realize the hydrogen economy will call for significant developments in hydrogen production and storage. The focus of this research was to further investigate the reactive ball milling process developed by Lueking et al. for combined hydrogen production, storage, and nano-crystalline diamond (NCD) formation [1]. This work investigates the role of metals in the structural evolution of carbon during the process, including the formation of NCD, and the role of the carbon precursor in the structural transformations and hydrogen evolution characteristics.

Buck Mountain anthracite (BMT) coal, demineralized BMT (DBMT), DBMT with added iron, and DBMT with added stainless steel were used to explore the role of metals in structural transformations and NCD formation. In each case, the coal was milled with cyclohexene in a stainless steel planetary mill. After milling, select samples were annealed at 1673 K; both as-milled and annealed samples were treated with 4M HCl followed by 10 M NaOH. Temperature programmed oxidation (TPO), X-ray diffraction (XRD) and ultra-violet Raman (UVR) probed carbon structure, metal content, and metal-carbon interactions. The results clearly show that metal is introduced during milling due to attrition of the stainless steel milling components. Introduced metal is converted to carbides during the thermal anneal, carbon is graphitized, and metals become encapsulated in carbon. The 4 M HCl treatment leads to further changes in the carbon structure, and this is more pronounced when the thermal anneal is omitted. The 10 M NaOH treatment leads to changes in the carbon structure. With the thermal anneal, the 10 M NaOH treatment leads to the formation of both more and less ordered carbon fractions and reduces the amount of iron carbide. The results support the hypothesis that iron carbide plays a key role in the formation of NCD. Evidence for a NCD vibration in UVR is found in one sample.

Secondly, Demineralized Summit (DS) anthracite coal, before and after a thermal anneal at 1673 K (DS-HT), along with graphite, were used to assess the role of precursor order on structural transformations induced by reactive ball milling. Along with TPO, XRD, and UVR, helium density, solvent swelling, and nitrogen adsorption were used to assess structural transformations of the carbons with milling. Reactive ball milling of

graphite led to a decrease in crystallite dimensions, the formation of amorphous carbon, and increased surface area made up primarily of mesoporous carbon. Milled graphite exhibited solvent swelling, an indication of a three-dimensional networked structure. The least ordered precursor, DS, had no evidence of amorphous carbon after milling in TPO analysis. XRD indicated milling DS increased the in-plane crystallite size and led to the formation of a 'gamma-phase' which was not evident in the other materials. UVR indicated an increased sp^2 clustering upon milling of DS, an effect which was not observed for the other materials. Milling of DS led to the most significant increase in N_2 BET surface area, and the pores were microporous in nature. Annealing DS prior to milling increased the metal input during milling, and led to structural changes of the carbon that resembled those of graphite. Additional studies suggested milling time and cyclohexene addition had little effect on structural transformation relative to carbon precursor and synthesis sequence. Thermo-gravimetric mass spectrometry (TGMS) of the materials confirmed cyclohexene dehydrogenation during milling, similar to previous studies. Only milled DS exhibited low temperature hydrogen evolution after extended storage, and the total hydrogen evolution from milled DS exceeded that of milled graphite.

TABLE OF CONTENTS

List of Figures

List of Tables

Acknowledgements

First and foremost, I would like to thank my advisor Dr. Angela Lueking for her invaluable guidance and support. I would then like to thank Dr. Caroline Clifford for being a great mentor and for her support and encouragement at times when they mattered most. My sincere thanks to Dr. Semih Eser for being in my committee and for his expert guidance on policy related issues.

I would like to thank Dr. Jonathan Matthews and Dr. John V. Badding for their expert advice.

I would also like to thank Nichole Wonderling and Magda Salama of the Materials Research Institute and Gareth Mitchell, Glenn Decker, Ronnie Wasco and Ronald Wincek from the Energy Institute for their invaluable technical support and advice.

Special thanks to Dania Fonseca, Humberto Rodriguez Gutierrez, Deepa Narayanan and Kofi Adu for their great support and encouragement. It was invaluable. I would also like to thank Qixiu Li for her help when I was making the final edits to the thesis from Hungary.

I cannot but think of my awesome friends now who have been there every step of my way and made this two years so memorable. I would like to thank Gustavo Lascano, Ojogbane Achimugu, Daniel Van Niekerk, Meredith Hill Bembenic, Narasimhan Soundarrajan, Pradeep Indrakanti and Brandie Markley. To Megan, thank you for being there for me and for your understanding and support.

To my brother Amlan, your support and encouragement was invaluable. You have been a great source of inspiration. Lastly, to my parents who are the reason why I am. I shall be forever indebted to them.

Chapter 1

Introduction and Scope of the Research

Introduction

The transportation sector is a major driver of the petroleum dependence of the United States, accounting for roughly two-thirds of the twenty million barrels of oil used in the U.S. per day. In 2005, U.S. imported 55% of its oil [2]. This is expected to grow to 61% by the year 2030 under a status quo scenario [2]. For a reduction in this dependence on imported oil, a host of strategies are under consideration including gasoline hybrid, fuel cell powered and battery operated electric vehicles. However in the long term, petroleum substitution is required that calls for the development of alternate energy carriers. Hydrogen is considered to have the potential to be an attractive alternative energy carrier particularly for the transportation sector [3-5]. The hydrogen economy, in which energy is stored and transported as hydrogen is often projected as the ultimate solution to the problems associated with the usage of fossil fuels. However for it to be realized, much development is needed in areas like hydrogen production and hydrogen storage.

The following is a discussion on the 'Science, Technology and Society (STS)' viewpoints for research contributing to the development of a hydrogen economy followed by the technical status and challenges facing its implementation. The STS perspective has been added to fulfill the requirements for a Minor in Science Technology and Society.

A STS perspective

STS or the study of how social, political, and cultural values affect scientific research and technological innovation, and how these in turn affect society, politics, and culture go a long way in determining effective research policies. The following is to address the STS concern over the direction of the research work presented in this thesis and the manner in which it will prove beneficial.

Clean forms of energy are needed to support sustainable global economic growth while mitigating impacts on air quality and the potential effects of greenhouse gas emissions. As mentioned above, a hydrogen economy is considered amongst the forerunners in the search for a clean energy source. Amongst the key drivers for hydrogen based energy system are energy security (e.g. oil dependency), environmental quality (e.g. carbon emissions) and international competitiveness.

The issue of energy security is based on the fact that most of the countries are net importers of energy resources like petroleum and hence are dependent on other countries. Petroleum supplies, on which the transportation sector is heavily dependent globally, will be in increasingly higher demand as highly populated developing countries expand their economies and become more energy intensive. For countries like the U.S., the development and realization of a hydrogen economy will facilitate the non-dependence on other countries for petroleum since hydrogen can be generated from diverse domestic sources.

The concern of the effects of indiscriminate usage of conventional energy sources on the environment is a major issue worldwide. The quality of air is also a cause of concern. Personal vehicles and electric power plants are significant contributors to air quality problems [6]. The introduction of hydrogen based vehicles for public transportation and an enhancement in the quality of service can be an approach to improve air quality. This is because with the right infrastructure for services to support hydrogen based public transportation system it will be able to compete with the available technologies. This will lead to a lesser reliance on personal vehicles. The production of hydrogen from coal and other fossil fuel sources for use in the aforesaid scenarios will produce emissions but since they will be from a central location instead from distributed sources, the capture and sequestration will be relatively easier.

The economic stakes in the development of alternative energy sources like hydrogen and fuel cells are high. Total revenues for publicly traded companies in the global fuel cell sector were up 20% to $266 million in 2005 compared to $221 million the previous year, according to the findings of the PricewaterhouseCoopers *2006 Fuel Cell Industry Survey* [7]. Since 2003, revenues have exceeded spending on research and

development [7]. In future this trend is expected to continue. Hence this is a sector where investments will bring back greater returns.

Taking the aforesaid factors into consideration namely the need to invest in alternative energy research and development and also the increasing returns on the investments it can be said that the right background for the development of cleaner energy technologies exist. Though considered a forerunner, a hydrogen economy is not guaranteed to be successful and better options can arise for addressing issues like carbon emissions and oil dependency. It is hence important that research and development is conducted to determine whether or not a hydrogen economy can be realized technically,

Technical Status and Challenges

To be accepted widely as a transportation fuel, hydrogen must match the price, refueling ease, and safety of current fuels. The challenges faced by a transition to a hydrogen economy are the lack of a hydrogen infrastructure and the substantial costs in production, storage, distribution and usage of hydrogen. To compete with current benchmarks, hydrogen storage targets set by the US Department of Energy (DOE) are to attain 6.0 weight % (i.e. 2 kWh/kg) by 2010 at an operating temperature of 243 K to 323 K and a delivery pressure below 100 bar [8]. Centralized hydrogen production methods currently in use are limited by an inefficient means to transport hydrogen to its point of use. Compressed and cryogenic storage methods do not meet density targets and incremental advances in candidate solid-state storage materials are not likely to meet density or cost targets (Figure 1- 1).

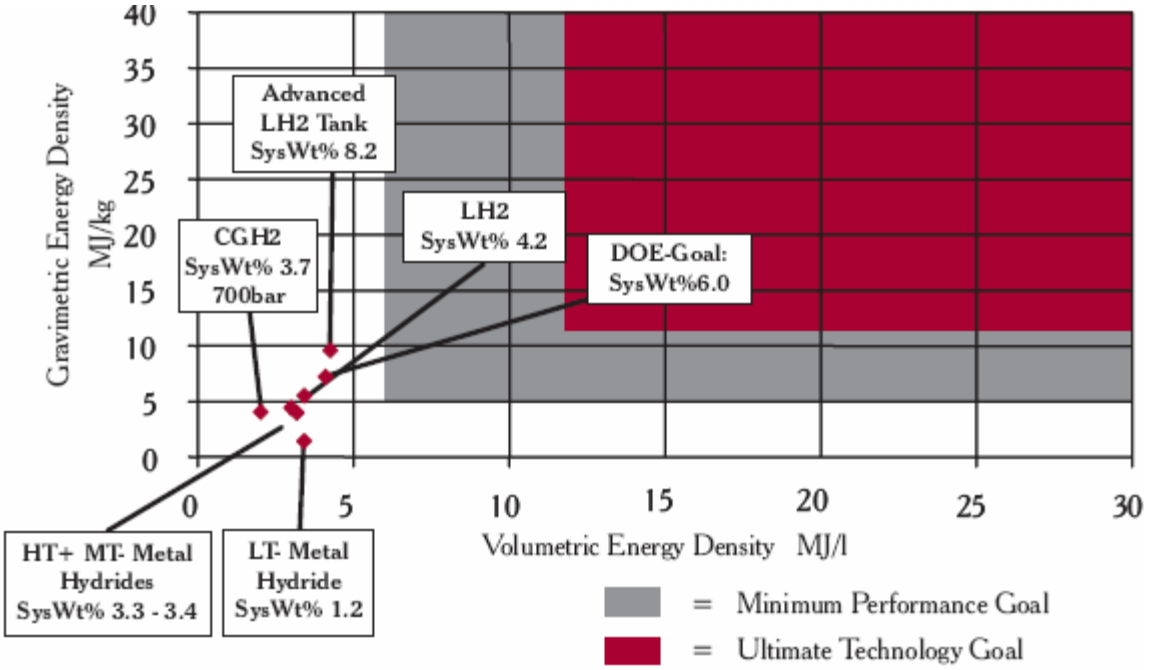

(a)

Figure 1- 1: DOE hydrogen storage goals for fuel cell applications. Abbreviations are as follows: LH2 is liquid hydrogen; CGH2 refers to cryogenic gaseous liquid hydrogen; HT refers to high temperature; MT refers to medium temperature; LT refers to low temperature. SysWt % refers to system weight percent of hydrogen and includes mass of the container and auxiliary equipment. *(Source – U.S. DOE National Hydrogen Energy Roadmap, 2002)[8]*

For all hydrogen production processes, there is a need for significant improvement in plant efficiencies, for reduced capital costs and better reliability. The commercial cost target for hydrogen production is 0.30 USD/kg H_2, corresponding to an energy price for gasoline of 2.5 USD/GJ in a competitive market [9]. Distributed hydrogen production based on reforming is often competitive with water electrolysis, as reforming costs 16-29 USD/GJ and electrolysis costs 20-40 USD/GJ, depending on investment and energy costs. In large-scale production plants based on natural gas, the production cost can be as low as 5-8 USD/GJ. However, distributed hydrogen production can be competitive with this centrally produced hydrogen depending on the transportation distance since transporting compressed hydrogen gas for 100 miles can add 15-20 USD/GJ to the cost [9].Other methods for hydrogen production include production from

biomass, photo-electrolysis, photo-biological processes and high temperature processes. However these need significant advances to prove economical even on a large scale.

Materials based hydrogen storage techniques include, metal hydrides, chemical hydrides and carbon based materials including metal-organic frameworks. Metal hydrides have a high volumetric storage density at moderate temperatures and low pressures. However, metal hydrides do not meet DOE storage goals and are inherently limited by the stoichiometry of the particular metal or metal alloy. Light-element metal hydrides are of interest for mobile applications, in order to minimize the overall gravimetric storage density of the hydride. An example of a light-element hydride is magnesium hydride, which has 7.6 wt% uptake of hydrogen based on its stoichiometry (for every magnesium atom, two hydrogen atoms are stored, leading to the stoichiometric formula MgH_2) [10]. However, the high thermal stability of magnesium hydride requires temperatures in excess of 570 K for hydrogen release, a temperature well above the DOE goal for mobile applications. Other challenges include the enhancement of the adsorption-desorption kinetics of charge and improving upon the susceptibility to contaminants which reduces the hydrogen uptake [10]. Carbon based adsorbents such as single walled nanotubes (SWNT) have been reported to have a storage potential of 5-10 wt% hydrogen on extrapolation based on SWNT purity [11]. Hydrogen storage in Graphite Nanofibers (GNF) and Multi-Wall Nanotubes (MWNT) too has been widely researched.

Another type of material considered for hydrogen storage is metal-carbon materials. Metals are often used to catalyze formation of the carbon nanomaterials, and may not be completely removed from the system. Several studies have indicated hydrogen uptake is reproducible only when metal is introduced [12] or not completely removed [13, 14] from the carbon material prior to hydrogen uptake measurements. Metal-carbon materials may also be synthesized via ball milling.

The focus of this research is to address hydrogen production and storage technologies, thereby contributing to the general field of utilizing hydrogen as an alternative energy source. The work explores a process reported by Lueking et al. [1], in which hydrogen is stored in a low-value anthracite coal during ball milling of the coal. Hydrogen is produced from dehydrogenation of a hydrocarbon. It has been speculated that the simultaneous hydrogen production and storage leads to novel carbon-hydrogen

interactions. A focus is also made to develop and optimize the formation of a value added carbon product, nanocrystalline diamond, that is produced by the structural transformation of the anthracite coal upon ball milling and subsequent treatment steps, as reported by Lueking et al. [1]. This was intended to further the understanding and determine the practical applicability of the entire process. The possibility of co-producing nano-diamond offered significant promise of boosting the economics of the whole process upon optimization. Lueking et al. developed a combined hydrogen production and storage process [1] through ball milling that utilized a low cost carbon precursor that slowly evolved hydrogen at room temperature [1, 15]. The evolution of the trapped hydrogen observed was said to be kinetically-limited based on evidence that H_2 evolution continued in excess of one year and accelerated hydrogen evolution being observed at modestly higher temperatures. A parallel observation of a nanocrystalline diamond (NCD) by-product suggested the pathway of hydrogenative ball milling leading to a hydrogenated tetrahedral carbon form that rearranges to more stable crystalline carbon forms upon heating.

The current research seeks to explore further the aforesaid process to understand the structural transformations and the evolution of hydrogen.

Scope of Research

The scope of this research was twofold and was hence divided into two projects with separate objectives:

Project 1: Structural Transformations with Ball Milling

For the first project, structural transformations leading to the formation of nano-diamond were explored. The hypothesis for this project was the sequence of reactions (shown below) as stated by Jain [16].

$$FeC\ (s) + HCl\ (aq) \rightarrow \text{no reaction (of Fe)}$$

$$xFeC\ (s) + yNaOH\ (aq) \rightarrow zFe_2O_3/Fe_3O_4(s) + xC\ (s) + y/2H_2O + yNa^+\ (aq)$$

[1] Patent Pending

$$C\ (s) \xrightarrow{HCl\ /\ NaOH} C\ (amorphous) + C\ (crystalline)$$

Subsequently the metal content in the ball milled samples were varied and the samples were characterized after the acid and base treatment. This was done to determine the structural changes occurring and to check for the formation of nano-diamond. The results of this study have been discussed in Chapter 4.

Project 2: Structural Transformations and Hydrogen Evolution

For this project the structural changes as well as the evolution of hydrogen from the samples were studied to test the following hypotheses:

a) The degree of order (and its susceptibility to change) in the precursor carbon structure affects hydrogen storage and trapping.
b) Ball Milling leads to changes in the carbon structure.
c) Ball milling with cyclohexene facilitates the structural changes due to the reaction of cyclohexene with the coal.

As such the objective of the research work was:

To explore the process parameters that effect the carbon-hydrogen structures and the hydrogen evolution via reactive ball milling. The process parameters to be explored were the carbon structure of the precursor and the susceptibility of the carbon precursor to rearrangement upon thermal or mechanical processing. .

The samples prepared as well as the series of characterizations that were performed to test the aforesaid have been discussed in Chapter 5.

Chapter 2

Literature Review

Ball milling of carbon materials has been used as a strategy to produce carbon-based hydrogen storage materials[17-20]. One route, recently reported by Lueking *et al.* resulted in hydrogen production and storage in the samples and caused structural changes leading to the formation of nano-crystalline diamond (NCD) on further processing [1]. The production of a value-added product has the potential to enhance the economic viability of the process. The following discussion reviews literature relevant to ball milling of carbon materials, focusing in particular on process steps, carbon precursor materials, structural transformations observed for carbon, and hydrogen storage.

Background

Ball milling

Ball milling, also commonly referred to as mechanical alloying, is used for producing different materials like fine microstructural powders [21]. Among the methods to prepare nanostructured materials, mechanical milling offers the possibility of producing nanocrystalline structures in different alloy systems. The ball-milling technique has been used to prepare various kinds of nanostructured materials, such as pure metallic elements, solid solutions and intermetallic compounds [22-24]. It has been applied to carbon based materials like graphite to study the formation of disordered carbons [25-27], in addition to the formation of curved and closed shell carbon nanostructures like carbon nanotubes and closed shell carbon nanostructures like carbon onions [23]. Tang *et al*. investigated the phase transformation of graphite upon ball milling and reported that a portion of the graphite underwent a crystal-amorphous phase transition. The amorphous carbon underwent crystallization upon heat treatment. Tang *et al.* reported the crystallization onset temperature to be ~ 677 ^{o}C and the corresponding activation energy to be 234 kJ/mole. They recommended the investigation of the effects of impurities like Co and Fe on the stabilization of the amorphous carbon formed.

By controlling the milling conditions, carbon powders with well defined morphology, surface area and crystallite size can be made. Changing the milling time and the atmosphere by introducing either a solvent or a gas during the process of milling can greatly vary the end product [28, 29]. For instance, the microstructure of natural graphite evolves very differently when ball milled in oxygen versus an inert atmosphere in a vibratory and a planetary mill [30]. Mechanically induced oxidation on the surface, probably along the edges of the graphene planes, is responsible for suppressing the fracture rate and preserving the crystallinity of natural graphite milled in oxygen [30]. Understanding this mechano-chemical process may open up a new route for the synthesis of carbonaceous materials.

Ball milling in liquid media can be classified into two categories based on the role of the liquid as either a lubricant or dispersal medium, or secondly, as a reactant [29]. In the latter case, the reactive nature of the liquid medium makes the process of ball milling a “mechano-chemical” process as opposed to dry mechanical milling. Narayanan and Lueking’s process involved reactive ball milling of anthracite coal in the presence of the solvent cyclohexene [31]. Their studies of anthracite coal and magnesium composites ground with and without a cyclohexene solvent indicated that the addition of cyclohexene increased the rate of reduction of ordered regions in the sample, evidenced by a decreased graphite [002] peak [32]. However their observation was an opposite trend compared to that of Imamura et al. [33], who found that the [002] peak in graphite disappeared more rapidly in the absence of a solvent, and attributed this to cleavage of graphite. It was suggested by Narayanan and Lueking that the opposite trend likely reflects the greater hardness of anthracites compared to graphite [31]. The solvent may have chemically reacted with coal (e.g., via a Diels–Alder reaction, free radical reaction, or hydrogen abstraction reaction), facilitating structural changes of the coal and leading to a disruption of any inherent structural order of the coal [31].

Hydrogen storage in carbon based materials

Hydrogen storage properties of carbon-based nano-structural materials, such as carbon nanotubes, carbon nanofibers, activated micro-porous carbon, and nano-structured graphite have been extensively investigated. Hydrogen interacts with solid-state materials

via absorption and/or adsorption. Absorption is the penetration of fluid into the solid phase, while adsorption is the enrichment or increase in density of a fluid on a surface. The origin of hydrogen storage in/on carbon-related materials can be due to the van der Waals interaction (physisorption, binding energy with ~0.1 eV), or from covalent C-H interaction (chemisorption, binding energy more than 2-3 eV). For physisorption, the binding energy increases in very narrow pores. At high relative pressures, physisorption generally occurs as a multilayer [32, 34]. Unlike physisorption, a chemisorbed molecule is linked to the reactive parts of the surface and is necessarily confined to a monolayer. Reduced C-H binding energies may originate from reconstruction and/or defect-formation in graphite [35-37]. This 'defect mediated hydrogen sorption' [37] has a binding energy in between chemisorption and physisorption. 'Defect mediated hydrogen sorption' needs further experimental clarification as to the exact nature of the carbon surface-hydrogen (C-H) interaction. For example, Browning et al. [38] claim that at 298 K only 80 % of the adsorbed hydrogen (3.5% - 6.5% uptake) could be desorbed. The high adsorption temperature, combined with the hysteresis, suggests the presence of chemisorption. On the other hand, Darkrim et al. [39] have found that adsorption of hydrogen in carbonaceous materials corresponds to the amount of hydrogen adsorption which takes place near the carbon surface solid only due to the physical forces (*viz*. van der Waal's forces) and therefore could only be physisorption. Thus, the actual nature and potential of chemisorbed hydrogen to carbon is unresolved.

Ball milling and hydrogen storage

Orimo et al. ball milled graphite in high pressure (10 bar) hydrogen to prepare a nanostructured carbon sample with an overall hydrogen content of 7.4% by weight ($CH_{0.95}$) measured through oxygen-combustion hydrogen analysis [40]. Temperature Desorption Spectroscopy (TDS) showed that the hydrogen evolved at 650 and 950 K. Based on complementary neutron diffraction studies, Orimo attributed the hydrogen evolution at 650 K to hydrogen stored between the graphite layers and the hydrogen evolution at 950 K to hydrogen chemically bonded to graphene edge sites. Orimo also suggested that graphite expanded to accommodate the hydrogen based on the neutron diffraction analysis and X-ray diffraction. Subsequent work by Ichikawa et al. [17]

demonstrated that the iron imparted during the milling process to be a necessary condition for the hydrogen evolution. Ichikawa's work also suggested that the carbon precursor did not affect the ultimate TDS profiles since both graphite and activated carbon showed similar behavior when milled under the same conditions. The variation of the carbon precursor has shown that there is a gradual decrease in the onset temperature of hydrogen evolution from ~600 K for graphite [41] to ~573 K for an activated carbon precursor [17] and ~ 500 K for single walled nanotubes (SWNT) [20]. In one study by Shindo et al., different precursors namely natural graphite, activated carbon fibers and activated carbon powder were milled in hydrogen atmospheres. They reported that the final product in each case was almost the same hydrogenated nanocarbon thereby suggesting its independence of the host precursor [42].

Along similar lines, Lueking et al. [1, 43] have recently published evidence of hydrogen evolution from an anthracite coal derivative, ball milled with cyclohexene. Lueking et al. did not add molecular hydrogen to the mill, but their work showed hydrogen was formed from dehydrogenation of cyclohexene within the mill. This is in line with the dehydrogenation of the milling solvent reported by Imamura et al. [44] for Mg and MgH_2 milled with cyclohexene but Lueking et al's sample evolved hydrogen even when magnesium was not added. Lueking et al. reported slow room temperature hydrogen evolution based on mass spectroscopy signal and also showed Raman vibrations that matched molecular hydrogen. The rate of hydrogen evolution increased at approximately 333 K with heating and then again at 573 K. The sample evolved 0.7-0.8% by weight hydrogen from sample loading to 573 K at ambient pressure after storage in ambient air, and 2.1% up to 1023 K. In addition to that, the observation of crystalline carbons with both sp^2 and sp^3 hybridized regions in the milled anthracite indicated that the process led to structural changes in the carbon material.

Hydrogen evolution from the samples prepared through ball milling has also been shown to be a function of the sample age. Thermogravimetric-mass spectrometry (TGMS) results reported by Lueking et al. show a greater evolution of hydrogen from the samples with lesser storage times [1]. The overall hydrogen evolution from the onset of sample heating till 750 °C was reported to be 2.1 %, 1.0% and 0.7% for the corresponding sample ages of 3, 30 and 76 days.

Anthracite Coal

Anthracites are high carbon coals, typically greater than 90% carbon, and by definition, greater than 92% fixed carbon on a dry, mineral matter free basis, with virtually all the carbon present in aromatic structures [45]. The volatile matter ranges from 2 to 8% [32, 46]. Anthracite is heterogeneous and contains amorphous material, made up of mostly aliphatic carbon and oxygen, located on the edges of the aromatic sheets [47]. The amorphous material can be a source of crosslink formation when the anthracite is heated through the formation of bonds between the aromatic sheets [48, 49].

The aromatic units are mostly in parallel orientation, and as a result the anthracites are very microporous and sub-microporous. (IUPAC classifies micropores as pores with a diameter of 8-20 Å and pores less than 8 Å as sub-microporous [50].) The fine-structured porosity of anthracites in general may facilitate higher adsorption of gas molecules with smaller kinetic diameters and may be advantageous to trap hydrogen. Anthracites also inherently contain hydrogen atoms within the structure which may be classified as organic or inorganic. Hydrogen in adsorbed water and that in mineral matter can be classified as inorganic hydrogen while hydrogen in polyaromatic hydrocarbon moiety can be termed as organic hydrogen.

Coal structure and cross-linking

The structure of coal is heterogeneous, and not well defined. Coal swells in organic solvents, exhibits elastic properties, and has a a complex, networked structure. Two network structure models widely considered are the covalent network model and the non-covalent network model (see Figure 2- 1) [51]. The covalent network model (Figure 2- 1a) also known as the “two-phase model” assumes that coal has covalently bound giant networks that are insoluble in any solvent, and relatively small amounts of solvent-soluble, low molecular weight substances are trapped in the networks. The non-covalent network (Figure 2- 1b) model also known as the “associated or the physical network model” proposes that coal consists of only coal molecules but form huge associates [51].

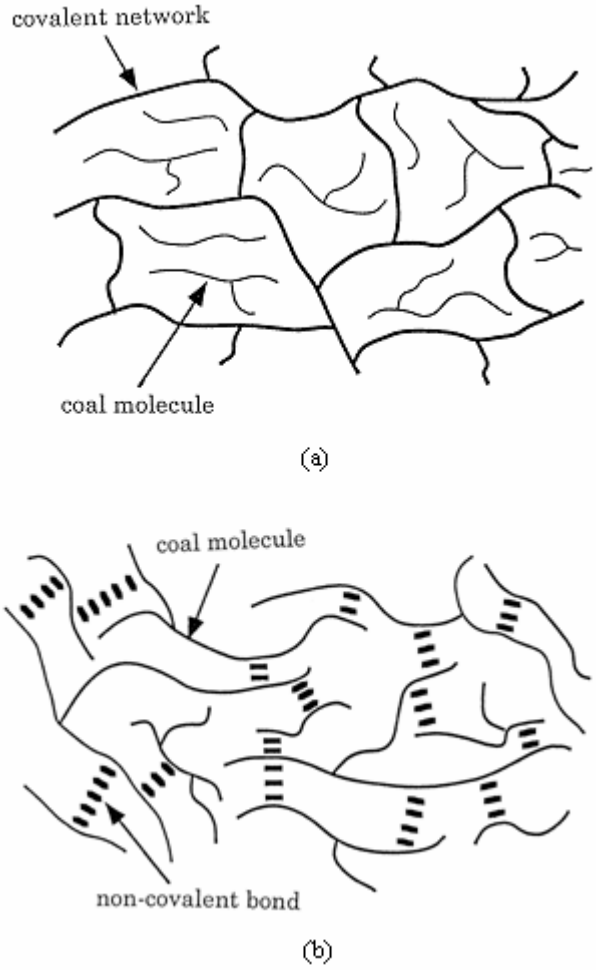

Figure 2- 1: Two widely considered network structure models of coal: covalent model (a) and non-covalent model (b) *(Source: Iino, M. Fuel Processing Technology, 2000) [51]*

In the associated structure (Figure 2- 1b), non-covalent interactions between the huge coal associates include hydrogen bonds, charge transfer interactions and $\pi - \pi$ interactions. Solvent swelling studies support the associated structure of coals rather than the covalent cross-link model [51]. The studies of Takanohashi et al. on the solubility, molecular weight distribution, and energy minimum structure of coal support an associated structure model [52]. However most of the studies have been conducted on bituminous coals which have a relatively higher extraction yield and swelling. Anthracites have higher fixed carbon content and in general have lower swelling ratios [53].

The extent and nature of cross-linking in coal is a subject of debate within the coal literature. According to Larsen et al., crosslinking may refer to hydroxyl groups forming strong bonds to acceptors in another macromolecular chain segment. These hydrogen bonds serve as effective cross-links in the glassy macromolecular coal [54]. Cross-links in anthracite, as described by Atria, can be fragments such as a methylene group $–CH_2-$, or an ether group, $-CH_2-O-CH_2-$, which act as covalently bonded chemical connections between aromatic sheets [49]. Painter contradicted Larsen et al. by stating that for molecules in the liquid state (as was the case in Larsen et al.'s experiment) the lifetime of the hydrogen bond was too short to act as a cross-link [55]. According to Larsen et al., a cross-link is a linkage that maintains its integrity during the course of a deformation experiment (e.g., swelling), thus affecting changes to the free energy by causing the interlinked segments to be displaced in such a way as to maintain a certain spatial relationship with respect to one another (i.e., there are configurational constraints relative to a non cross-linked system)[54].

The nature of the cross-links significantly influences the manner in which the coal behaves. According to van Krevelen, for a carbon to be graphitizable, there should not be strong crosslinks between the crystallites for them to be able to prevent rearrangement upon heating [56]. Figure 2- 2 shows the schematic representation by Franklin of a graphitizing (Figure 2- 2a) and a non-graphitizing (Figure 2- 2b) carbon. The graphitizing carbon (Figure 2- 2a) is characterized by the presence of pores situated between the basal planes of neighboring near-parallel crystallites. Here the process of crystallite growth consists of progressive elimination of the holes by gradual shifting of the near-parallel groups into truly parallel positions [57].

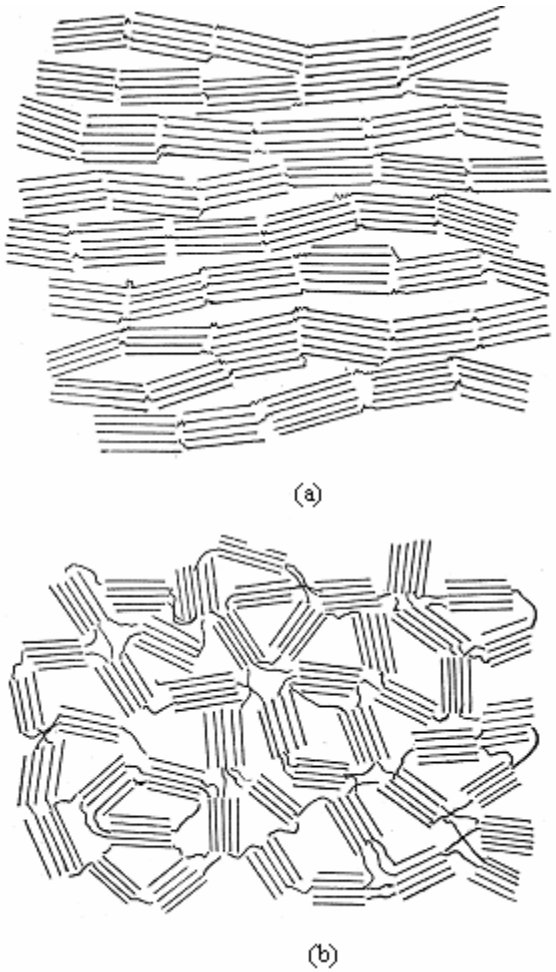

Figure 2- 2: Schematic representation of a graphitic (a) and a non-graphitic (b) coal (Source: Franklin, R.E., Proc. of the R Soc. of London, A, 1951) [57]

The non-graphitizing carbon (Figure 2- 2b) shows the strongly cross-linked system of randomly orientated crystallites, resulting in large porosity. Franklin also stated that the strong cross-linking which exists in the non-graphitizing carbons is at least partially broken down at sufficiently high temperatures [57]. In the case of anthracites, cross-linking hinders crystallite growth at temperatures below 2000 ˚C. At higher temperatures, cross-linking is destroyed crystallites reorient and unite to eliminate pores in the structure. This process is graphitization. Figure 2- 3 is a schematic representation by Franklin of a low temperature anthracite char showing the relative orientation in the structure as compared to Figure 2- 2b [57].

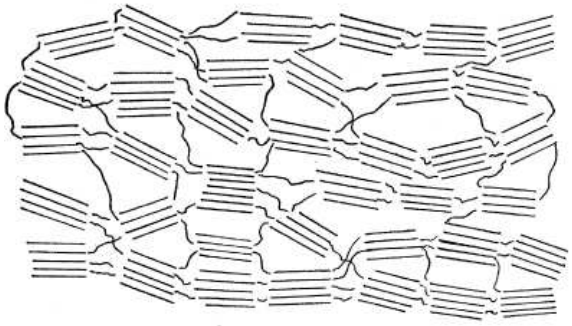

Figure 2- 3: Schematic representation of an anthracite char (Source: *Franklin, R.E., Proc. of the R Soc. of London, A, 1951*) [57]

Structural transformations and carbon crystallization on ball milling

Lueking et al. observed nano-crystalline diamond (NCD) after a four-step process: anthracite was first reactively ball milled with cyclohexene, annealed at 1400 °C, treated in 4M HCl, then treated with 10M NaOH [1]. When the thermal anneal was omitted, a crystalline carbon region was also observed after the 10 M NaOH treatment; this crystalline region was unstable and converted to NCD and carbon onions via electron irradiation in the transmission electron microscopy (TEM) [15]. Using Raman, X-ray diffraction (XRD) and temperature programmed oxidation (TPO) characterization results, Lueking et al. proposed that ball milling led to the formation of tetrahedral amorphous carbon, the thermal anneal led to iron carbide formation, and both the HCl and NaOH purification steps led to changes in the carbon structure [58].

Along similar lines, Chen et al. observed the formation of highly curved nanostructures or closed shell graphite particles upon ball-milling. Chen et al. explained this formation by the bending of the flat sp^2 graphite layers and their linking under the forces of mechanical deformation [23]. Likewise, Fecht *et al.* reported the formation of highly curled carbon nanostructures during high-energy ball-milling of graphite and attributed it to the bending due to the mechanical deformation [24]. These structures in general can be are characterized by small crystalline particles embedded in an amorphous matrix causing a high specific surface area.

Orimo *et al.* reported the formation of nanostructured graphite on ball milling in a hydrogen atmosphere and the disappearance of the long range ordering of the interlayer with increased milling time(46). The variation of the milling atmosphere from hydrogen

to argon led to a deceleration of the formation of the nanostructures as reported by Francke *et al.* A hydrogen atmosphere saturates dangling carbon bonds, stabilizing carbon nanotstructures to prevent agglomeration[59]. Nuclear magnetic resonance and Raman studies have indicated that the hydrogen can be trapped either in the graphite interlayers or chemisorbed at the dangling carbon bonds [41, 60]. The hydrogen uptake has been reported by Isobe et al. to be catalyzed by 3d metals like Fe, Ni, Co and Cu [61], amongst these Fe had the most effect. Isobe et al. suggested that the Fe_3C formed during milling plays an important role in hydrogen absorption. Their XRD data indicated that Fe contamination forms a large amount of defective sites between the graphene sheets and the covalent bonding sites. This led to an increased amount of hydrogen absorption during the milling process as observed from their thermal desorption mass spectroscopy results [61].

Summary

The reactive ball milling process also leads to unique carbon nanostructures due to the mechanochemical processing conditions. Ball milling of graphite rearranges the carbon structure and often leads to the formation of amorphous carbon. Hydrogen added to the ball milling process may stabilize dangling carbon bonds that are formed from ball milling. Carbon nanostructures formed by reactive ball milling may have advantageous properties for defect mediated hydrogen storage. The networked structure of coal may have interesting behavior in ball milling. The behavior of coal in a reactive ball milling environment is the subject of this work.

Chapter 3

Experimental Methods

Materials

A total of 6 anthracite coals: Buck Mountain PSOC-1468 (BMT), LCNN, Summit, AFM 800, AFM 2600 and PSOC 1515 and graphite were used for the two projects. PSOC 1515, Summit (S), and LCNN were supplied by the Penn State Coal Sample Bank. AFM-800 and AFM-2600 were supplied by F.B. Leopold. Graphite was supplied by Carbone.

BMT was used for Project 1, which involved investigating the structural transformations that occur during the synthesis sequence. BMT was obtained from the Pennsylvania State University coal sample bank. BMT is an anthracite coal from the bottom of the Llewellyn formation of the Buck Mountain Seam, collected from Luzerne County, Pennsylvania. The BMT has a low volatile matter content (3.65 wt%, dry) and high fixed carbon content (89.52 wt%, dry) [62]. The ash content of the coal precursor is relatively low for a naturally occurring coal (6.7%), consisting primarily of naturally occurring minerals; neutron activation analysis (NAA) of the coal precursor indicated traces of aluminum, antimony, arsenic, barium, bromine, cerium, chromium, hafnium, iron, lanthanum, magnesium, potassium, scandium and tungsten. The particle size data of the coal showed heterogeneous nature, with a broad particle size distribution ranging from 0.27 – 0.58 μm [32]

For Project 2, which probed the role of carbon precursor and milling conditions, a total of 5 anthracite coals were considered in the preliminary selection process. They included LCNN, Summit, AFM 800, AFM 2600 and PSOC 1515 (See Appendix A). Summit was chosen as a result of the coal selection process which as been described in detail in Appendix A. Summit mines a conglomeration of veins. Summit coal has been used in previous studies [63] and is a run-of-mine, or unprocessed, anthracite recovered from the Tracey vein. Summit has a relatively high volatile matter content (11.1wt%, dry) and lower fixed carbon content (71.2 wt%, dry). It has relatively higher ash (17.6%) as compared to the BMT as well as the four other coals considered in this study. Information on the other coals can be found in Appendix A.

Demineralization

The demineralization of the coals was done via a series of acid treatments as described by Bishop and Ward [64] to remove mineral matter inherent to the coal. Six grams of coal was mixed with 120 ml of 6 N hydrochloric acid (HCl) in a 300 ml Nalgene beaker. The mixture was heated at 333 K while mixing every 5 minutes for a period of 1 hour, and then the heat source was removed and it was left undisturbed for 24 hours. The acid was then decanted, the residue was centrifuged, and the acid further decanted. The residue was washed with de-ionized water till the water became neutral and then vacuum filtered using a grade 41 mesh ashless filter paper from Whatmann (Porosity: Coarse, Flow rate: Fast, Particle retention: 20-25 micrometer). To remove the iron content present in the form of pyrites (iron sulfide), this coal sample was washed in a similar procedure with 135 ml 6 N nitric acid (HNO_3). After repeating the same heating procedure with stirring as with the HCl-anthracite mixture, the acid was decanted out, centrifuged, decanted again, rinsed and filtered as in the previous case. Finally, to remove the silicon based impurities, the acid treatment was repeated with 120 ml 47 – 52% hydrofluoric acid (HF). Each acid treatment was followed by the centrifugation procedure and by multiple rinses with de-ionized water until the rinse water became neutral. Finally the sample was subjected to vacuum heating at 423 K to remove the moisture. The HCl and HNO_3 used were from Sigma Aldrich and the HF from J.T. Baker.

Processing

Ball milling was done on a Fritsch Planetary Mono Mill Pulverisette 6 LC – 106A with a 250 ml stainless steel (Fe-Cr-Ni) vessel and a set of twenty 10mm diameter stainless steel (Fe-Cr) balls. The bowl was hardened using Ni. The choice of cyclohexene as the grinding solvent was based on the previous work of Lueking et al.[1, 31]. As in the case of Lueking *et al.* the sample was carbon-rich (as defined in Narayanan and Lueking [31]). All the samples were milled for 80 hours at 400 rpm in an argon atmosphere to prevent oxidation and to minimize air exposure. The Argon used was of ultra-high pure (UHP) grade and was 99.999% pure. Cyclohexene (99 % purity) was purchased from JT Baker.

For Project 1, the iron and stainless steel (type 316) powders which were added to the samples were obtained from STREM Chemicals. For the acid and base treatments the HCl used was from Sigma Aldrich and the NaOH from J.T. Baker. De-ionized water was used to prepare the HCl of the required concentration while the NaOH was of the required concentration. The acid and base treatments were carried out for a period of 24 hours. Subsequently the acid or base (depending on the treatment) was decanted and the residue was centrifuged, and the acid further decanted. The residue was washed with de-ionized water till the water became neutral and then vacuum filtered using a grade 41 mesh ashless filter paper from Whatmann (Porosity: Coarse, Flow rate: Fast, Particle retention: 20-25 micrometer). Specific details on the preparation of the samples for the two projects have been described in the Results and Discussion chapters (4 and 5). Wherever the samples have been thermally annealed (denoted by a '-HT'), a temperature of 1400 ºC was attained and the sample was soaked at that temperature for a time period of three hours. For Project 1, the ramp rate was 2.5 ºC and for Project 2 a ramp rate of 25 ºC was used. The order of sample preparation has been documented in Appendix A. For the preparation of the samples for Project 2, a new set of stainless steel bowl and balls (as described above) was used.

Characterization

Temperature Programmed Oxidation (TPO)

TPO was performed in a Perkin Elmer 7 thermo-gravimetric analyzer (TGA) by flowing UHP grade air with a flow rate of 100cc/min. Samples (10-14 mg) were heated from 30 ^{o}C to 1000 ^{o}C with a ramp rate of 5 ^{o}C/min. TPO is plotted as the negative derivative weight vs. temperature (T). For Project 2, TPO has also been plotted as the weight % vs. T. For Project 1, the mass at room temperature is being considered as the initial mass while for Project 2 the initial mass was considered as the mass at 100 ^{o}C. This was selected under the assumption that at that temperature all loosely bound cyclohexene will be removed. The ash contents were calculated based on this mass and the final mass after the sample cooled down to negate buoyancy effects. The data was smoothed by using a forward moving average. First 10 data points were averaged and subsequently an

average of 30 of these averaged points was obtained to negate instrument noise as much as possible.

For reference, amorphous carbon oxidizes as 150 ºC [16], purified (after the removal of metals) single walled carbon nano-tubes (SWNT) oxidize at ~ 600 ºC, and graphite oxidizes at higher temperatures of ~ 850ºC when oxidized under the same conditions [16]. SWNT's oxidize at a temperature of ~ 450 ºC if metals are present in the sample [16, 65]. The temperature of oxidation of a carbon sample is generally dependent on: the temperature ramp rate, particle size, the presence of metals which may catalyze the oxidation of the carbon and the degree of ordering in the sample. More ordered carbons resembling graphite tend to have an oxidation temperature closer to the graphitic oxidation temperature. Wherever multiple sample runs have been made and the ash contents calculated for each case, the standard deviation of the ash content has been included in parentheses.

X-ray Diffraction

X Ray diffraction (XRD) was used to monitor changes in both the carbon structure and metals inherent in the coal. XRD measurements were taken with a Scintag Model X2 θ/θ goniometer with Cu radiation Ka1/Ka2 with Si (Li) Peltier detector operated at 30 kV and 50 mA. The instrument error was calculated using a standard Si sample and the necessary corrections made once every month. The relative intensities of the samples were plotted. This was done by dividing the absolute intensities of the different spectra by the same number selected on the basis of the most intense peak. The software used was Jade 8 produced by Materials Data Incorporated, Livermore, CA. The database used was ICSD and ICDD PDF4 (2006). XRD was used to characterize the different species present in the samples in Project 1. When iron carbide was identified and there was a strong fit for species of different stoichiometric ratios of iron and carbon, they have been indicated as Fe_xC_y. This was done to indicate the presence of iron carbide in different forms in the sample. For Project 2, apart from the species identification, XRD was also used to determine the crystallite sizes Lc and La; and the d spacing. Lc gives the crystallite stacking height, La gives the crystallite size (length) and d spacing represents the height between to adjacent layers of atoms in the z direction (vertical height).

For Project 2, a gamma phase associated with aliphatic side chains has been considered wherever a split was observed in the [002] peak suggesting the possibility of more than one peak presence. The peak fitting has been shown in Appendix B. Inclusion of the gamma peak leads to a decrease in the FWHM value of the [002] peak resulting in an increase of the Lc and La values. The Lc and La values have been calculated following the Scherrer Equation which is given by:

$$L_c = K\lambda / \Delta 2\phi Cos\phi \ ,$$

(where $\Delta 2\phi$ is the FWHM (in radians) of the [002] peak, λ is the X-ray wavelength, ϕ is the Bragg angle and K is a constant equal to 0.9 for Lc and 1.84 for La [66]) [67].

Surface Area and Porosity Analysis

The surface area and microporosity of the samples were measured using Micromeritics ASAP 2020 using nitrogen at 77K and a maximum manifold pressure of 925 mm Hg.The samples were degassed for at least 24 hours in vacuum prior to measurement. Adsorption measurements with N_2 at 77K were translated to surface area based on the BET equation. The porosity distribution was calculated using the original Density Functional Theory (DFT) considering slit pores.

Raman Spectroscopy

Raman spectroscopy in the ultraviolet range was done on a Renishaw inVia spectrometer with a confocal Leica DM LM microscope and a Peltier cooled RnCam dd-CCD with a frequency doubled argon laser to obtain 244 nm. At least three runs were done per sample to check for reproducibility. Analysis of peak height and full-width at half maxima (FWHM) was performed after subtracting the baseline from the spectra using the Lorentzian Peak Fitting Module of the software Origin. The chi squared value which gives a measure of the difference of the actual and fitted data values was used to determine the goodness of fit. For Project 1, the absolute intensities have been plotted in Chapter 4. This has been labeled as ‘intensity’. All graphs plotted for Project 2 in Chapter 5 have been normalized per the G peak and a high correlation coefficient was

obtained for the fits. For samples with multiple runs, the standard deviation was calculated for FWHM and I(D)/I(G) and have been included in parentheses. For Project 2, the samples had 1 exposure each for 100 seconds at 10% of the total laser power of 0.027W.

Intelligent Gravimetric Analyzer-Helium Density Analysis

Helium density measurements were performed on an Intelligent Gravimetric Analyzer (IGA) 003 (Hiden Isochema) in order to evaluate the density after high-vacuum pretreatment. The helium density however was determined over a pressure range of the equipment, 0-20 bar at 423 K, this method is a departure from the standard helium density measurement reported in the literature in which the pressure is < 1.37 bar (20 psig) [68]. Helium (UHP, 99.999%) was passed through a 3 Å zeolite trap to minimize trace moisture. After loading, samples were outgassed at high vacuum (10^{-6} mbar) at 423 K for 2.5 hours.

Thermo-Gravimetric Mass Spectrometry

Temperature programmed desorption coupled with mass spectrometry (TGMS) was used to evaluate the hydrogen introduced into the samples during the ball milling process, as described previously in parallel studies [1]. In brief, the TGMS spectra were obtained on a Thermal Gravimetric Analyzer (TGA) 2050 coupled to a Pfeiffer Thermostar GSD 301T mass spectrometer (MS). The TGA is coupled to the MS via a temperature controlled quartz capillary at 473 K and has a mass range of 1 to 300 AMU. The Chen-tron detector was used for all MS measurements. Only mass spectroscopy data is reported here. The TGMS is purged with argon at all times: reducing--but not eliminating--the trace oxygen and water in the balance. The argon was passed through a 3Å zeolite trap to minimize moisture content. Samples were loaded into the TGMS with minimal air exposure then purged for with a flow of argon (100 cc/min) to reduce residual air while monitoring the off-gassing of the material with the MS. After a 30 minute purge at 300 K the temperature was increased to 1273 K at 10 K/min. The signal was monitored during the purge as well so that no data was lost during that stage. Before each run, pressure, peak alignment and mass scale calibrations were performed for the

MS. The MS signals are assigned to hydrogen (AMU 2), methane (AMU 16), hydroxyl (OH) species (AMU 17), water (AMU 18), carbon monoxide (AMU 28), ethane (AMU 30), oxygen (AMU 32), carbon dioxide (AMU 44), benzene (AMU 78) and cyclohexene (AMU 82), although at high temperatures other evolved hydrocarbons may have peaks that match benzene and/or cyclohexene, similar to that reported for the 'exotic hydrocarbons' that are detected in time of flight spectroscopy of milled graphite by Francke et al [69]. An alumina pan was used in all measurements within this work, and alumina is not known to catalyze any suspected dehydrogenation reactions.

Solvent Swelling

The technique used for the swelling experiments is similar to the one developed by Liotta *et al.* as described by Green *et al.*[70]. The coal samples (0.03g) were take in NMR sample tubes (8mm diameter) loaded into centrifuged at 3,000 rpm for 10 minutes. The height of coal was measured. Binary solvent CS_2-NMP (Carbon Disulphide - N-Methyl Pyrolidone) solvent (10 times the amount by volume) was added, mixed and left for 24 hours. This CS_2 containing mixture was used because related extraction and swelling experiments by Iino *et al.* [53] have proved its greater ability to swell and solvate higher rank coals as is in our case. (Iino *et al.* performed their experiments on the extract residue unlike the initial coal samples in our case. Also, in their case, repeated centrifugation was performed and the results corrected for mineral matter. The samples in our case were centrifuged once and have not been corrected for mineral matter.) The swelling ratio (Q) was determined as:

$$Q = H_{final}/H_{initial}$$

Solvent swelling experiments were performed thrice on a couple of the samples (DS and DS-HT) to determine the standard deviation (shown in parenthesis) for these samples for an estimate of reproducibility of the method.

Chapter 4

Results and Discussion I: Structural Transformations with Ball Milling

Chapter Overview

The purpose of the research presented in this chapter was to investigate the structural transformations that occur in the processing conditions used by Lueking et al.[1], i.e. reactive ball milling of anthracite coal in cyclohexene, followed by thermal anneal at 1673 K, followed by a 4 M HCl treatment, followed by a 10 N NaOH treatment. Specifically, we were interested in identifying the reaction sequence/conditions that led to the formation of nano-crystalline diamond (NCD) and an unidentified crystalline carbon (UCC) structure that were reported in [1]. A previous hypothesis put forth by Lueking et al.[16] was the following reaction sequence:

$$FeC\ (s) + HCl\ (aq) \rightarrow \text{no reaction (of Fe)}$$

$$xFeC\ (s) + yNaOH\ (aq) \rightarrow zFe_2O_3/Fe_3O_4(s) + xC\ (s) + y/2H_2O + yNa^+\ (aq)$$

$$C\ (s) \xrightarrow{HCl\ /\ NaOH} C\ (\text{amorphous}) + C\ (\text{crystalline})$$

In the above sequence, the iron carbide (FeC) is introduced from attrition of the stainless steel (SS) milling components and subsequent thermal anneal. The key point in the above reaction sequence is that carbon restructures in the post-ball milling synthesis steps, both due to reactions with or catalyzed by HCl and NaOH. Further, FeC is oxidized by NaOH to form iron oxides and a solid carbon form; in previous research, NCD and UCC were observed only after the NaOH treatment, and iron oxides were evident in XRD [15]. This chapter explores the role of metals in the post-ball milling processing steps.

Experimental Design

Buck Mountain PSOC-1468 (BMT) was used as the precursor coal for this series of tests. The ball milling procedures (as outlined in Chapter 3) were varied altering the metal content and composition present in the milling process. Sample notation, representing the four variations in metal addition include: (1) mBMT refers to milled (as-

received) BMT; (2) mDBMT refers to BMT that was demineralized prior to milling (DBMT); (3) mDBMT-Fe refers to a sample in which additional iron was added to DBMT prior to the milling process; and (4) mDBMT-SS refers to a sample of DBMT in which powdered stainless steel (SS) was added prior to the milling process. All samples were prepared using 6 g of the solid (coal and added metal) and 20 ml cyclohexene. For samples with added metal (i.e. mDBMT-Fe and mDBMT-SS), 10% of the 6 g was either Fe powder or SS powder and the remaining 90% was DBMT.

After milling, samples were processed according to the procedure described in Chapter 3. Here, the 4M HCl treatment is denoted by the suffix '-A' (e.g. mBMT-A) in the sample notation, whereas the 10 M NaOH treatment with is denoted by the suffix '-B' (e.g. mBMT-AB). When a high-temperature thermal anneal (3 hours at 1673K) was included in the process, the notation 'HT' is included in the sample name. The order of the sample preparation sequence is denoted in the sample name: e.g., mBMT-HT-A represents the BMT coal ball milled under standard conditions, followed by a high-temperature thermal anneal, followed by 4 M HCl treatment. This sample preparation sequence is shown schematically in Figure 4- 1: Flow chart of the various samples processed from mBMT. The same sequence and nomenclature was used for mDBMT, mDBMT-Fe and mDBMT-SS. All samples, at each stage of processing, were characterized with temperature programmed oxidation (TPO) and X-ray diffraction (XRD). UV Raman was performed only on the AB samples to check for the presence of the tetrahedral 'T' peak or the diamond peak.

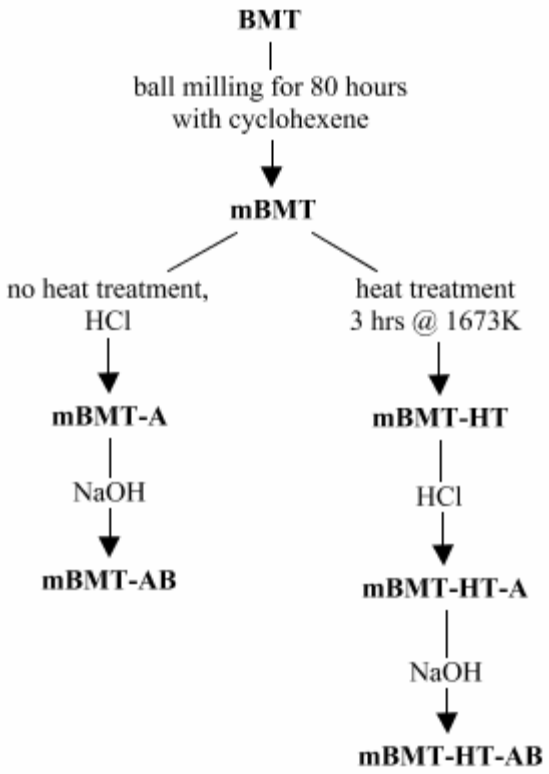

Figure 4- 1: Flow chart of the various samples processed from mBMT. The same sequence and nomenclature was used for mDBMT, mDBMT-Fe and mDBMT-SS.

Results of the mBMT series

TPO confirms a change in oxidative reactivity upon milling: BMT has a bimodal oxidation behavior (see Appendix C), whereas mBMT exhibits a single maximum at 475 ºC (mBMT, Figure 4- 1). The characteristic carbon reflection in XRD (i.e. graphite [002] at $2\theta=26°$) is almost completely eliminated by ball milling of BMT (mBMT, Figure 4- 3i). There is a clear indication of attrition of the stainless steel milling materials to impart transition metals to mBMT, with corresponding to "iron/chromium", "iron/nickel" and "stainless steel" references found in the JADE software; subsequent discussion will refer to these reflections simply as SS (stainless steel) metals. The TPO and XRD results are reflective of the following events that occur during milling: carbon particles are reduced in size [31], the metal content is increased as milling components break down,

and the order and structure of the carbon is altered particularly when cyclohexene is present to lead to chemical reactions within the anthracite coal [15, 43].

Treating mBMT with HCl (mBMT-A, Figure 4- 2) decreases the major TPO peak from ~ 475 ºC to ~ 375 ºC, and a second peak at ~ 425 ºC is observed. The SS reflections in XRD are reduced significantly after acid treatment (mBMT-A, Figure 4- 3i), and residual ash content is reduced from 30.7 to 5.3% (Figure 4- 2, inset). The change in TPO cannot be attributed to metal removal, as this would be expected to shift the TPO to higher temperatures. A decrease in particle size would lead to a decrease in TPO temperature, but this is not expected to be significant with acid treatment and would not lead to a bimodal TPO profile. Thus, the bimodal TPO profile is suggestive of two regions of reactivity and the large TPO temperature shift (relative to mBMT) is on the order expected for a change in carbon reactivity. Acid treatment of mBMT has changed the carbon structure.

The NaOH treatment, somewhat surprisingly, gives rise to a third TPO peak at 600 ºC (mBMT-AB, Figure 4- 2). XRD of mBMT-AB provides a strong indication for the presence of calcite in the material, a surprising match as calcium was not intentionally added to mBMT at any stage of processing and was not found in NAA of the BMT coal precursor. The unexpected observation of calcite and its implications are discussed further in the subsequent section ***"Calcite"*** below. Ash content is *increased* after NaOH treatment, from 5.3% to 16.4%. However, the ash content of (mBMT-A) is likely to be artificially deflated due to iron and carbon interactions [1] and the ash content of mBMT-AB is likely inflated due to the presence of calcite. Due to these effects (see additional discussion in "***Ash content***" below), the term 'apparent' ash content is used in subsequent discussion. Due to complications with ash content, a qualitative analysis of the XRD data indicates that the relative intensity of iron carbide has decreased relative to the carbon reflections. The NaOH treatment has slightly reduced the amount of iron in the sample.

UV Raman of mBMT-AB (Figure 4- 4a) shows peaks characteristic of carbon-based samples: a G peak at 1600 cm^{-1}, a D peak at 1427 cm^{-1}, and a second order G peak at 3150 cm^{-1} [71]. The D peak shift to 1427 cm^{-1} is characteristic of UV excitation (compared to a peak at ~1350 cm^{-1} for visible excitation). It is this shift in the D peak for

UV Raman that lowers the 'sp^2 shielding effect' and helps to delineate the sp^2 D peak from the diamond peak. The peaks at 1086 cm^{-1}and 1748 cm^{-1} are characteristic of calcite [72]; the intensity of these calcite peaks varied depending upon sampling location. The origin for the vibration at ~ 2330 cm^{-1} is unknown.

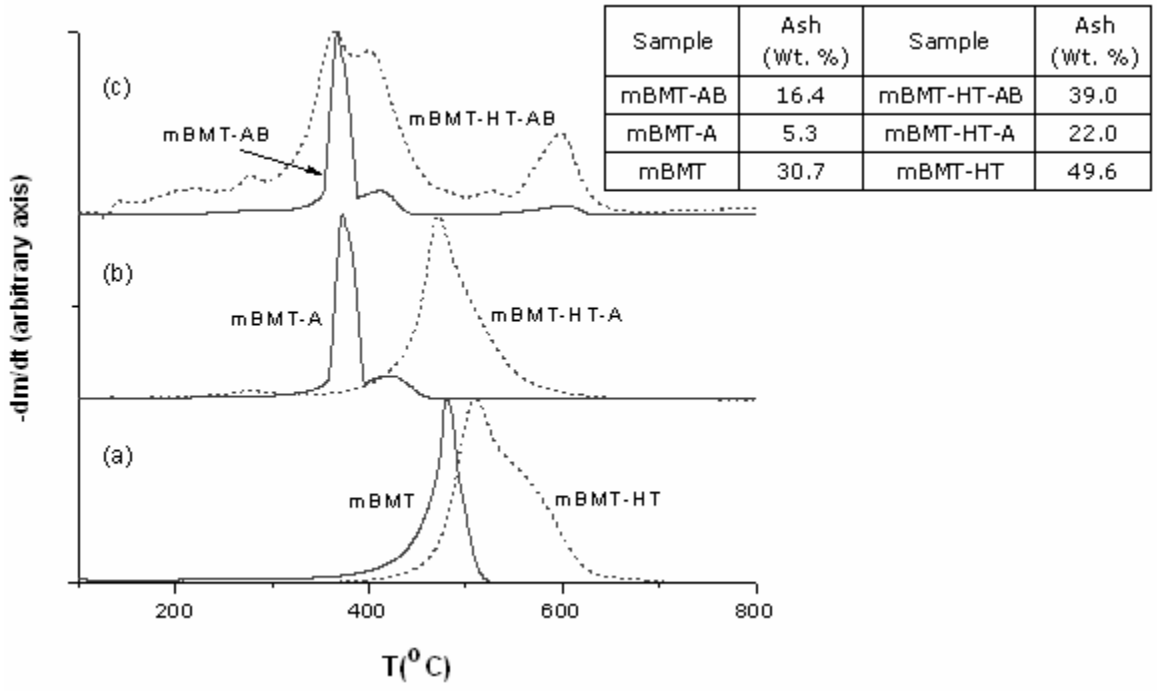

Sample	Ash (Wt. %)	Sample	Ash (Wt. %)
mBMT-AB	16.4	mBMT-HT-AB	39.0
mBMT-A	5.3	mBMT-HT-A	22.0
mBMT	30.7	mBMT-HT	49.6

Figure 4- 2: TPO and ash contents of the mBMT samples, with (dotted lines) and without (solid lines) the HT anneal. The synthesis sequence (as shown in Figure 4- 1) proceeds up the diagram. Residual ash content is shown in the inset.

The samples with a HT anneal oxidize at higher temperatures compared to the samples without thermal anneal (Figure 4- 2). The anneal shifts the TPO profile of mBMT from ~ 475 ºC to ~ 510 ºC and leads to the formation of an asymmetry in the oxidation profile. Volatiles are expected to be removed in the thermal anneal, and ash content is correspondingly increased from 30.7% to 49.6% (inset, Figure 4- 2). Thus the change in TPO of mBMT-HT relative to mBMT is reflective of removal of volatiles, increased carbon ordering, and the formation of iron carbides. XRD confirms the HT

anneal partially graphitizes the carbon. XRD of mBMT indicates the SS metal (Figure 4- 3i) has been converted to iron carbide in mBMT-HT (Figure 4- 3ii) by the HT anneal.

The asymmetry of mBMT-HT in TPO is significantly reduced for mBMT-HT-A, suggesting the acid treatment removes, reduces, or reacts the second region. The widening of the carbon peak in XRD suggests the carbon has lost long range order with the acid treatment, consistent with the decrease in the TPO profile. Apparent ash content is reduced from 49.6% to 22.0%; the presence of iron carbide complicates the interpretation of ash content, however (see ***Ash content section,*** on page 46). Qualitative XRD suggests the metal content is slightly increased after acid treatment, but this would be consistent with a loss of ordered carbon that would diffract. Iron carbide is expected to be soluble in acid [73], however, encapsulation in carbon would limit the solubility. The changes induced by acid treatment are much less pronounced for the mBMT-HT sample than for the mBMT sample.

Dramatic changes occur in the TPO for mBMT-HT-AB, with the multiple peaks in TPO indicating a quite complex and heterogeneous structure (Figure 4- 2c). The complex TPO profile cannot be attributed to calcite, as both mBMT-HT-AB and mBMT-AB had calcite. The low onset temperature of oxidation, ~140 ºC, is suggestive of the presence of amorphous carbon. The carbon peak in XRD has broadened (Figure 4- 3ii), consistent with a decrease in long range order. XRD and UV Raman once again indicate the presence of calcite after NaOH treatment.

Qualitative XRD analysis indicates the carbon: metal ratio for mBMT-HT-AB has not changed significantly relative to mBMT-HT-A. Ash content increases after NaOH treatment for the HT sample, but this can be explained by deflation of the ash of mBMT-HT-A and inflation of the ash of consistent of mBMT-HT-AB due to calcite. Both samples contain a large peak around 600 ºC, yet this peak is much more pronounced for mBMT-HT-AB. The drastic change in TPO data is consistent with the idea that NaOH treatment led to regions of greater and lesser order in the carbon; XRD is consistent with the former, but would not be sensitive to the latter.

UV Raman of mBMT-HT-AB (Figure 4- 4b) also shows the characteristic carbon peaks with a slight shift in the G peak to 1588 cm^{-1} and the second order G peak to 3148 cm^{-1}. This shift in the G peak is characteristic of a more graphitic sample, as peaks at or

above 1600 cm^{-1} are characteristic of chain-like sp^2 carbon rather than graphitic carbon [74]. The D peak is significantly decreased for mBMT-HT-AB relative to mBMT-AB, consistent with an increase in graphitic order. Notably, a vibration at 1331 cm^{-1} is observed, a frequency characteristic of crystalline diamond. Raman with UV excitation suffers less from the 'sp^2 shielding effect' than Raman with visible excitation due to the shift in the D peak and resonance effects. Even with UV excitation, the sp^2 shielding effect limits the detection limit of diamond in a sample that contains sp^2-hybridized carbon: Gogotsi et al. did not observe the diamond peak for samples with known NCD content until graphite impurities were removed by oxidation to lead to a ~25% diamond content in the material [75]. Thus presence of a vibration at 1331 cm^{-1} provides positive evidence for NCD in the material, but its absence does not provide evidence for the absence of NCD. The breadth of the D peak in certain samples may also mask peaks in this region.

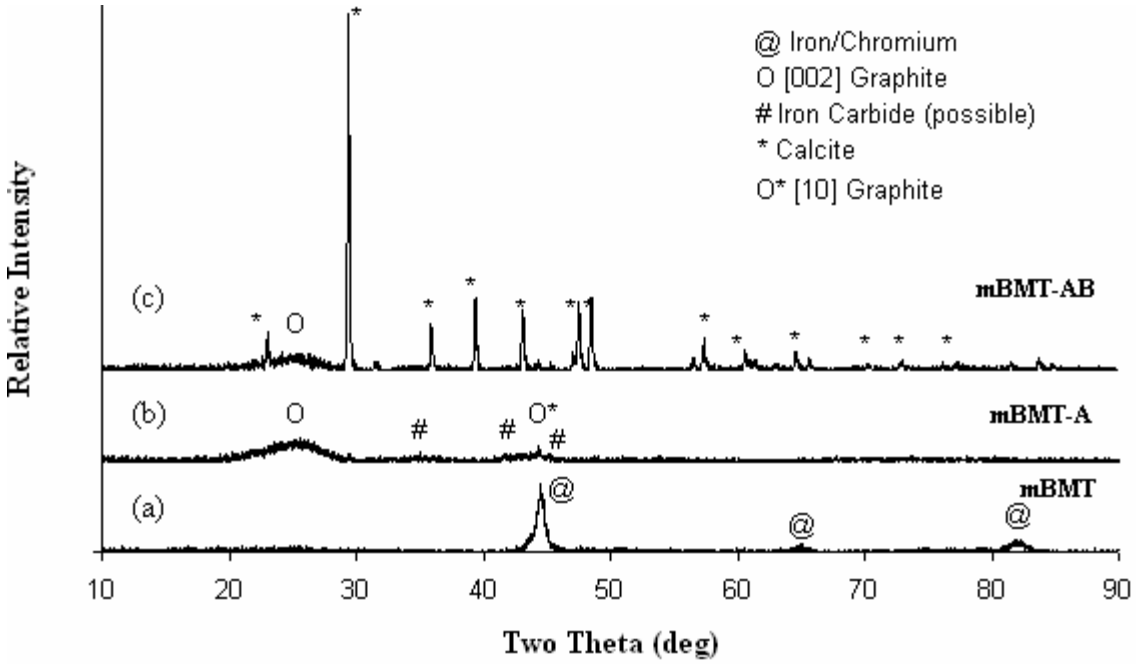

(i)

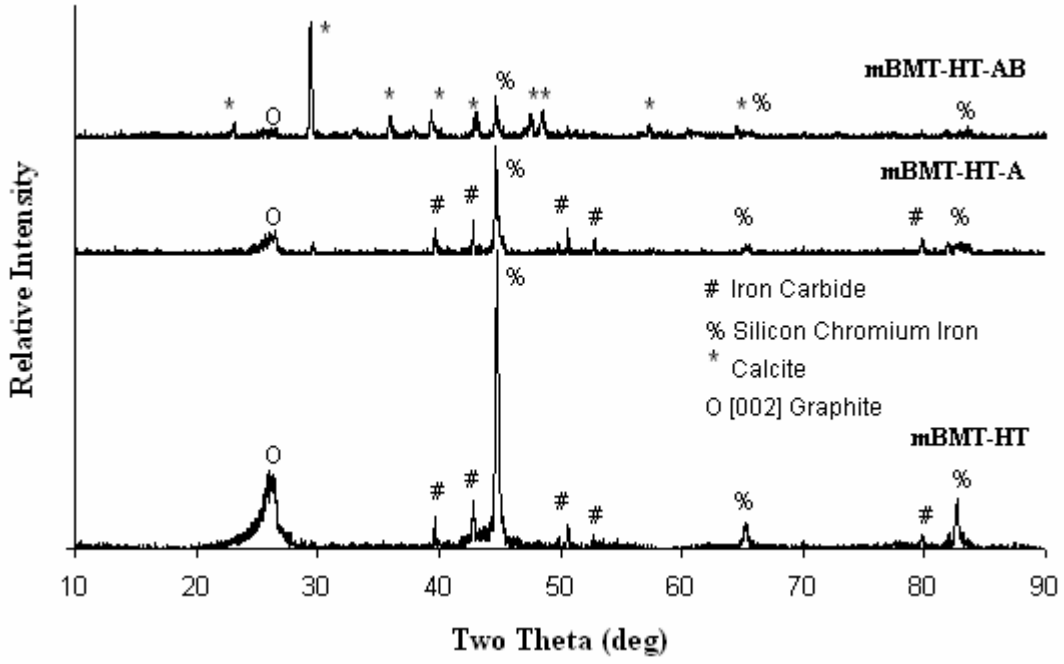

(ii)

Figure 4- 3: XRD of the mBMT series omitting (i) and including (ii) the HT thermal anneal.

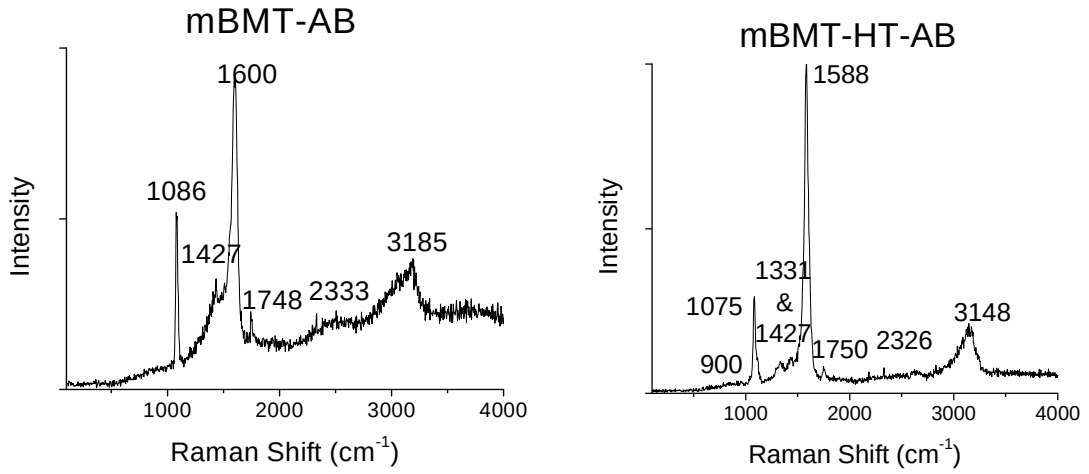

Figure 4- 4: UV Raman spectra (244 nm) of the AB samples from the mBMT sequence

Results of the mDBMT series

BMT was demineralized prior to milling in an attempt to elucidate the role of inherent mineral matter in the structural transformation induced by the ball milling process. Despite removal of the inherent mineral matter inherent of the anthracite, it was anticipated that SS would still be imparted to the sample upon milling. The discussion below attempts to highlight the features that differ for the mDBMT series compared to the mBMT discussion above. Direct comparison of the mDBMT and mBMT series is reserved for a later section.

TPO of mDBMT showed a maximum oxidation rate at 430 ºC (Figure 4- 5a). XRD confirms the introduction of SS metals during milling (Figure 4- 6).The introduced SS is significant, with apparent residual ash of mDBMT at 40.2% (Figure 4- 5, inset). In comparison DBMT oxidizes at ~ 535 ºC and has an ash content of 0.6% (see Appendix C). HCl treatment of mDBMT removes metals, judging from a significant reduction in residual ash (Figure 4- 5, inset) and the XRD profile which has significantly reduced SS reflections (Figure 4- 6). The major TPO peak shifts from 430 ºC to 390 ºC after acid treatment (Figure 4- 5b) and a shoulder at ~ 430 ºC is observed. This provides evidence that HCl alters the carbon structure, for reasons discussed above.

Subsequent NaOH treatment has only a minor effect on the TPO, and NaOH treatment once again leads to an increase in the residual ash content (Figure 4- 5, inset) and the introduction of calcite (XRD, Figure 4- 6). A slight peak at 600 ºC is observed in TPO for the mDBMT-AB sample. UV Raman of mDBMT-AB (Figure 4- 7) shows the characteristic carbon peaks (G peak at 1600 cm^{-1}, D peak at 1407 cm^{-1}, and 2G at 3180 cm^{-1}) and evidence for calcite (1086 cm^{-1}). The high frequency of the G peak is indicative of sp^2 chains rather than graphitic carbon [76]

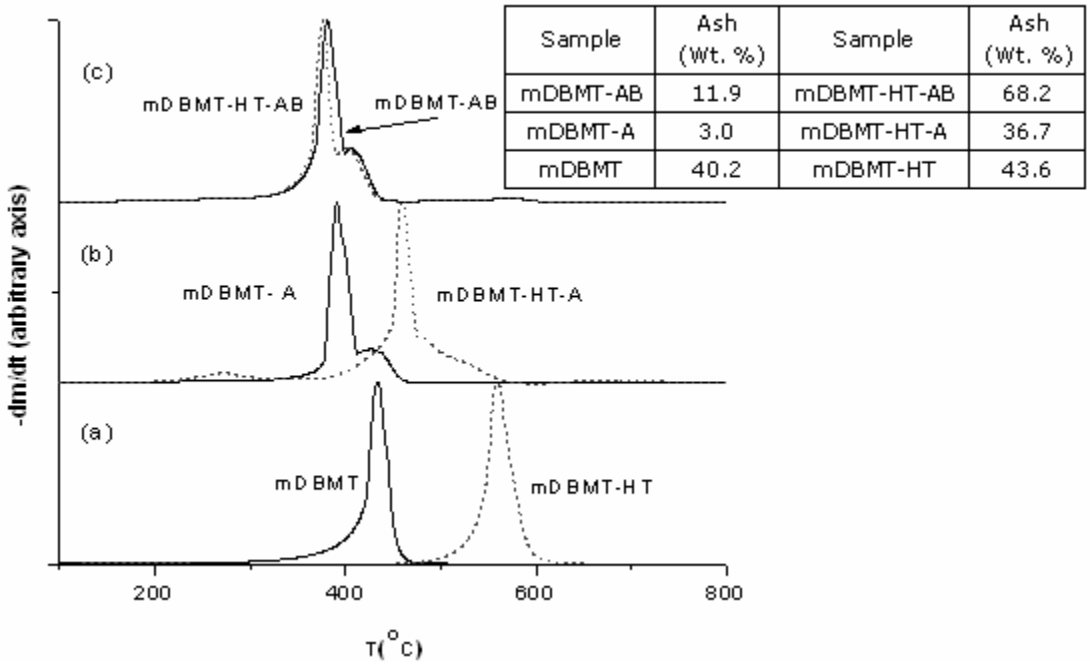

Sample	Ash (Wt. %)	Sample	Ash (Wt. %)
mDBMT-AB	11.9	mDBMT-HT-AB	68.2
mDBMT-A	3.0	mDBMT-HT-A	36.7
mDBMT	40.2	mDBMT-HT	43.6

Figure 4- 5: TPO and ash contents of the mDBMT samples, with (dotted lines) and without (solid lines) the HT anneal.

The HT anneal shifted the TPO profile to higher temperatures, from 430 ºC for mDBMT to 560 ºC for mDBMT-HT (Figure 4- 5). The shift to higher temperatures is consistent with increased order in the carbon samples. Increased carbon order is also apparent by the increased intensity and breadth of the graphite [002] peak in XRD (Figure 4- 6ii). Along with graphitization, XRD indicates the formation of iron carbide during the HT anneal.

Acid treatment of the HT sample again decreases the TPO to lower temperatures; the shift is more pronounced than was the case for mBMT-HT. Residual ash content is decreased and XRD indicates a slight decrease in relative intensity of the carbon reflections relative to the metal. NaOH treatment led to an additional decrease in TPO temperature to 375 ºC; a small shoulder at 400 ºC is observed and the ash content once again increases. Interestingly, the TPO of mDBMT-HT-AB lacks the complexity of mBMT-HT-AB and the other 'HT-AB' samples. This suggests the inherent mineral matter of BMT is related to the complex TPO profile, but this is not fully understood. XRD indicates calcite is formed from precipitation by the NaOH treatment: the calcite is found despite coal demineralization, suggesting the calcium is not a result of the inherent mineral matter. UV Raman of mDBMT-HT-AB (Figure 4- 7) shows peaks for carbon and calcite. As was the case for the BMT series, the G peak of mDBMT-HT-AB is shifted to lower frequencies relative to mDBMT-AB indicating a more graphitic structure. Unlike mBMT-HT-AB, there is no evidence for NCD found in the UV Raman of mDBMT-HT-AB. As stated above, UV Raman can provide evidence for the presence of NCD, but cannot confirm the absence.

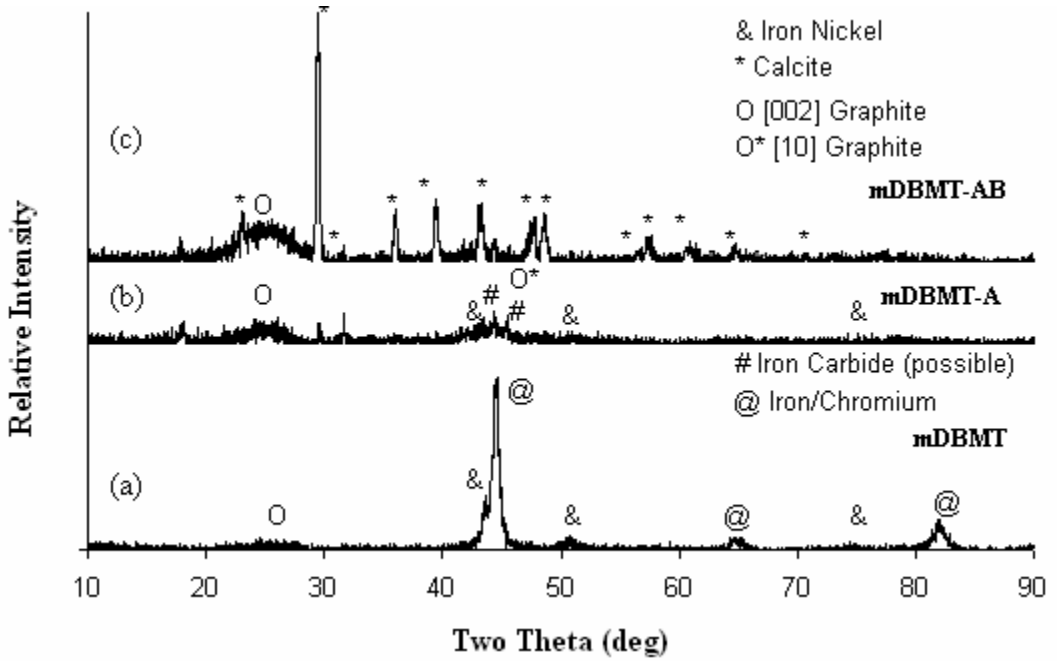

(i)

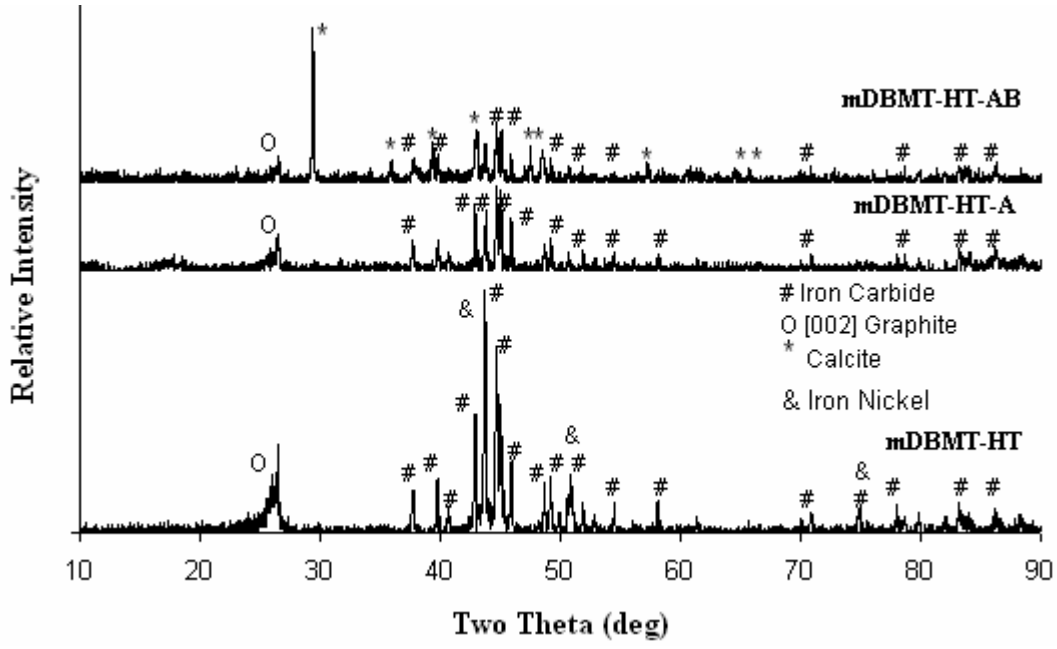

(ii)

Figure 4- 6: XRD of mDBMT series omitting (i) and including (ii) the HT anneal. Iron carbide peaks labeled have different stoichiometric values for iron and carbon (Fe_xC_y).

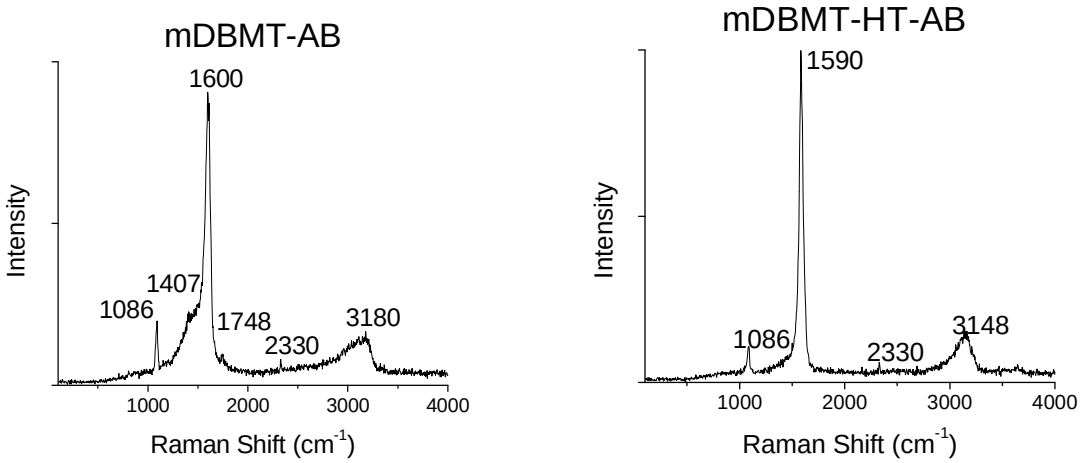

Figure 4- 7: UV Raman spectra (244 nm) of the AB samples from the mDBMT sequence

Results of the mDBMT-Fe series

Additional iron powder was added to demineralized BMT coal prior to the ball milling process (in the ratio of 1:9 Fe:DBMT) in an attempt to emphasize the effect of iron on characterization and subsequent processing steps. As before, the discussion is meant to emphasize the unique features of this series and comparison to other series is reserved to the end.

Iron addition shifted the main TPO peak slightly, from 430 ºC for mDBMT (Figure 4- 5) to 380 ºC (mDBMT-Fe, Figure 4- 8). A shoulder at 420 ºC is also observed. The mDBMT-Fe peak is broadened relative to mDBMT, highlighting the effect of Fe on TPO. XRD indicates the presence SS metals (mDBMT, Figure 4- 9i). The high residual ash (58.5%, Figure 4- 8, inset) relative to mDBMT (40.2%, Figure 4- 5, inset) can be explained by the added iron and a slight increase in mill attrition.

Acid treatment increases the TPO profile to 410 ºC and 440 ºC (mDBMT-Fe-A, Figure 4- 9). This is the only sample in which acid treatment led to an increase in oxidation temperature, and it is possible that the extra iron in mDBMT-Fe catalyzed carbon oxidation, shifting TPO to lower temperatures. However, there is also an indication from the carbon reflection in XRD that the acid-treatment led to an increase order in the carbon. The acid treatment has significantly decreased residual ash, from 58.5 % to 2.5 % (Figure 4- 8, inset) with a corresponding decrease in SS peaks in XRD

(Figure 4- 9). Treatment with NaOH decreased the TPO to 350 ºC with a prominent shoulder at 395 ºC (mDBMT-Fe-AB, Figure 4- 8). Residual ash content increased to 9.3 % and XRD indicates the presence of calcite (Figure 4- 9). The relative intensity of the carbon and metal reflections in XRD indicates the NaOH treatment has increased the relative fraction of ordered carbon in the material. UV Raman of mDBMT-Fe-AB (Figure 4- 10a) is similar to that of mBMT-AB and mDBMT-AB.

The HT thermal anneal led to increased order of the carbon samples, with a TPO oxidation at 555 ºC (mDBMT-Fe-HT, Figure 4- 8) and an increased order in carbon XRD (Figure 4- 9i). Residual ash content is 76.3 %, indicating artificial inflation as discussed above. XRD indicates graphitization and formation of iron carbide (Figure 4- 9ii). HCl treatment lowered oxidation temperature in TPO to 460 ºC and led to the resurgence of a shoulder at 510 ºC (mDBMT-Fe-HT-A, Figure 4- 8b). Residual ash content is reduced from 76.3 to 59.8%. XRD shows acid-treatment reduced the relative fraction of iron carbide (Figure 4- 9ii).

The complex TPO profile after NaOH treatment (mDBMT-Fe-HT-AB, Figure 4-8) is reminiscent of that observed for mBMT-HT-AB; the major TPO peak is at ~ 430 ºC. The low onset temperature of oxidation, ~250 °C, is suggestive of amorphous carbon, and XRD confirms mBMT-HT-AB has lost long-range order. The TPO profile exhibits a large peak at 600 ºC. This is the only sample for which NaOH treatment decreased rather than increased the residual ash content, and the carbon to metal ratio in XRD confirms this trend. XRD of mDBMT-Fe-HT-AB indicates the presence of calcite (Figure 4- 9). UV Raman of mDBMT-Fe-HT-AB (Figure 4- 10b) is similar to that of mDBMT-HT-AB; no peaks corresponding to NCD are observed.

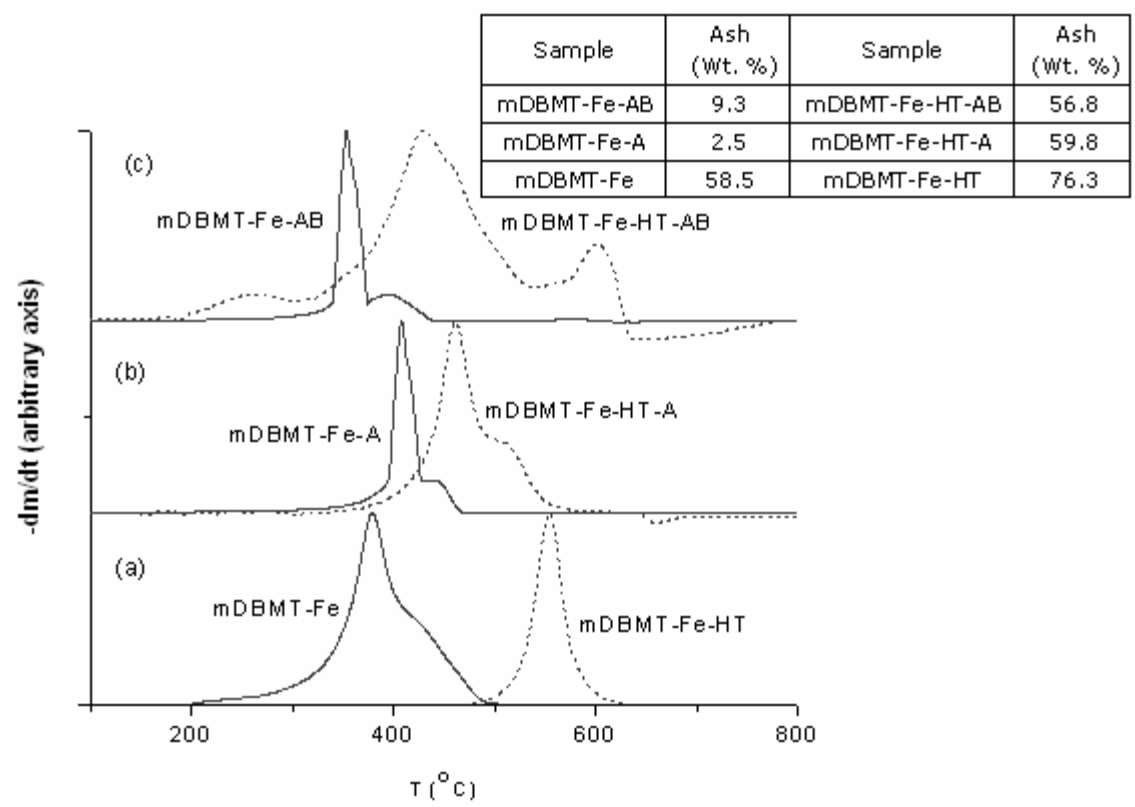

Sample	Ash (Wt. %)	Sample	Ash (Wt. %)
mDBMT-Fe-AB	9.3	mDBMT-Fe-HT-AB	56.8
mDBMT-Fe-A	2.5	mDBMT-Fe-HT-A	59.8
mDBMT-Fe	58.5	mDBMT-Fe-HT	76.3

Figure 4- 8: TPO and ash contents of the mDBMT-Fe samples, omitting (solid lines) and including (dotted lines) the HT anneal.

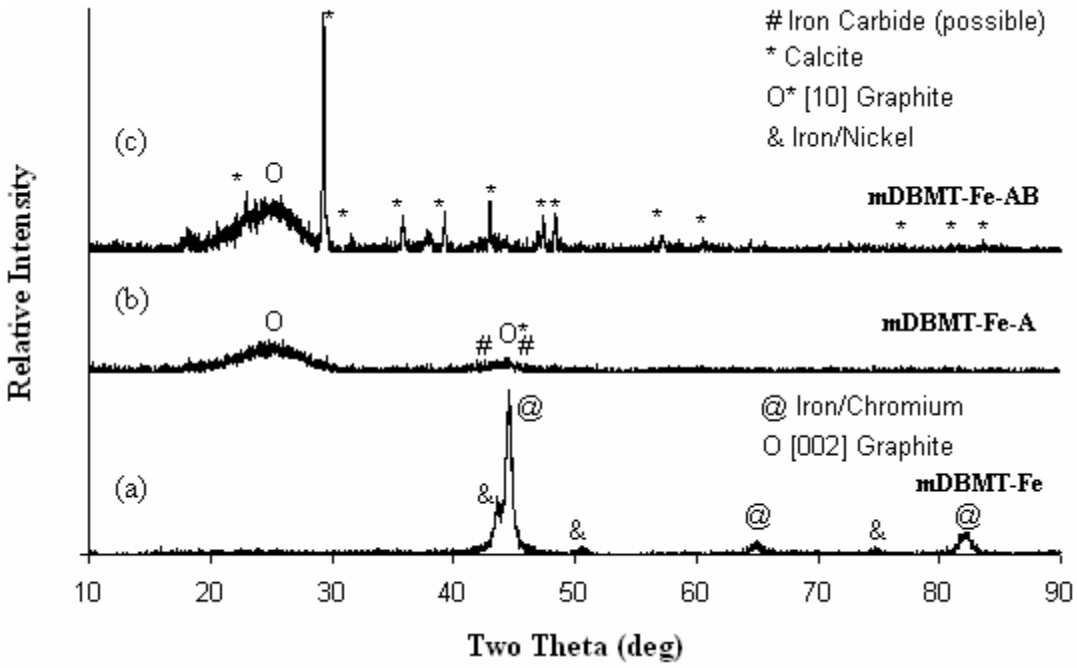

(i)

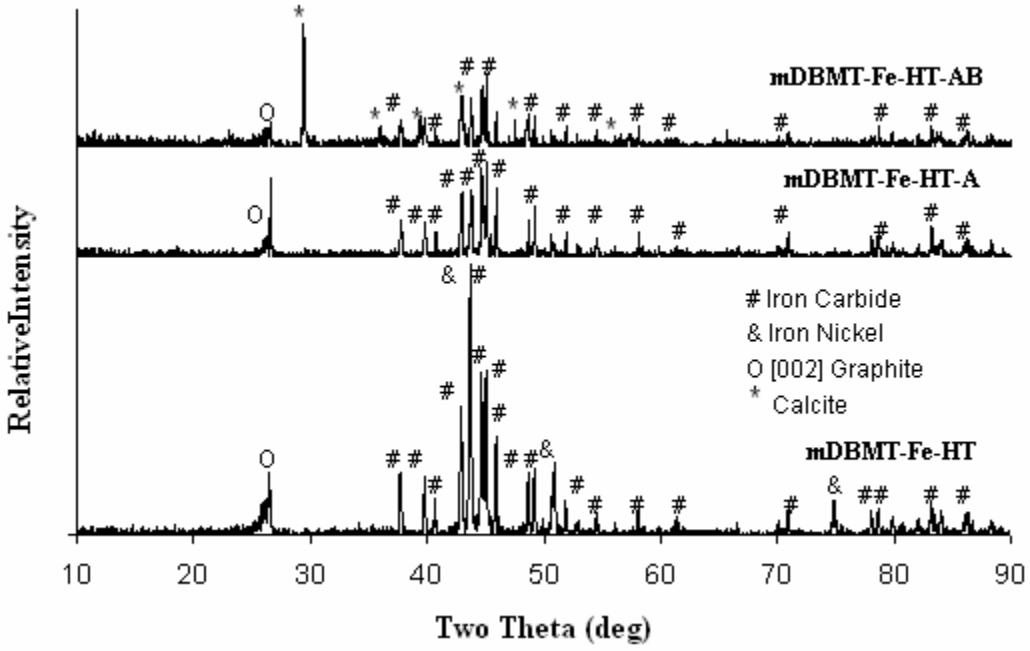

(ii)

Figure 4- 9: XRD of the mDBMT-Fe series omitting (i) and including (ii) the HT anneal.

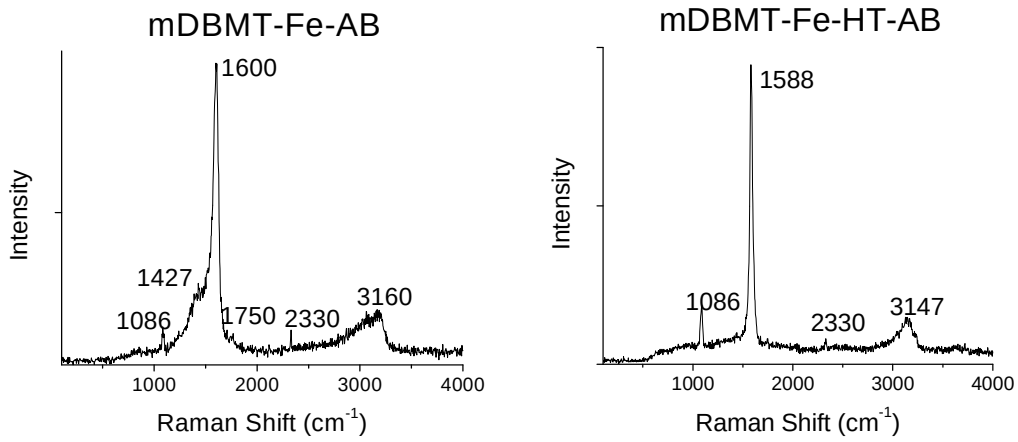

Figure 4- 10: UV Raman spectra (244 nm) of the AB samples from the mDBMT-Fe sequence

Results of the mDBMT-SS series

In the final sequence, SS powder was added to DBMT in an attempt to emphasize the effect of adding other transition metals to the ball milling process. TPO of mDBMT-SS shows a maximum oxidation rate at ~ 485 ºC; residual ash content is 57.0%, on the order of that observed for mDBMT-Fe (Figure 4- 11). XRD of mDBMT-SS shows the SS metal reflections (Figure 4- 12i), as expected, and closely resembles the XRD of the other samples directly after milling.

HCl treatment lowers the oxidation temperature to 375 ºC and leads to a shoulder at 420 ºC (mDBMT-SS-AB, Figure 4- 11). Residual ash is significantly reduced, to 4.6%, and SS peaks in XRD are also significantly reduced (Figure 4- 12i).

NaOH treatment does not significantly alter the TPO profile with peaks at 380 ºC and ~ 415 ºC (mDBMT-SS-AB, Figure 4- 11); residual ash content is increased to 15.5 %. XRD of mDBMT-SS-AB indicates the precipitation of calcite (Figure 4- 12i). UV Raman of mDBMT-SS-AB is similar to other 'AB' samples without the HT anneal, with one exception in that a small peak in the range of 620-860 cm^{-1} is observed (Figure 4-13), the origin of this peak is unknown.

HT anneal shifts the TPO to a higher temperature of 545 ºC, and leads to a shoulder at 580 ºC (mDBMT-SS-HT, Figure 4- 11). XRD confirms a more ordered carbon fraction and the formation of iron carbides (Figure 4- 12ii).

HCl treatment leads to a substantial decrease in oxidation temperature to ~ 420 ºC (mDBMT-SS-HT-A, Figure 4- 11); a shoulder at ~ 505 ºC is observed. However, XRD indicates the acid-treatment leads to more long range order in the carbon fraction (Figure 4- 12ii). Residual ash content remains significant (51.1%), however, the qualitative XRD carbon to metal ratio indicates a significant removal of the carbides by the acid treatment.

NaOH treatment of the HT sample once again leads to a complex TPO profile (mDBMT-SS-HT-AB, Figure 4- 11), exhibiting low temperature (265 ºC) oxidation characteristic of amorphous carbon, a broad peak at 425 ºC and a quite pronounced high temperature peak ~ 600 ºC . XRD indicates the carbon has lost long range order. NaOH treatment once again increases ash content and XRD shows the presence of calcite (Figure 4- 12ii). UV Raman of mDBMT-SS-HT-AB (Figure 4- 13Figure 4- 13a) confirms the presence of calcite, with peaks at 1086 cm^{-1} and 1748 cm^{-1} [72]. The intensity of the calcite vibration varied widely based on sampling location.

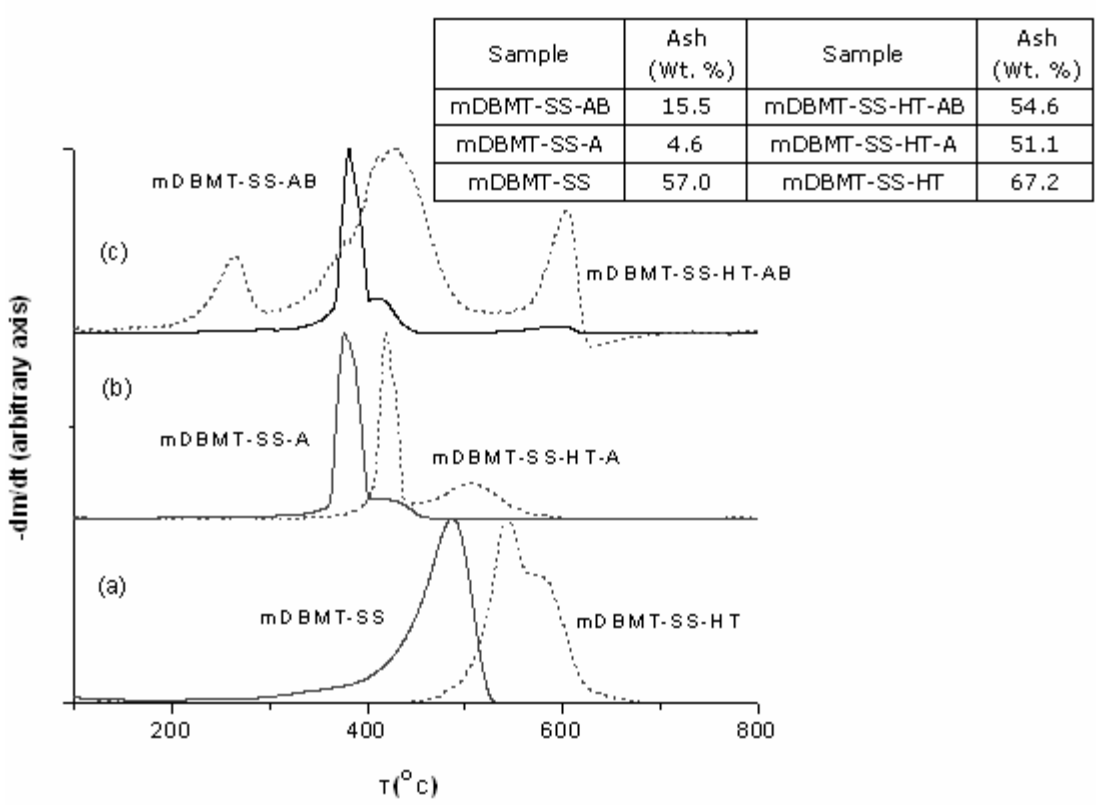

Figure 4- 11: TPO and ash contents of the mDBMT-S samples, with (dotted lines) and without (solid lines) the HT anneal.

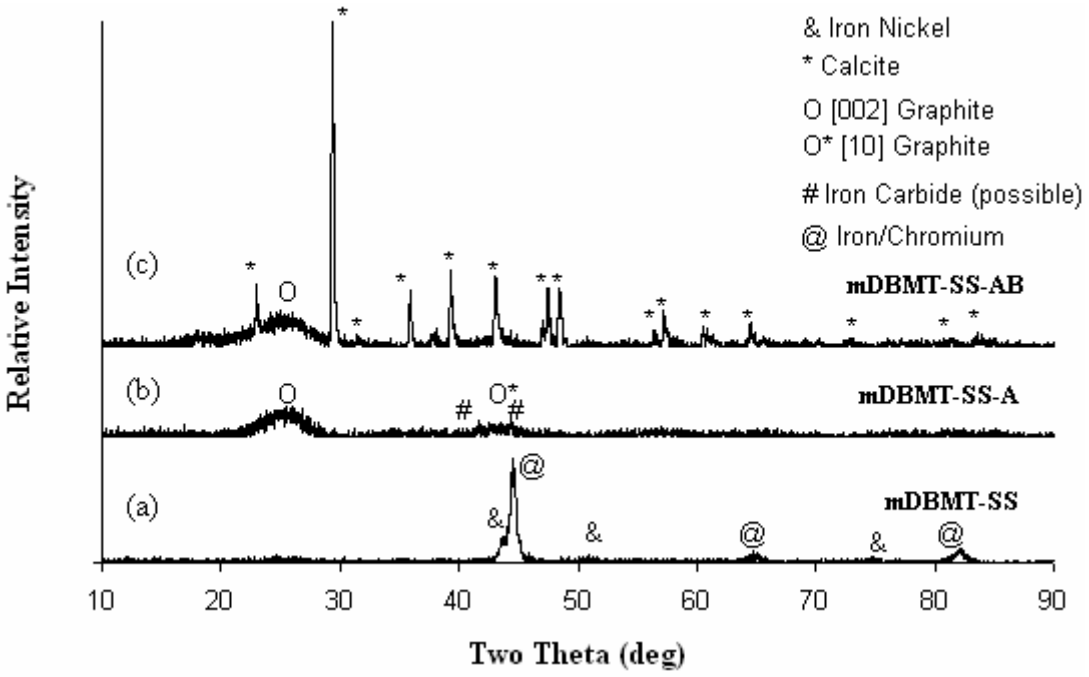

(i)

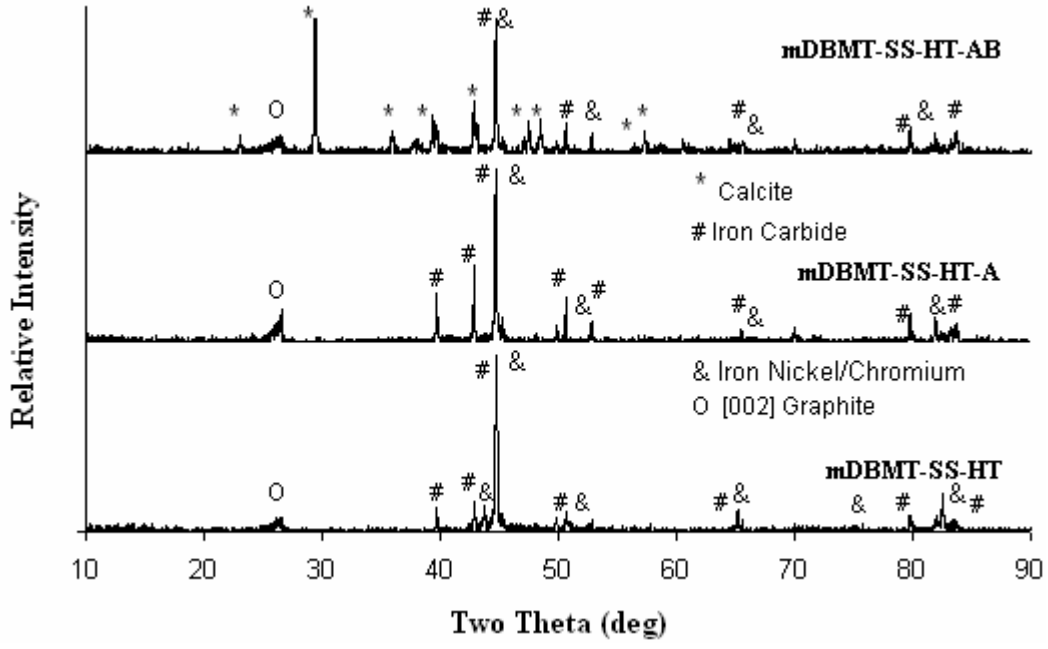

(ii)

Figure 4- 12: XRD of the mDBMT-SS series omitting (i) and including (ii) the HT anneal.

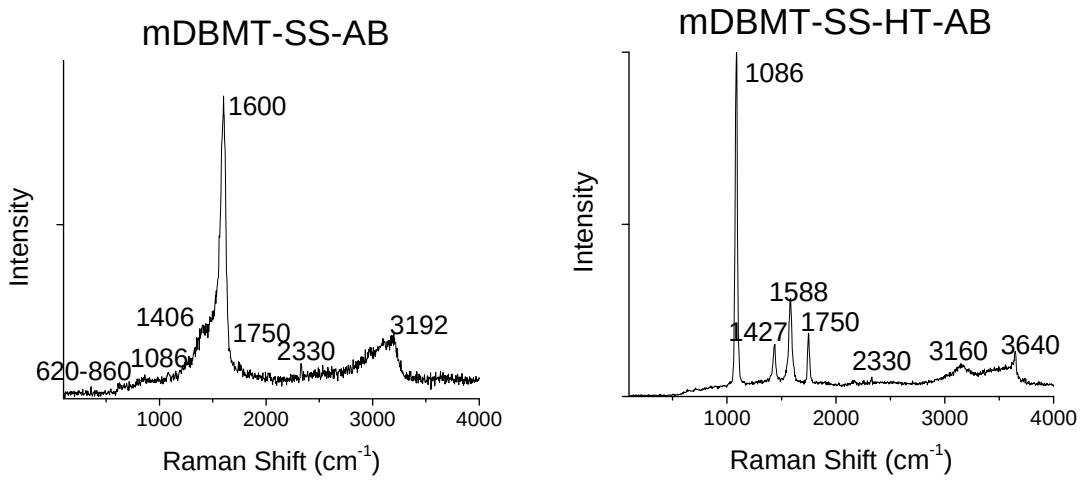

Figure 4- 13: UV Raman spectra (244 nm) of the AB samples from the mDBMT-SS sequence

Discussion—Limitations in the analysis

Prior to discussing the results, we first discuss complicating factors that limit subsequent analysis.

Calcite. Evidence for calcite is found in XRD of every material treated with 10 M NaOH in this chapter, including the DBMT series where mineral matter inherent to the coal was removed prior to processing. Calcite is also evident as minor reflections in many of the acid-treated samples. The source of calcite is unclear, although the deionized (DI) water source used in these experiments showed a 30 ppm concentration of Ca^{2+} (see Appendix D); DI water would typically contain less than 0.02 ppm Ca^{2+} [77]. It is not clear, however, whether the high Ca^{2+} concentration in the DI water is the source of calcium that precipitates upon contacting NaOH with solid carbon, or a symptom of a solid calcite contamination elsewhere in the laboratory. The presence of calcite limits the possible interpretation of step 2 in the above proposed reaction sequence as it is anticipated that either aqueous Ca^{2+} or solid $CaCO_3$ would affect this reaction . The formation of calcite will also influence the residual ash content in the 'AB' samples. It is not clear how the high calcite may affect the TPO of the 'AB' samples, however, the TPO of the samples

with HT anneal differs greatly from those without HT anneal, and both samples contained calcite.

Apparent ash content. The unexpected increase in ash content was previously observed by Lueking et al. [1] and explained by the conversion of iron carbides to iron oxides upon oxidation. In brief, oxidation of iron carbides in TPO leads to the formation of Fe_3O_4, which is heavier than either FeC or Fe_3C. TPO of FeC, for example, shows a mass *increase* of 31.8 % (Appendix E). This effect is expected to be amplified in materials with high iron carbide content, namely the 'HT' series. Conversely, the presence of calcite is expected to artificially inflate the ash content in AB samples. Thus, the ash content may be artificially deflated in the 'HT and 'HT-A' samples and artificially inflated in the 'AB' and 'HT-AB' samples.

Limitations in the Characterization Methods. In TPO, the temperature at which a carbon oxidizes is influenced by the structure of the carbon material, the overall particle size, and the presence of metals. The carbon order influences oxidation temperature: graphite will oxidize at temperatures of ~850 °C or above, while amorphous carbon materials will generally oxidize at temperatures less than ~250 °C. However, carbon nanomaterials will oxidize at moderate temperatures (~500 °C) although they may be considered ordered, as they are composed of graphene sheets in a regular manner. TPO must be interpreted with caution, and may provide contradictory information relative to XRD in terms of the ordering of the material. Here, changes in particle size with milling, accompanied by metal addition, removal, and carbide formation complicate the use of TPO as an indicator of carbon order and structure.

One might be tempted to assign various peaks and/or shoulders observed in the TPO to certain features of the material (i.e. presence of iron carbide), but we can find no real trends when comparing TPO behavior to added metal content. We therefore have attempted to limit our discussion of the TPO results to shifts in temperature, using TPO as a relative measure. In several cases, the TPO behavior is inconsistent with metal removal (i.e. for mBMT series, discussed above), thus changes in carbon order can be stated with some confidence. The most notable features are the materials that oxidize at

low temperature and the formation of a third region in TPO at ~600 °C. These two features are discussed in more detail below.

As stated above, an objective of this work was to explore processing steps that led to NCD formation. The characteristic XRD pattern for diamond has reflections at 2θ = 43.89°and 75.4° in a ratio of 4:1, which correspond to (111) and (220). Unfortunately, the major diamond peak at 43.89° is not likely to be distinguishable from iron, stainless steel, and/or iron carbide all of which have peaks in this range. Other methods to detect NCD (e.g. UV Raman, TEM) are limited by the overall content of the material and can provide positive evidence for its presence, but cannot provide conclusive evidence for its absence. Iron species that likely catalyze NCD formation are not easily removed, as shown here by both XRD and residual ash content. The presence of iron renders XRD ineffective in identifying NCD and complicates other potential characterization methods (e.g. NMR).

Discussion: Delineating the Role of Metal

We can state with confidence that the milling process adds metal to the carbon, and the imparted metal reacts with carbon to form carbides during the HT anneal. The metal in the as-milled material is easily removed by acid treatment, whereas the metals present after HT anneal are difficult to remove by acid treatment.

The experiments were designed to emphasize the role of metals in the processing stages. No attempt was made to completely eliminate SS addition due primarily to limitations with available equipment. Substitution of SS milling components for ceramic components was both cost prohibitive and was expected to significantly alter the physics of milling, introducing yet another experimental variable. Few consistent trends emerge regarding the effect of metal 'emphasis'. The transformations of the metal within XRD are fairly consistent in the four series studied, with the one exception of the reflections in the range of 40-50° for the samples after thermal anneal. The regions in question are plotted together in Figure F- 6 (Appendix F). In this region, the XRD of mBMT-HT closely resembles that of mDBMT-SS-HT, with a strong reflection at 44.7° and a weaker reflections at 42.78°; mDBMT-SS-HT has an additional reflection at 43.74°. The XRD of mDBMT-HT and mDBMT-Fe-HT have these reflections and additional reflections at

45.0, 45.9, 48.6, and 49.2°. A peak search/match in Jade suggests the first set better matches iron carbide with the stoichiometry of FeC, whereas the second set better matches cohentie (Fe_3C). The origin of these complexities is not clear, and the "grouping" of samples based on metal content is also not clear. The most likely explanation is slight variations in the structure of the carbides due to subtle variations in processing or preparation.

Adding metals does seem to broaden the TPO peaks: the TPO profile of mDBMT was the sharpest of any of the samples directly after milling, followed by mBMT. The samples with metal addition oxidize at higher temperatures, the opposite from what would be expected from a catalytic role of metals in carbon oxidation. This may suggest that added metals may lead to more complete amorphitization within the milling process, but this is speculative at best.

Discussion: Evidence for Changes in Carbon Structure

As stated above, there is evidence that the acid treatment alters the carbon structure, particularly for samples directly after milling. Comparing the TPO of mBMT to mBMT-A shows the most pronounced shift in oxidative temperature induced by acid treatment. The large shift in mBMT relative to the other 'as-milled' samples is likely related to the demineralization procedure used for the other materials, all of which utilized DBMT. As discussed above, the shift for mBMT-A to lower temperatures is despite metal reduction, which would be expected to shift TPO to higher temperatures. Furthermore, the mBMT-A TPO profile has become bimodal indicating two regions of oxidative reactivity. Together, this is a fairly conclusive argument that acid-treatment has altered the carbon structure. The TPO profile of all the acid-treated samples for which the thermal anneal has been omitted are quite similar, suggesting that there are no *major* effects of mineral matter and the added Fe or SS has little effect on carbon structure (beyond that already added due to attrition of SS milling materials) on carbon structure. The high frequency G peak observed in UV Raman of the 'AB' samples suggests the samples tended to be more 'polymeric' than 'graphitic' when the thermal anneal was omitted.

HT graphitizes the carbon, as expected, and leads to three-dimensional carbon order, evidenced by the XRD. The carbon XRD reflection also suggests the acid treatment tends to decrease long-range order for BMT-HT and DBMT-HT while increasing long-range order for samples with added Fe and SS.

XRD consistently shows NaOH reduces the FeC content of the material as well as decreases the long range order of the carbon. The TPO profiles suggest dramatic changes in the "HT" samples after NaOH treatment (with the exception of the mDBMT-HT-AB). TPO shows carbon oxidizes both at a decreased temperature (T<250 °C) and at an increased temperature (T>600 °C), suggesting regions or both lesser and greater order are created by the NaOH treatment. Although one might envision NaOH would oxidize solid carbon to create a more reactive material, it is difficult to see how NaOH would react with solid carbon to create a more structurally ordered carbon material. The observation of the increased oxidation temperature after NaOH treatment, combined with the reduction in FeC after NaOH treatment, provides evidence for step 2 in the proposed reaction sequence. This peak at 600 °C was also observed for all 'AB' samples in which the HT anneal was omitted, and may be an indication of reaction of a small amount of iron carbide that may be in these samples.

Certain aspects of the study provide corroborating evidence (or lack thereof) for the reaction sequence previously put forth by Lueking et al. and stated in the introduction of this chapter. In brief, Lueking et al. stated that reactive ball mill in cyclohexene increased the reactivity of the anthracite coal precursor, forming an amorphous carbon that included both sp^2 and sp^3 hybridized content. Evidence for sp^3 hybridized carbon is shown in 'AB' samples, although UV Raman of as-milled samples was not collected. Low frequency UV Raman vibrations in mBMT-AB, mDBMT-Fe-AB, and mDBMT-SS-AB may be indicative of sp^3 carbon peak; the sp^3 'T' peak is shifted to lower frequency as the material becomes increasingly hydrogenated [78]. The frequency of the G peak in UV Raman indicates the final product of the materials without HT anneal were 'polymeric' with sp^2 chains, whereas the samples that included HT anneal were more 'graphitic' in nature. The TPO of the milled samples is generally lower than that of the precursor and analysis of the carbon peak shows milling decreases long range order. Certainly, reactive ball milling in cyclohexene is both a chemical as well as physical

process, as the changes in carbon structure would not be expected for physically treated anthracite coal.

In prior work, NCD and the other crystalline region were observed only after the 10 M NaOH treatment. Here, strong evidence for the presence of NCD is provided by UV Raman in one sample (BMT) only after the NaOH treatment. However, as stated above, UV Raman can provide only positive evidence for NCD and cannot provide evidence for its absence in other samples. The drastic changes in TPO after NaOH treatment certainly suggest unusual and unexpected effects of NaOH treatment, although the role of calcite formation in this processing step is unclear and complicates data interpretation. The reaction between NaOH and the milled materials needs further exploration in a more controlled manner.

Summary and Conclusions

The objective of this work was to explore the role of metals in the reaction scheme proposed by Lueking et al. provided in the introduction. The role of metals was explored by using BMT coal 'as received', demineralizing the coal prior to milling, and adding Fe, and separately SS, to 'emphasize' the role of metal addition. In all cases, metal was introduced during ball milling, and no consistent trends were found by further metal 'emphasis'. When the materials were subjected to a HT anneal, the introduced metal reacted with carbon to form carbides and other regions of the carbon graphitized. The metal carbides were inaccessible to HCl, validating step 1 in the proposed reaction sequence. There was consistent evidence that NaOH treatment reduced the amount of iron carbide in the materials, although this was complicated by the unexpected formation of calcite. There is evidence that both HCl and NaOH alter the carbon structure, validating step 3 in the proposed reaction sequence. The effects of HCl and NaOH treatment are more pronounced for materials in which the HT thermal anneal is omitted. The NaOH treatment led to carbon that was both more amorphous and more ordered in nature. Strong evidence for NCD was found in one of the four materials studied

Chapter 5

Results and Discussion II: Structural Transformations and Hydrogen Evolution

Chapter Overview

The purpose of this research was to investigate and understand the structural evolution of carbon, hydrogen evolution characteristics, and the relation between the two parameters in ball milled coal samples. An alternate coal precursor was used for comparison to the Buck Mountain anthracite used by Lueking et al. [1]. As stated in Chapter 1, the hypotheses were:

d) The degree of order (and its susceptibility to change) in the precursor carbon structure affects hydrogen storage and trapping.
e) Ball Milling leads to changes in the carbon structure.
f) Ball milling with cyclohexene facilitates the structural changes due to the reaction of cyclohexene with the coal.

An initial screening process of five anthracite coals was conducted (see Appendix A) using TPO and XRD to determine the inherent structural order, and the susceptibility of the various coals to change when subjected to a moderate (i.e. 1673 K for 3 hours) thermal anneal. Demineralized Summit (DS) anthracite and its annealed analog (DS-HT) were selected for further testing of the above hypothesis, with graphite (G) as a control. Summit is unprocessed anthracite recovered from the Tracey vein. It has a relatively high volatile matter content (11.1wt%, dry), low fixed carbon content (71.2 wt%, dry [63]). The ash content of Summit is 17.6%; demineralization reduces the ash content to 1.2 wt% (see Appendix A).

The discussion in this chapter is organized around experiments designed to probe the hypothesis stated above.

Common Methods

Further details of the characterization methods are found in Chapter 3. In brief, common to all tests are the following characterization methods: (1) TPO probed

oxidative reactivity, (2) XRD probed the structural order of the carbon, (3) ultra-violet Raman (UVR) probed carbon order and associations, (4) solvent swelling provided a qualitative indication of the cross-link density [79-82], (5) helium density measurements probed structure, in particular networking and accessibility to helium, and (6) nitrogen gas adsorption probed surface area and porosity. Solvent swelling measurements were used to give an indication of the cross-linked structure of the samples.

Thermogravimetric-mass spectrometry (TGMS) evaluated the hydrogen evolution from samples in which the carbon precursor was varied (Section A), as this series of experiments provided the most conclusive information regarding trends in structural evolution during ball milling. The MS signals are monitored as each sample is heated to 1000 ^{o}C in Argon. The MS signals are assigned as follows: (1) hydrogen (m/z = 2), benzene (m/z = 78), cyclohexene (m/z = 82). Additional signals were monitored and are provided in Appendix G. It should be noted that the three signals above are unique: cyclohexene does not have an MS line at m/z = 78, and neither benzene nor cyclohexene have MS lines at m/z = 2.

Sample Notation

Here, 'S' refers to Summit Anthracite and 'DS' refers to demineralized Summit. The demineralization procedure is described in Chapter 3. DS-HT refers to demineralized summit subjected to 1673K for 3 hours to increase carbon order. The standard ball milling conditions were 80 hours using 6 g of coal with 20 ml of cyclohexene solvent. The number in a sample name refers to the milling time, whereas 'CH' refers to the cyclohexene milling solvent. Omission of 'CH' refers to milling without solvent. An added '<' or '>' is used in sample nomenclature to denote decreasing and increasing solvent amount by a factor of 2, respectively. Further details in the variations of the standard milling conditions for each test are given within the relevant section below.

Results and Discussion

A: Effect of Precursor Order on Structural Transformations and Hydrogen Evolution.

1. Variation of Precursor Order

In this series of experiments, the relative order of the carbon precursor was varied by using DS, DS-HT, and graphite (G). All three were milled at standard conditions to yield DS-80CH, DS-HT-80CH and G-80CH.

TPO and XRD Verify Anticipated Precursor Order. TPO of the carbon precursor indicates carbon order is as follows: G>DS-HT>DS with the maximum rate of oxidation occurring at 795, 700, and 460 ºC, respectively (Figure 5- 1). The crystallite height, Lc, in XRD provides the following indication of three-dimensional order of the materials: G >> DS-HT ~ DS with Lc values of 718, 14, and 15 Å, respectively (Figure 5- 2). The crystallite diameter, La, for G, DS-HT, and DS are 1034, 44, and 14 Å, respectively (Figure 5- 2). The XRD results indicate the 'HT' thermal anneal of DS led to an increase in the in-plane dimension of crystallites with very little affect on three-dimensional stacking order.

Probes of 3-D Networking within Amorphous/Turbostratic Regions. Solvent swelling ratios and helium densities give additional information regarding the 3-dimensional nature of the structure, including amorphous regions that would not be probed by XRD. In polymer science, the swelling ratio is proportional to the number of crosslinks, related through the Flory-Rehner relationship [83, 84]. Clearly, the relation is more complex for heterogeneous coal-structures, and complex methods using multiple solvents with varying hydrogen donation have been developed [80, 85]. Here, our intent is to perform a simple qualitative comparison of the solvent swelling ratio, and hence the relative number of cross-links, by using a single solvent. Our intent is not to probe the chemical nature of the cross-links, information that requires the use of multiple solvents of varying chemical nature.

For both solvent swelling and helium density measurements, graphite serves as a baseline for comparison. The helium density of G is 2.2 g/cc, in agreement with generally accepted values for graphite [86]. The swelling ratio of G is 100%, as expected, an indication that the solvent does not disrupt the three-dimensional, highly ordered structure of graphite that is held together by weak van der Waals interactions between the adjacent graphene layers. DS-HT has a swelling ratio of 113, whereas DS has a swelling ratio of 124. The swelling of DS is interesting given that DS is an anthracite, and not expected to swell significantly. Thus the swelling ratio also indicates the relative order of the materials is G >DS-HT > DS, consistent with the other characterization methods. DS and DS-HT have a lower helium density compared to G, reflective of regions of the structure that are inaccessible or 'closed off' to helium. The difference in the helium density of DS and DS-HT is likely within experimental error.

UV Raman as a probe of local carbon structure. Changes in the carbon precursor seen in XRD and TPO are also reflected in the location of the G peak in UVR (Figure 5-4): The G peak of G (graphite), DS-HT, and DS are at 1582, 1588, and 1602 cm^{-1}, respectively. An increase in the G peak frequency in UVR above 1580 cm^{-1} for graphite is characteristic of sp^2-chain like structures; G-type vibrations above ~1600 cm^{-1} have been associated with chain-like, polymeric sp^2 carbon [74]. The shift in the UVR G peak, a reflection of sp^2 clustering, is thus consistent with the La crystallite size measured in XRD. The commonly used ratio of the D to G peak intensity also follows the expected range of carbon order, with an I(D)/I(G) of 0, 0.1, and 0.3 for G, DS-HT, and DS, respectively.

2. Structural Transformations Induced by Ball Milling

Changes in Carbon Order With Ball Milling (TPO and XRD). Ball milling in cyclohexene consistently increased the oxidative reactivity of the samples, as evidenced by a shift in the TPO to lower temperatures (Figure 5- 1). Upon ball milling, the main TPO peak for DS shifts from 460 ºC to 405 ºC; DS-HT shifts from 700 ºC to 485 ºC; and G shifts from 795 ºC to 475 ºC. DS-HT and G both exhibit low temperature oxidation

after milling suggestive of very disordered (in fact amorphous) carbon, behavior not seen for DS-80-CH. These low temperature TPO peaks do not follow trends of ash content, thus cannot be attributed to increased catalytic activity that would lower carbon oxidation temperatures. G-80-CH also has a high temperature shoulder at ~ 540 ºC that is more pronounced than in the other materials. In contrast, the TPO profile for DS-80-CH is quite sharp suggesting carbon of uniform reactivity; in fact, the breadth of the peak has decreased compared to DS. The TPO results imply that increased order in the carbon precursor leads to a more heterogeneous structure upon reactive ball milling in cyclohexene. Further, the relative shift in the TPO profiles suggests that the structural changes induced by reactive ball milling are more significant for precursors that contain a higher order prior to milling.

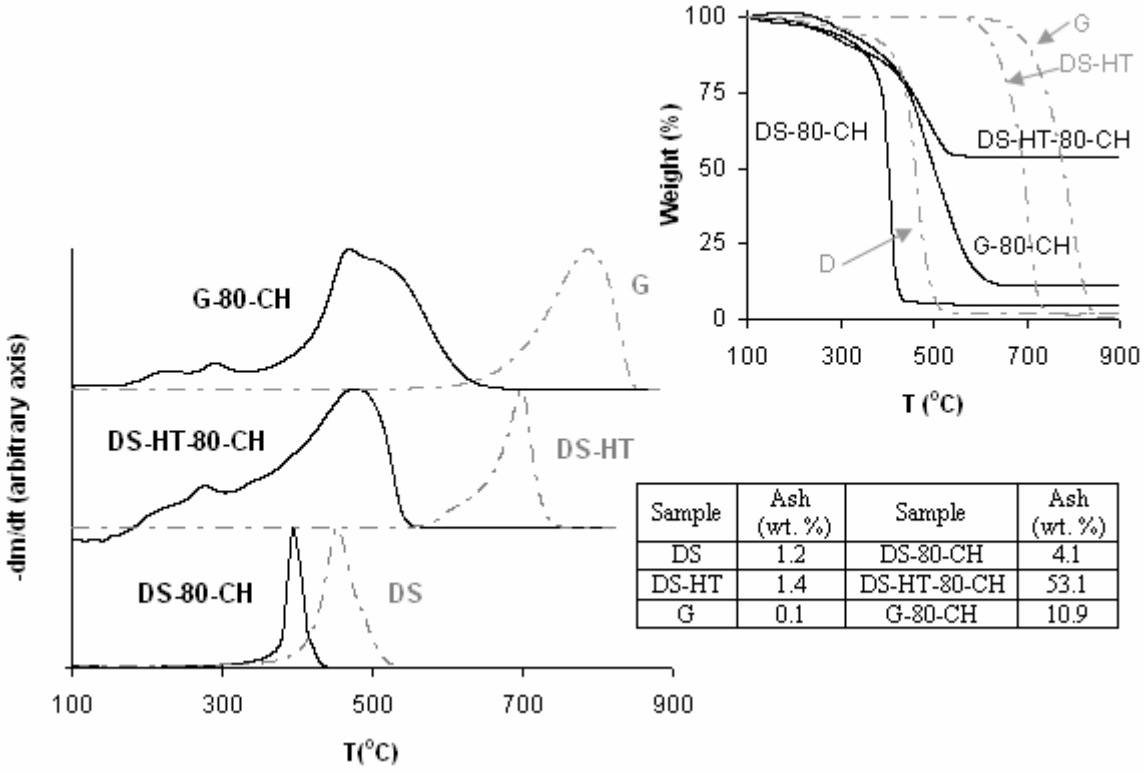

Sample	Ash (wt. %)	Sample	Ash (wt. %)
DS	1.2	DS-80-CH	4.1
DS-HT	1.4	DS-HT-80-CH	53.1
G	0.1	G-80-CH	10.9

Figure 5- 1: Temperature Programmed Oxidation (TPO) profiles and ash contents of the DS, DS-HT and G samples with and without ball milling. Ball milled samples have been represented by solid and dotted lines represent the precursors. Weight loss upon oxidation as a function of the temperature has also been shown (inset)

In all cases, ash content increased with milling (Figure 5- 1, inset), an indication of the expected attrition of the stainless steel milling components. However, the increase for DS-HT is much more significant than the other samples; the reason for this is not clear. XRD of this sample confirms a very high metal content (Figure 5- 2), and the corresponding low carbon content of this material compromises XRD quantification of carbon order. Subsequent analysis of DS-HT-80-CH will be treated with caution due to this anomalously high ash content that may affect characterization that are normalized per unit mass of material.

Reactive ball milling decreases the Lc of G from 718 to 75 Å and the La from 1034 to 170 Å (Figure 5- 2). This indicates that ball milling decreases the overall crystallite size, but certain regions with 3-D graphitic structure remain intact. The decrease in La suggest changes for graphite are not solely due to shearing, 'flaking', or exfoliation; however, it is not clear if the reduction in La is due to introduction of defects or amorphitization of graphite via the breaking of C-C bonds to form nonplanar structures. The low temperature TPO results for G-80CH suggest the latter does occur.

Analysis of Lc and La for the milled coal samples is more problematic due to a large asymmetry in the graphite [002] reflection, and for DS-HT-CH a high metal content that decreases the overall intensity of the carbon reflections and interferes with the carbon [10] peak (Figure 5- 2b). With these caveats, the Lc of DS remains virtually unchanged after milling, but an increased asymmetry in the [002] peak may be a sign of 'gamma-phase' carbon [66, 87], or carbon that is turbostratic in nature with 'defects' in three-dimensional order (Figure 5- 2c). In brief, the gamma phase has been associated with the packing distance of saturated structures such as aliphatic side chains [66].

Changes in Carbon Clustering with Ball Milling (UVR). Somewhat surprisingly, no change is observed in the D:G ratio upon milling for any of the samples (Figure 5- 4, inset); the D:G ratio in UVR is apparently insensitive to the changes seen in TPO and XRD. Shifts in the G peak to lower frequency are an indication that the material has become less 'chain-like' and more graphitic, as decreased G peak frequency has been associated with increased sp^2 clustering [88]. Comparing ball milled samples, sp^2 clustering (i.e. G peak frequency) increases as follows: DS-80CH<DS-HT-80CH<G-

80CH. The trend has not changed compared to the carbon precursors prior to ball milling. No shift is seen in the G peak frequency for G-80CH, a likely reflection of the regions of the material that remain crystalline after ball milling (as evidenced by XRD).

For DS, the G peak frequency shifts from 1602 to 1592 cm^{-1}, indicating milling has increased sp^2 clustering. This is consistent with the increased La of DS-80CH relative to DS. The increase in clustering is greater for DS than DS-HT upon milling, reflecting the fact that DS was more susceptible to structural changes than DS-HT.

A small decrease in the FWHM for the G peak is seen for DS and DS-HT upon milling; the FWHM (G) is a probe of the structural disorder [88]—the smaller the FWHM (G), the less defects and strain in the sp^2-clusters. Thus, the decreases in FWHM (G) suggest ball milling relieves strain in the carbon materials when the carbon precursor has inherent disorder.

Sample	L_c (Å)	L_a(Å)	$d_{(002)}$(Å)
G-80-CH	75 (2)	170 (10)	3.35 (0.00)
G	718 (6)	1034 (28)	3.36 (0.00)

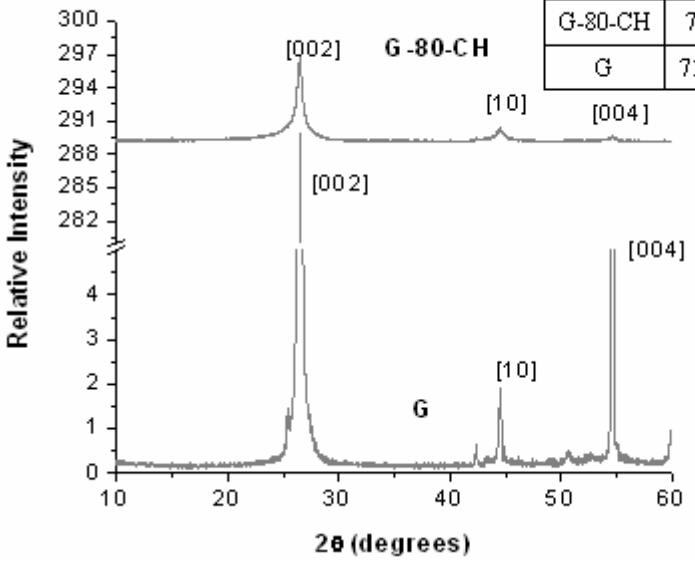

(a)

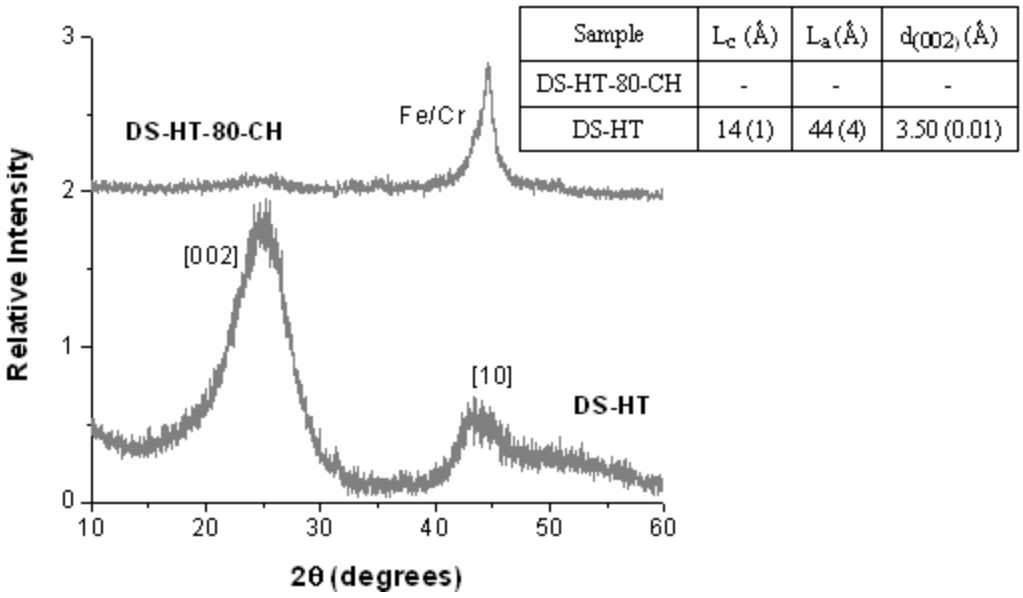

(b)

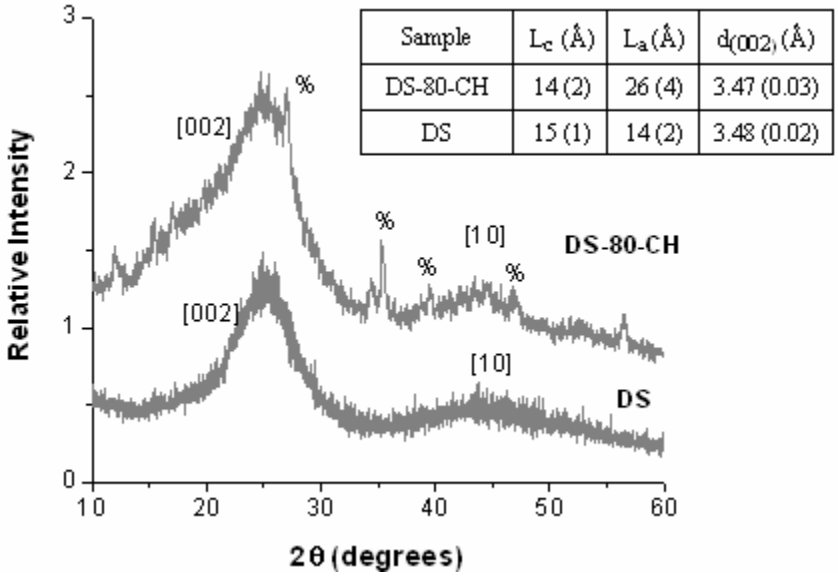

(c)

Figure 5- 2: XRD spectra of the precursor carbon materials before and after ball milling: G and G-80-CH (a), DS-HT and DS-HT-80-CH (b) and DS and DS-80-CH (c). The crystallite sizes and the interlayer spacing's have been shown in the inset table. Iron oxide hydroxide (FeO(OH)) peaks have been represented by a '%'.

Effect of Ball Milling on 3-D Carbon Network and Structure: Solvent Swelling, He Density, and gas adsorption. Solvent swelling and gas adsorption tests provide an indication of three-dimensional association and structure. These tests probe all carbon regions, including those that are graphitic, defected, turbostratic, and amorphous. In contrast, XRD does not probe carbon that is truly amorphous. Gas adsorption studies (including N_2 adsorption and helium density) probe primarily regions that are disordered or amorphous, as these regions have higher surface area for gas adsorption/interaction. Solvent swelling is proportional to cross-link density in polymeric materials, and can provide a qualitative indication of the same in coal structures. Here, the high ash content of DS-HT-80-CH is expected to invalidate these measurements, and thus the DS-HT-80CH data will not be considered further. The change in ash content of the other materials is sufficiently small such that trends may be considered qualitatively. Introduction of metals would be expected to increase helium density; hence, any decreases seen in helium density below are counter to that expected from metal introduction.

Milling of G increases the swelling ratio from 100% to 136% (Table 5- 1). Any remaining graphitic regions within G-80-CH would retain a swelling ratio of 100%, so this increase in swelling is an indication of a turbostratic, defected, or amorphous carbon regions. The increase in swelling is likely related to the carbon that oxidizes at low temperatures in TPO. This effect gives a clear indication that ball milling in cyclohexene is introducing cross-links and disorder into graphite. Helium density of G-80-CH decreased slightly, suggesting certain regions within the amorphous fraction became closed off and inaccessible to helium. Ball milling also increases the swelling ratio of DS from 124% to 150% (Table 5- 1). No net effect is seen for changes in helium density when DS is ball milled, but again, increased ash content would counter possible changes in helium accessibility.

It is interesting to note that the increase in solvent swelling for both G and DS suggests an apparent increase in cross-linking density upon ball milling. For G-80-CH, this is likely due to the amorphous regions that are evident in TPO. For DS-80-CH, no amorphous regions are apparent in TPO, but DS-80-CH does show an increase in gamma-phase carbon in XRD. Thus, the increased cross-linking density for DS is likely

associated with the increase in gamma-phase carbon that indicates an increase in the d-spacing between turbostratic layers. It is not clear whether the increased swelling for DS-80-CH is brought about by exposure to the cyclohexene solvent or ball milling.

Table 5- 1: Solvent swelling ratios and helium densities of the samples DS, DS-HT and G before and after ball milling. The standard deviations (in case of multiple runs) are indicated in parentheses.

Sample	Swelling Ratio (%)	Helium Density (g/cc)	Sample	Swelling Ratio (%)	Helium Density (g/cc)
DS	124 (2)	1.6	DS-80-CH	150	1.6
DS-HT	113 (3)	1.5	DS-HT-80-CH	100	2.6
G	100	2.2	G-80-CH	136	2.0

An increase in the nitrogen BET surface area and porosity is seen upon ball milling for all three samples (Table 5- 2). Here the high ash content of DS-HT-80CH is expected to act as a diluent, and the pore volume of the carbon phase is expected to be higher than reported on the total mass content. The BET surface area of G increases ~10-fold upon ball milling, DS-HT increases ~20-fold (or more if ash is neglected) upon ball milling, and DS-HT-80CH increases ~ 80-fold. After ball milling, the total pore volume of all materials is comparable, 0.2-0.3 cm^3/g; the lower value for DS-HT-80-CH is likely reflective of high ash content. Interestingly, the micropore volume (pore diameter < 20 Å) is increased significantly by reactive ball milling, with the greatest micropore volume (after milling) for DS-80CH. The trend appears to be that the more disordered carbon precursors lead to greater micropore volume upon milling, with the micro-porosity of DS-80CH 3.5-fold greater than DS-HT-80CH, and DS-HT-80CH 10-fold greater than G-80CH. Although TPO indicated that G and DSHT-80CH were more susceptible to change, it appears these changes tended to favor creation of mesoporosity, whereas the subtle changes seen in TPO for DSHT led to regions of microporosity.

The differential pore size distribution (Figure 5- 3) indicates the pores of DS-80-CH may be in the ultra-micropore range, whereas the pores of DS-HT-80CH are primarily >10 Å. Disorder in the carbon precursor appears to lead to a more 'tightly knit' structure upon reactive ball milling with pores in the molecular scale. This is likely related to the increase in gamma-phase carbon seen for DS-HT-80CH in XRD.

Table 5- 2: Nitrogen BET surface area and porosity results of the precursor materials before and after ball milling

Sample	BET surface area (m^2/g)	Micro-pore Volume (cm^3/g)	Total pore volume (cm^3/g)	Sample	BET surface area (m^2/g)	Micro-pore Volume (cm^3/g)	Total pore volume (cm^3/g)
DS	4.1	0.00003	0.008	DS-80-CH	325.7	0.07	0.3
DS-HT	5.3	0.00009	0.008	DS-HT-80-CH	98.0	0.02	0.2
G	9.4	0.00000	0.02	G-80-CH	108.7	0.002	0.3

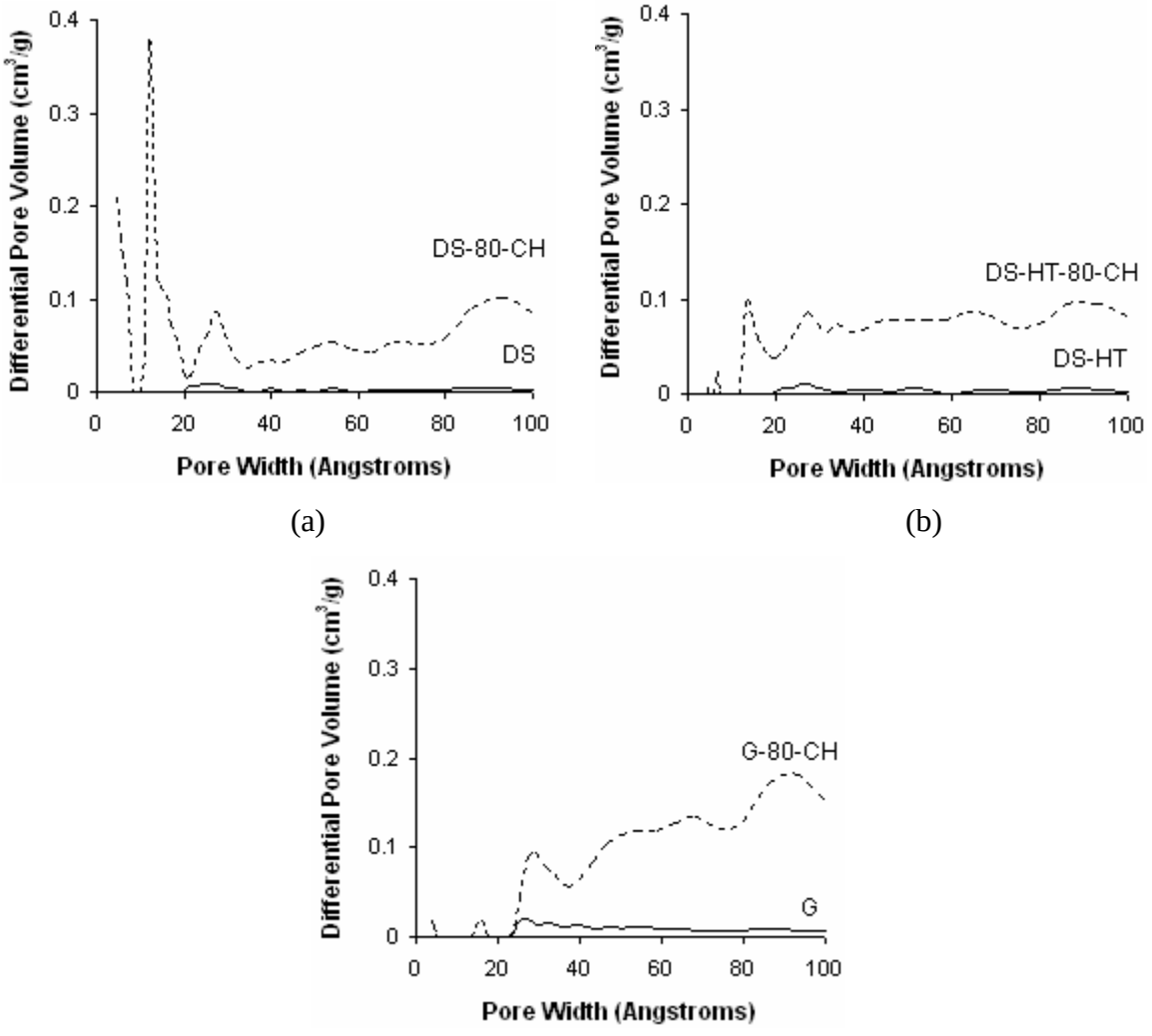

Figure 5- 3: Variation of nitrogen pore volume with pore width for the precursor carbon materials DS, DS-HT and G before (solid lines) and after ('-80-CH' shown with dotted lines) the ball milling process.

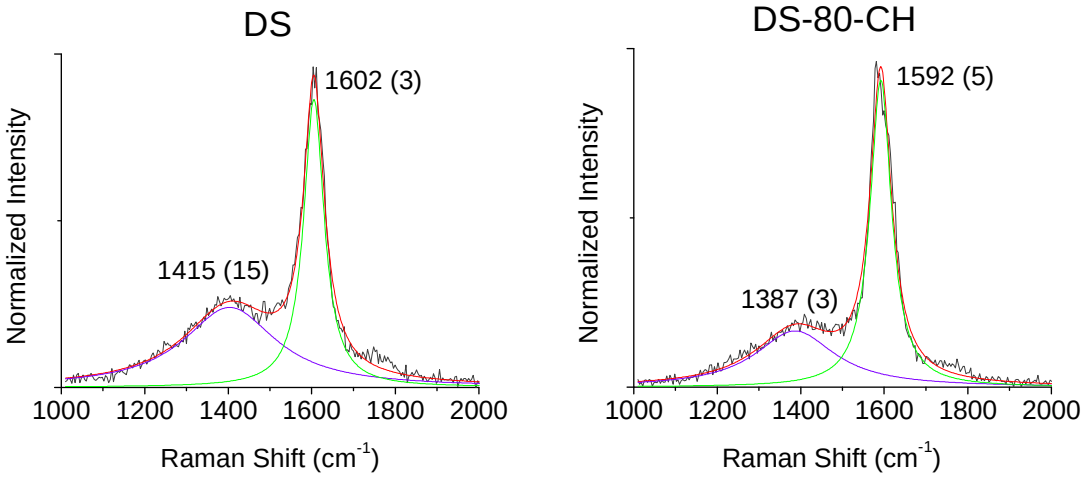

Sample	FWHM		I(D)/I(G)
	D	G	
DS	220 (63)	61 (1)	0.3 (0.0)
DS-80-CH	246 (24)	59 (6)	0.3 (0.0)

(a)

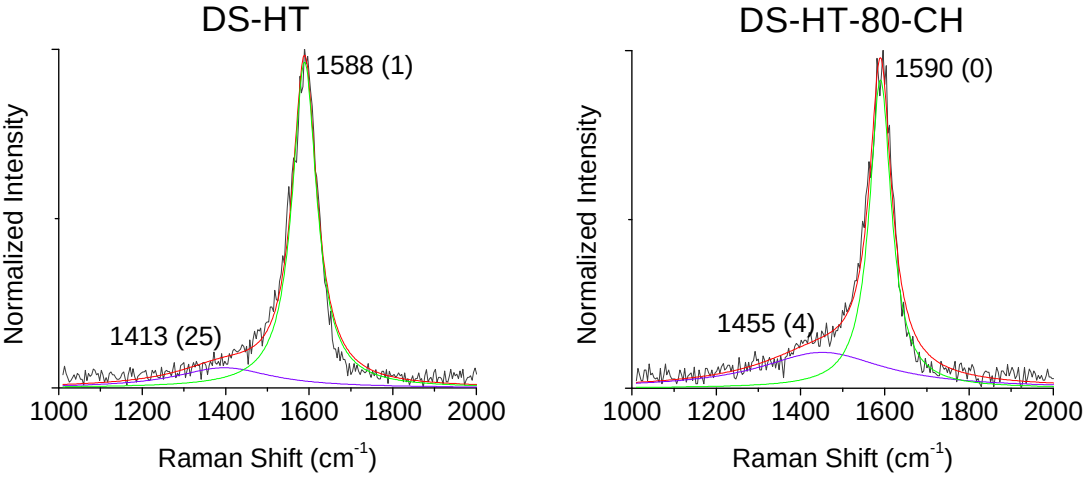

Sample	FWHM		I(D)/I(G)
	D	G	
DS-HT	250 (42)	69 (3)	0.1 (0.0)
DS-HT-80-CH	276 (67)	63 (1)	0.1 (0.0)

(b)

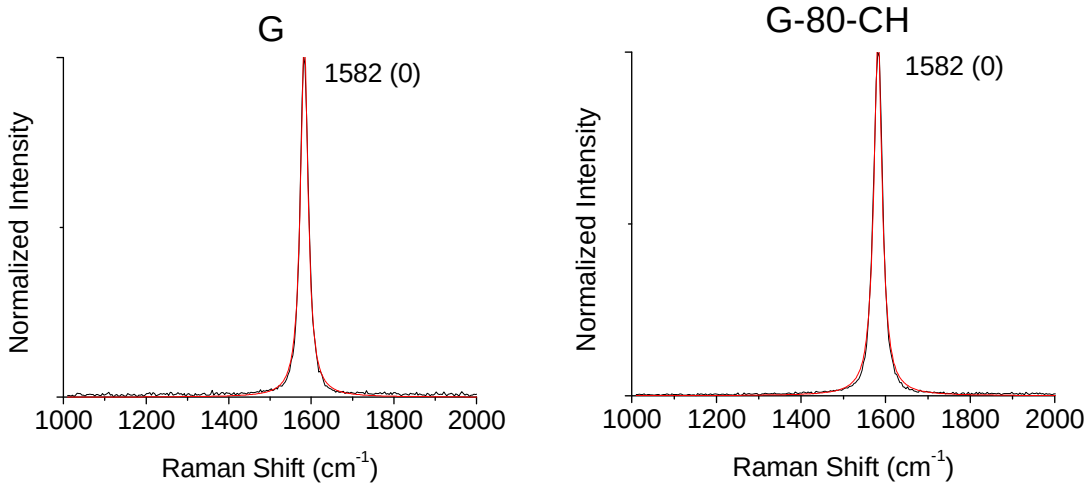

Sample	FWHM (G)
G	24 (1)
G-80-CH	24 (1)

(c)

Figure 5- 4: UV Raman spectra of the precursor carbons before and after ball milling. Peak positions are presented in the figures, along with standard deviations from multiple measurements. The figure also shows the Lorentzian curves fitted to analyze the spectra. The FWHM values of the peaks along with their intensity ratios have also been tabulated.

3. Hydrogen Evolution from Ball milled Samples

TGMS was used to assess possible dehydrogenation of cyclohexene during milling. No benzene or cyclohexene signals are observed in samples that are not ball milled (G and DS, Figure 5- 5). In the samples milled with cyclohexene (i.e. DS-80-CH and G-80-CH), cyclohexene was detected at low temperatures, with the most prominent evolution below ~200 ^{o}C (Figure 5- 5a). The presence of cyclohexene suggests desorption and subsequent evolution of residual cyclohexene from the samples. Benzene evolution for G-80CH paralleled cyclohexene evolution. For DS-80CH, benzene evolution lagged behind cyclohexene, with prominent evolution completed by 400 °C for DS-80CH (Figure 5- 5b). Benzene (and hydrogen) is the expected product of cyclohexene dehydrogenation, thus cyclohexene dehydrogenation leads to hydrogen donation within the ball mill. The difference in the profile of cyclohexene versus

benzene for DS-80CH suggests evolution from the coal structure rather than dehydrogenation of cyclohexene within the TGMS (see also Figure 5- 6b). The evolution of masses 82 and 78 was at higher temperatures for DS-80CH than for G-80CH, suggesting the hydrocarbons were more strongly retained by DS-80CH. This will be discussed further in a subsequent paragraph.

Hydrogen evolution from DS, G, DS-80, DS-80-CH, and G-80-CH has been presented in Figure 5- 5c. G shows no hydrogen signal, and thus the drift in hydrogen baseline for G over the 1000 °C temperature range is a conservative estimate of the error in the measurement (see the error bar in Figure 5- 5c and reproduced in subsequent figures). Hydrogen evolution from DS originates at ~ 600 ˚C, and milling DS without cyclohexene shifts the H_2 evolution to 450 ˚C (Figure 5- 5d). The high temperature hydrogen signals for DS and DS-HT may be attributed to gasification of coal with trace moisture or the evolution of volatile matter. Gasification is possible with trace moisture, as the TGA is not an entirely sealed system.

Low temperature hydrogen evolution is observed for samples milled with cyclohexene, i.e. DS-80CH and G-80CH (Figure 5- 5c). The hydrogen evolution DS-80CH exceeds the graphite drift (scaled in Figure 5- 6), whereas the hydrogen evolution for G-80CH does not. The initial increase in hydrogen evolution for G-80CH appears to follow an initial signal increase in masses 82 and 78. Hydrogen evolution from DS-80CH also increases with masses 82 and 78 initially, but continues to increase after masses 82 and 78 subside. This is evidence of hydrogen trapping in DS-80CH due to reactive ball milling in cyclohexene. As DS also shows hydrogen evolution at temperatures of ~450 ˚C and G-80CH shows hydrogen evolution at ~225 °C, it is the hydrogen evolution at temperatures below 200 °C that is unique to reactive ball milling of DS.

Previously, similar low temperature hydrogen evolution was attributed to dehydrogenation of cyclohexene within the mill and hydrogen trapping [1] within a Buck Mountain anthracite coal. Here, demineralized summit shows qualitatively similar behavior, although the hydrogen evolution is less. The decrease in hydrogen evolution can be attributed to a longer storage time between ball milling and TGMS analysis.

The behavior of ball milled graphite (G-80CH) resembles that seen by Orimo et al, for graphite ball milled in high-pressure hydrogen [40], with a prominent peak at ~400 ˚C. With complementary neutron and X-ray diffraction, Orimo et al attributed this particular peak to hydrogen intercalated between graphene layers. A secondary peak at ~720 °C (990 K) was attributed to hydrogen chemically bound to terminal carbon groups as a result of the hydrogenative ball milling process. Studies by Narayanan and Lueking suggest the sharp peak seen by Orimo et al. at 720 °C was due to metals, as Narayanan and Lueking see a peak that is remarkably similar only upon the addition of magnesium. The low temperature hydrogen evolution seen here for DS-80CH was not seen in the studies of Orimo et al. Also, a prominent peak at 700 °C is not seen for G-80CH, but is seen for DS-80CH at 800 °C and is much more prominent than the high temperature evolution of G-80CH. This can be attributed to the greater number of terminal carbons in DS-80CH available to bind hydrogen, as it did not retain nanocrystalline graphitic regions as did G-80CH.

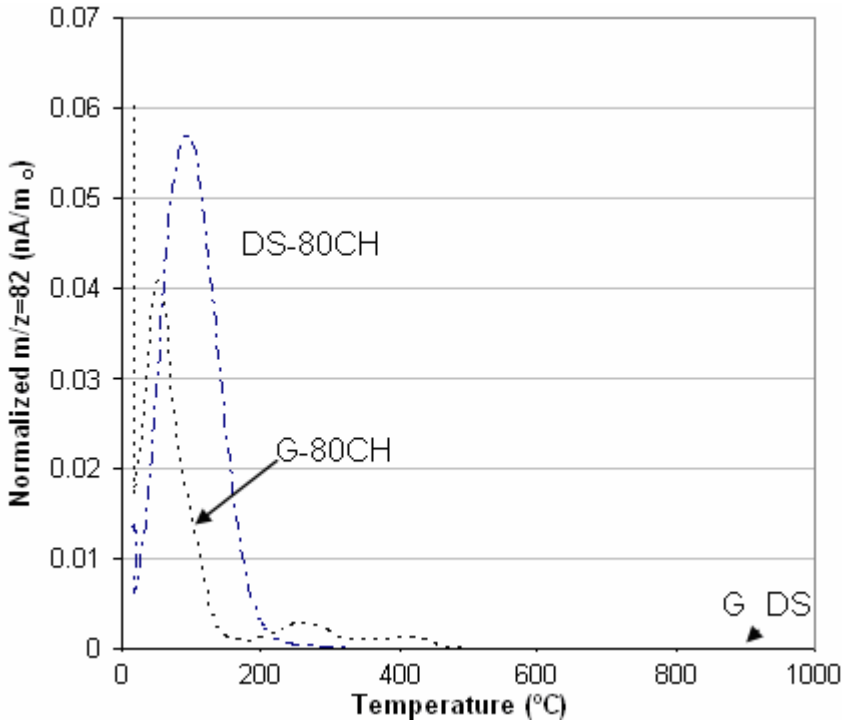

(a)

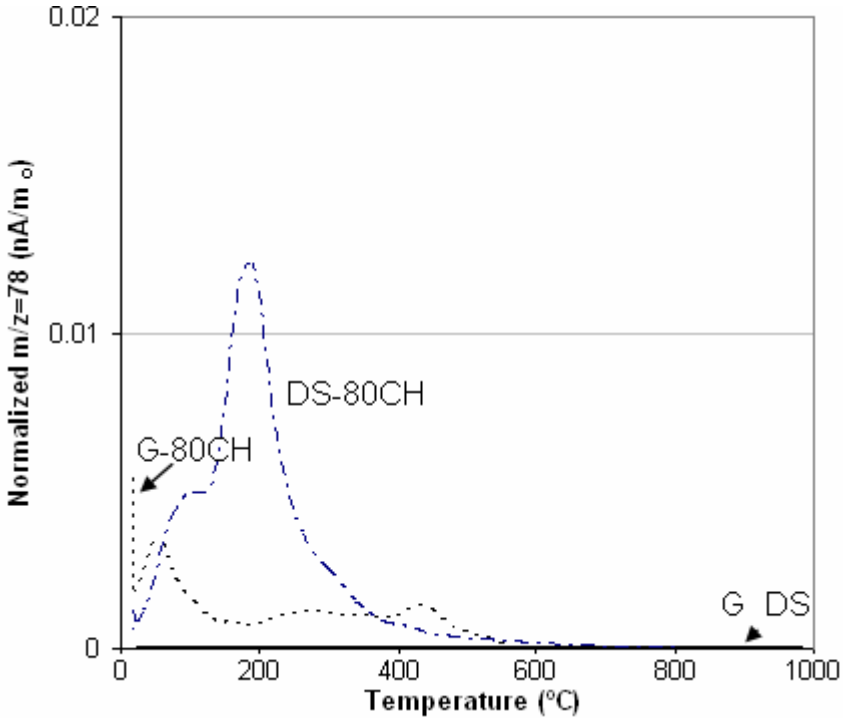
0.02
0.01
0
Normalized m/z=78 (nA/m o)
DS-80CH
G-80CH
G DS
0
200
400
600
800
1000
Temperature (°C)

(b)

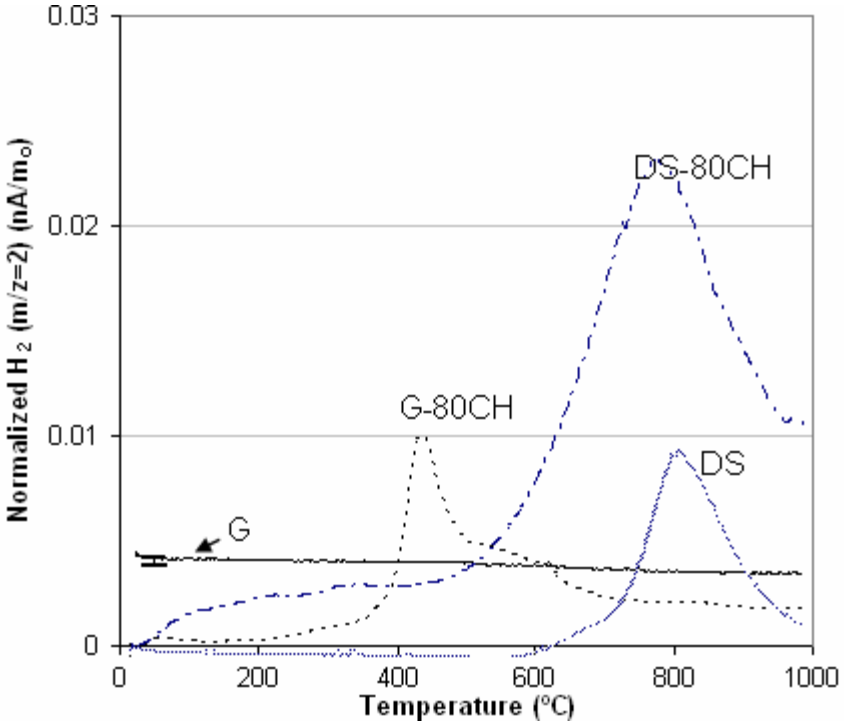
0.03
0.02
0.01
0
Normalized H 2 (m/z=2) (nA/mo)
DS-80CH
G-80CH
DS
G
0
200
400
600
800
1000
Temperature (°C)

(c)

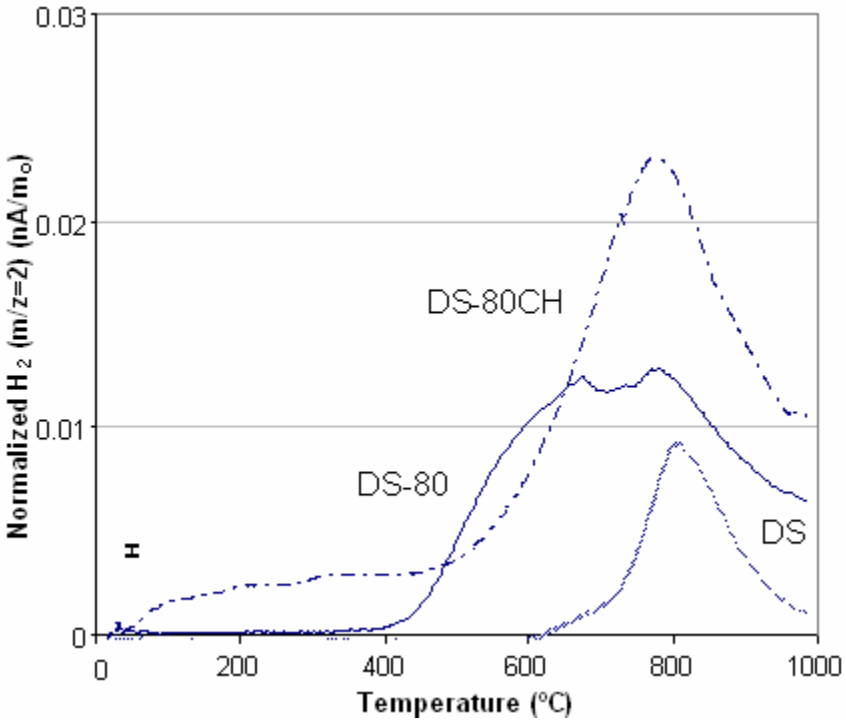

(d)

Figure 5- 5: TGMS results for cyclohexene (a), benzene (b) and hydrogen (c-d) normalized per initial sample mass. G is compared to DS, along with the milled products in (a-c), whereas the variations in DS are compared in (d).

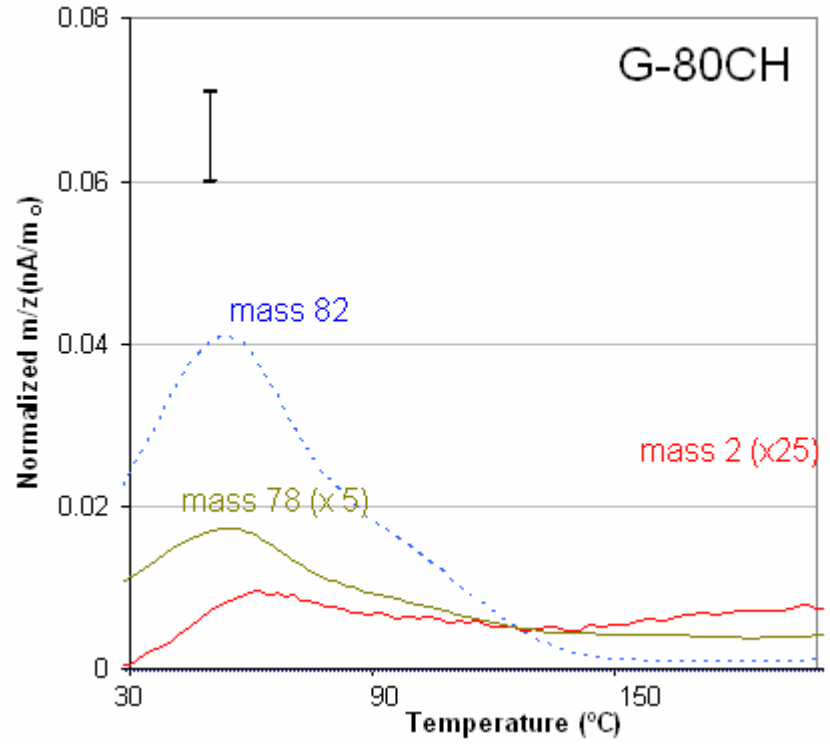

(a)

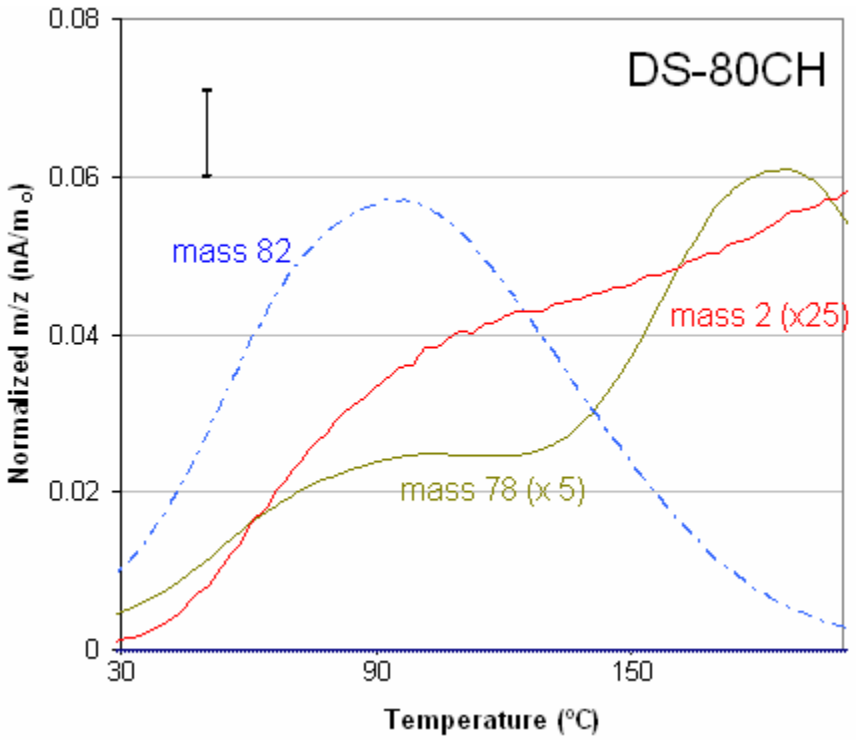

(b)

Figure 5- 6: TGMS results comparing low temperature evolution of G-80CH (a) to DS-80CH (b). Each signal is normalized per initial sample mass, and the signals have been scaled as indicated.

B: Effect of Ball Milling Time on Structural Transformations

DS-20-CH, DS-80-CH and DS-160-CH were prepared by varying the ball milling time of the standard procedure, with 20, 80, and 160 hours of milling, respectively. The experimental results of this section and corresponding trends should be considered a series of preliminary tests. The changes in synthesis conditions are more subtle than in the previous section, and there may be variability introduced by the sequence of the preparation (see also Appendix A). Among other effects, attrition of the stainless steel milling materials is a function of preparation sequence. A discussion on sample variability and repeatability tests is included in Chapter 7 on Suggestions for Future Work..

Evolution of Carbon Structural Changes with Ball Milling Time. TPO studies do not show a wide variation in the oxidation profiles as the milling time is varied (Figure 5- 7). DS-20-CH oxidized at ~ 390 ºC, DS-80-CH ~ 395 ºC and DS-160-CH ~ 410 ºC. The oxidation peak for the precursor material DS was ~ 460 ºC. Thus ball milling for a period of 20 hours increases the reactivity of the carbon which subsequently does not show much of a change as we increase the milling time. A shoulder however forms at ~ 425 ºC as the milling time is increased from 80 to 160 hours. A slight asymmetry/shoulder is barely distinguishable in the case of DS-80-CH. These features cannot be attributed to differences in ash content. This suggests the formation of a carbon of increased order as ball milling time is increased.

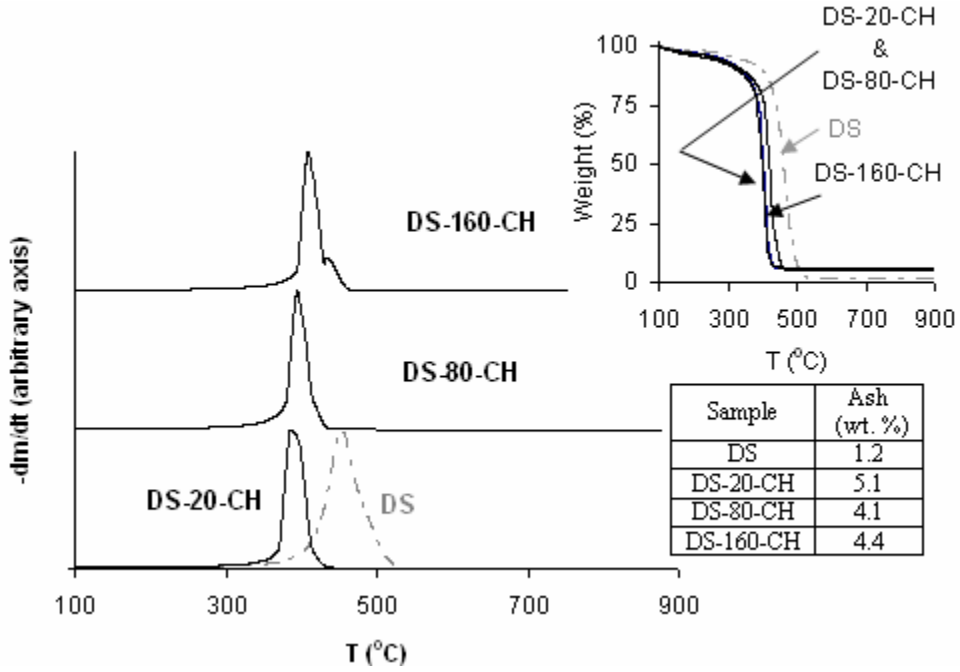

Figure 5- 7: Temperature Programmed Oxidation (TPO) profiles and ash contents of the samples with varying ball milling time DS-20-CH, DS-80-CH, DS-160-CH along with the precursor DS. Weight loss upon oxidation as a function of the temperature and the residual ash contents have also been shown (inset)

The XRD spectra generally shows a broadening of the [002] peak with ball milling (Figure 5- 8). An asymmetric shoulder of the [002] peak is most apparent after 80 hours of milling, and suggests the possible incorporation of the γ phase (DS-80-CH, Figure 5- 8). The intensity of the γ phase seems to increase as the milling time is

increased from 20 to 80 hours and subsequently decreases when milled for 160 hours suggesting the presence of an optimum time. These results suggest a continuous transformation of the carbon structures within the mill with the formation of aliphatic carbons initially which subsequently get amorphitized with increased milling times. However, these results are preliminary and should be reconsidered with additional preparations such that experimental variability may be fully considered.

XRD studies also show the presence of iron oxide hydroxide in the milled samples (denoted by '%', Figure 5- 8) which formed either during milling or storage as the DS precursor had no indication of iron oxide hydroxide.

Sample	L_c (Å)	L_a (Å)	$d_{(002)}$ (Å)
DS-160-CH	14 (2)	12 (4)	3.35 (0.03)
DS-80-CH	14 (1)	26 (4)	3.47 (0.03)
DS-20-CH	10 (1)	26 (4)	3.42 (0.03)
DS	15 (1)	14 (2)	3.48 (0.02)

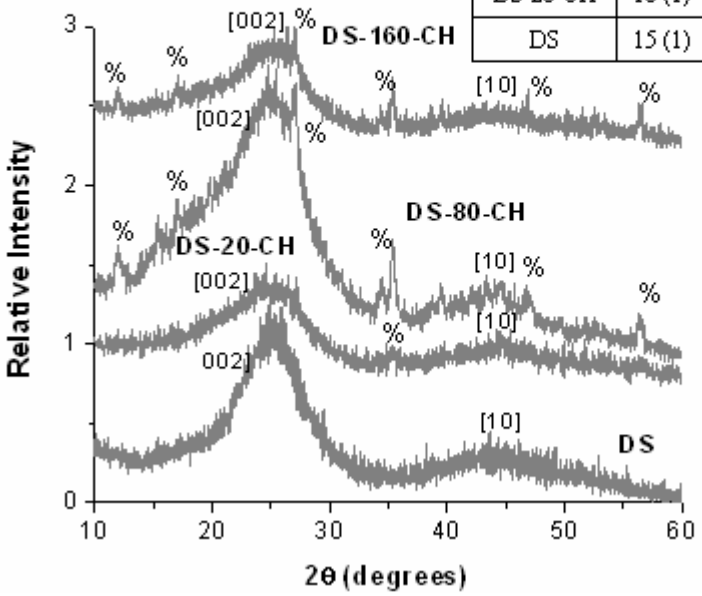

Figure 5- 8: XRD spectra of the samples ball milled for different times DS-20-CH, DS-80-CH, DS-160-CH along with the precursor DS. The crystallite sizes and the interlayer spacing have also been shown (inset). Iron Oxide Hydroxide peaks have been represented by %.

Changes in 3-D Networking with Milling Time. An increase in the solvent swelling ratio is observed after ball milling in cyclohexene (Table 5- 3). Swelling increased with ball milling from a ratio of 124 to 150-170 after ball milling. Ball milling for additional time

first decreased, then increased the solvent swelling ratio. The variation with time (i.e. by +/- 10) is outside the deviation of measurement error, but likely within the variation for sample preparation which was not explored in this work. The swelling ratio is, however, consistent with the trends observed for the gamma phase in XRD. As stated above, the gamma phase has been associated with the packing distance of saturated structures such as aliphatic side chains [66]. Whatever the chemistry of gamma-phase carbon, it is not unexpected that an increased d-spacing within the gamma phase would be more susceptible to solvent swelling. An increase in helium density after 20 hours of milling (Table 5- 3) is likely due to incorporation of metals, as reflected by the increased ash content, and/or an increase in the d-spacing and La of DS-20-CH relative to DS (Figure 5- 8). With increased milling time, helium density decreases, but the changes are small relative to possible variations in synthesis preparation.

Table 5- 3: Solvent swelling ratios and helium densities of the samples milled for 160, 80 and 20 hours along with the precursor DS

Sample	Swelling Ratio (%)	Helium Density (g/cc)
DS-160-CH	160	1.5
DS-80-CH	150	1.6
DS-20-CH	170	1.9
DS	124 (2)	1.6

Nitrogen BET surface area and porosity show an interesting trend with ball milling time. Surface area increases significantly after 20 hours of milling time, increases another ~3-fold with additional milling time, then decreases for extended milling time (

Table 5- 4). The pore size distribution (Figure 5- 9) shows no real trends that would suggest the *distribution* of pores is changing with time. This would be expected if smaller pores were merging to form larger pores, or smaller pores were collapsing or opening up to form larger pores. The studies should be repeated with multiple preparations to ensure the trends are not due to synthesis variations (see Chapter 7).

Table 5- 4: BET surface areas and pore volumes of the samples milled for 160, 80 and 20 hours along with the precursor DS

Sample	BET surface area (m^2/g)	Micro-pore Volume (cm^3/g)	Total pore volume (cm^3/g)
DS-160-CH	109.0	0.01	0.2
DS-80-CH	325.7	0.07	0.3
DS-20-CH	114.3	0.02	0.3
DS	4.1	0.00003	0.008

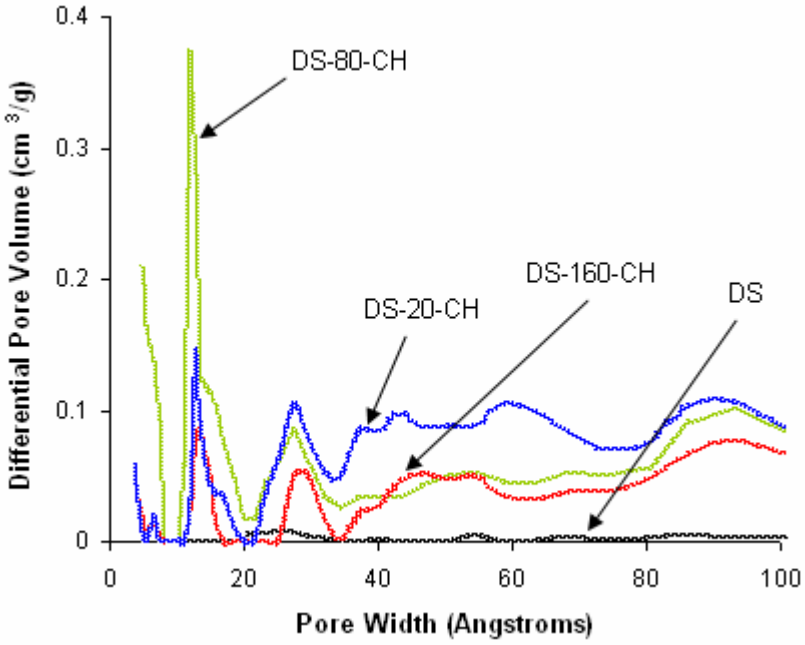

Figure 5- 9: Variation of differential nitrogen pore volume with pore width for the samples milled for different time periods.

Probing changes in local carbon structure with milling time (UVR). The UVR spectra of DS-20-CH and DS-160-CH have been shown in Figure 5- 10 along with the peak positions, intensity ratio of the peaks, and the FWHM values. For comparison, DS and DS-80-CH (from Figure 5- 4a) have been included in the table. The G peak position for DS, DS-20-CH, and DS-160-CH, are all ~1600 cm^{-1} +/- 4 cm^{-1}. The G peak position for

DS-80-CH was higher than the aforementioned, at 1592 cm^{-1}. As stated above, the G peak position decreases with increasing sp^2 clustering [88] for UV Raman excitation. The anomalous trends with milling time suggests the clustering may be more a function of preparation sequence than milling time, as DS-80-CH was prepared much earlier. No real variation is seen with FWHM (G) on ball milling, and the breadth of the D peak makes results of fitting prone to error. No real variations were seen for the D:G ratio.

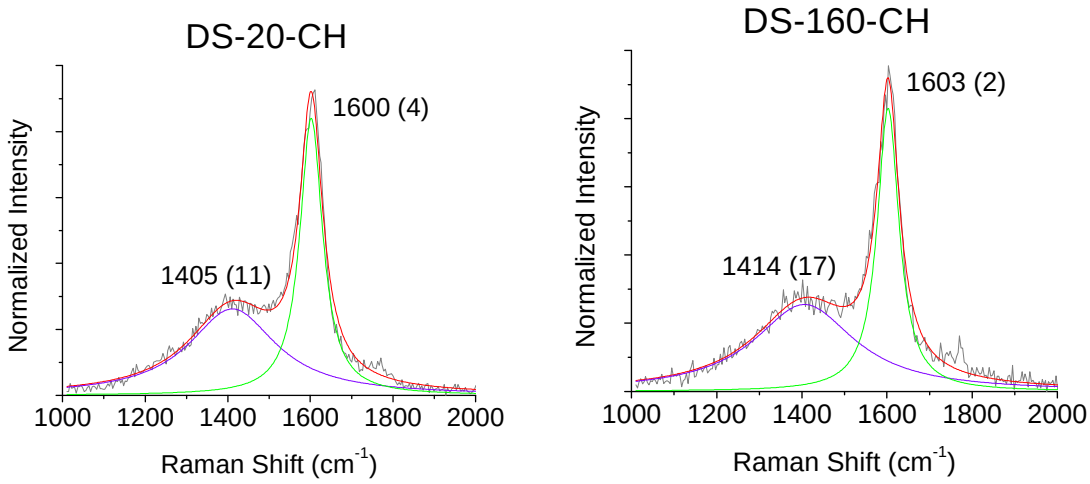

Sample	FWHM		I(D)/I(G)
	D	G	
DS	220 (63)	61 (1)	0.3 (0.0)
DS-20-CH	294 (39)	64 (3)	0.3 (0.1)
DS-80-CH	246 (24)	59 (6)	0.3 (0.0)
DS-160-CH	325 (42)	60 (4)	0.3 (0.0)

Figure 5- 10: UV Raman spectra of the samples with varying milling times. The figure also shows the Lorentzian curves fitted to analyze the spectra. The FWHM values of the D and G along with their intensity ratios (I (D) / I (G)) have also been tabulated. The results of DS and DS-80-CH have also been included in the table for comparison.

XRD, swelling, and nitrogen adsorption results all suggest the possible presence of an optimum time for the changes. However, the changes are subtle, and possibly within the error that would be expected with multiple preparations at the same conditions. Previous reports of milling graphite in the presence of a solvent have shown the presence

of an optimum milling time for the variation of nitrogen surface area [89]. With longer milling times, a shoulder in the TPO profile (at higher temperature) of DS-160-CH suggests that longer milling times may increase order. The preliminary tests seem to suggest that ball milling first disrupts the DS structure, making it more reactive, and that these fragments are then able to graphitize within the mill. However, the analysis should be repeated to ensure the variations are not due to sample preparation sequence and also to take into account natural variations in synthesis. It is recommended that first multiple preparations of one condition be made, such that the experimental error due to variations with preparation sequence can be made. This can be used to assess whether the differences in the above measurements exceed this experimental deviation; if not, there is no need to repeat the above tests.

C: Effect of Cyclohexene on Structural Transformations

Two additional samples were prepared in which the amount of cyclohexene was varied. DS-80-CH (<) and DS-80-CH (>) were prepared with 10 ml and 40 ml cyclohexene respectively. Again, this series of experiments should be considered preliminary tests, as repeatability and natural variations in sample preparation due to synthesis sequence were not yet considered. A discussion on sample variability and repeatability tests is included in Chapter 7 on future work.

TPO characterization showed no effect of the amount of solvent addition to the ball mill. All samples showed one oxidation peak, all within 390-400 ºC (Figure 5- 11). In contrast, the sample milled without cyclohexene (DS-80) had an onset of oxidation at ~ 270 ºC. The lower oxidation temperature of DS-80 may be explained, in part, due to a higher relative ash content; however, the ash content of DS-160CH was comparable and oxidized in the range of 390-400 ºC. Cyclohexene addition to the ball mill thus appears to lead to more stable carbon structures. In general, higher ash content is seen when no solvent is added—both here and in previous studies [32]. Increased milling times lead to increased ash content, but the high ash content in the absence of cyclohexene is not fully understood (Figure 5- 11, inset table).

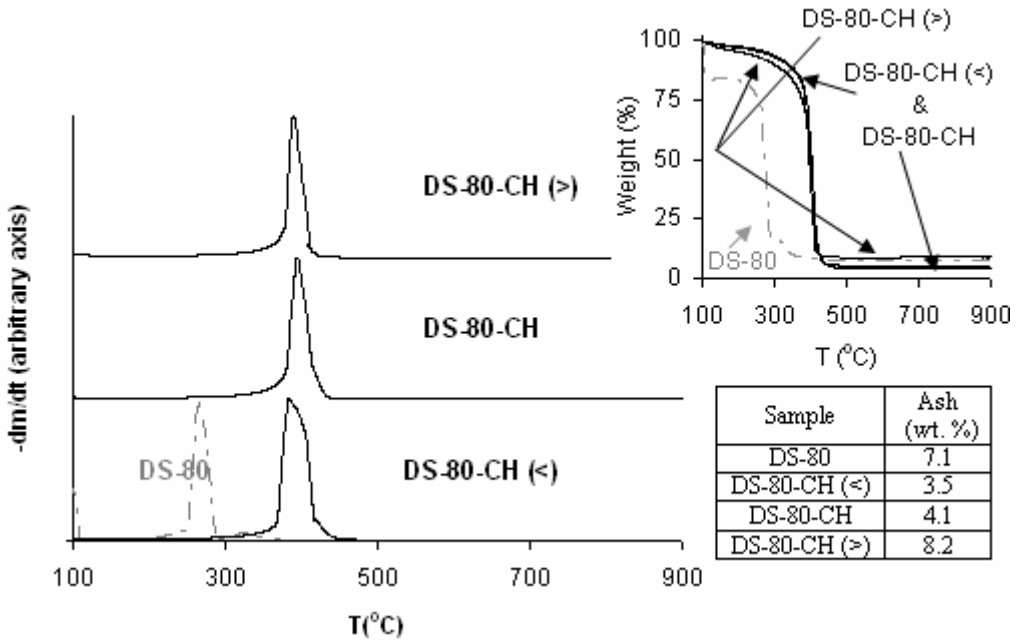

Sample	Ash (wt. %)
DS-80	7.1
DS-80-CH (<)	3.5
DS-80-CH	4.1
DS-80-CH (>)	8.2

Figure 5- 11: Temperature Programmed Oxidation (TPO) profiles and ash contents of the samples ball milled with varying amounts of the solvent cyclohexene including the sample ball milled with no cyclohexene (DS-80). Weight loss upon oxidation as a function of the temperature and the residual ash contents have also been shown (inset)

XRD results indicate that increasing cyclohexene increases the gamma phase contribution, as evidenced by increasing breadth and asymmetry in the peak at ~ 2θ = 26 degrees. This phase is thought to represent saturated structures such as aliphatic side chains, which are grafted to the edges of coal crystallites [66]. These can possibly facilitate structural changes through the formation of cross-links. Certain samples contained iron oxide hydroxide, an effect of attrition of the milling materials with subsequent oxidation (Figure 5- 12).

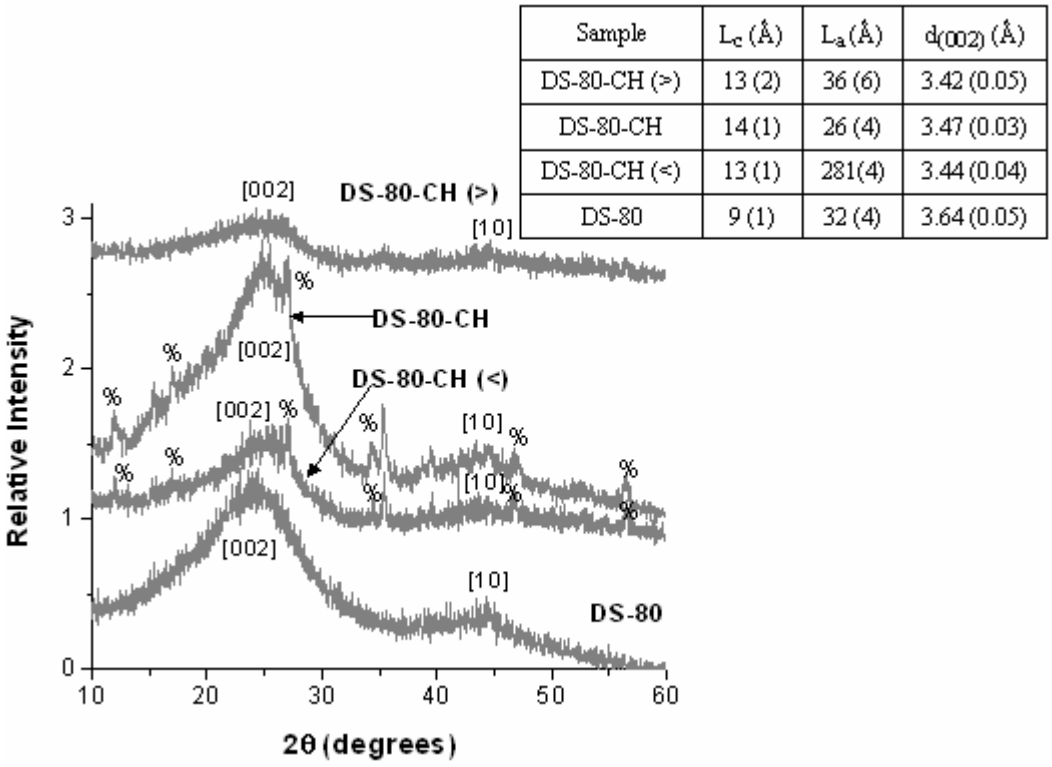

Figure 5- 12: XRD spectra of the samples ball milled with different amounts of solvent DS-80-CH (<), DS-80-CH, DS-80-CH (>) along with the sample ball milled without any solvent (DS-80). The crystallite sizes and the interlayer spacing's have also been shown (inset). Iron Oxide Hydroxide peaks have been represented by %.

Greater swelling is achieved when cyclohexene is added to the ball milling process: the samples containing cyclohexene have a solvent swelling ratio ranging from 150-180% (Table 5- 5). It is not clear, however, if the addition of cyclohexene leads to increased solvent swelling or if it is the combined effect of ball milling in cyclohexene. The solvent swelling ratios appear to follow the trend of the gamma phase observed in XRD. Helium density of samples milled with cyclohexene is comparable to DS. Milling without cyclohexene decreases the solvent swelling ratio to 117%, a likely effect of 'compaction', which is also reflected by XRD and an increased helium density.

Table 5- 5: Solvent swelling ratios and helium densities of the samples milled with varying amounts of cyclohexene (DS-80 with no cyclohexene and 10 ml, 20ml and 40 ml cyclohexene used for the preparation of samples DS-80-CH (<), DS-80-CH and DS-80-CH (>) respectively; DS added for comparison)

Sample	Swelling Ratio (%)	Helium Density (g/cc)
DS-80-CH (>)	180	1.6
DS-80-CH	150	1.6
DS-80-CH (<)	170	1.5
DS-80	117	1.8
DS	124 (2)	1.6

The BET surface area and pore volume shows a significant increase on milling with cyclohexene in comparison to the results obtained from dry milling (Table 5- 6). Once again, the DS-80-CH sample showed the highest surface area and porosity when compared to the samples ball milled with varying amounts of the solvent cyclohexene. The unique behavior of DS-80-CH suggests sample preparation order is important, as this sample was prepared earlier. Figure 5- 13 further elucidates this variation in the differential pore volume with the pore width. It is seen that both DS-80-CH and DS-80-CH (>) have higher micro-pore volumes in comparison with DS-80. However DS-80-CH (<) has a lower micro-pore volume.

Table 5- 6: BET surface areas and pore volumes of the samples milled with varying amounts of cyclohexene (DS-80 with no cyclohexene and 10 ml, 20ml and 40 ml cyclohexene used for the preparation of samples DS-80-CH (<), DS-80-CH and DS-80-CH (>) respectively; DS added for comparison)

Sample	BET surface area (m^2/g)	Micro-pore Volume (cm^3/g)	Total pore volume (cm^3/g)
DS-80-CH (>)	76.0	0.01	0.2
DS-80-CH	325.7	0.07	0.3
DS-80-CH (<)	67.5	0.001	0.2
DS-80	33.6	0.006	0.06
DS	4.1	0.00003	0.008

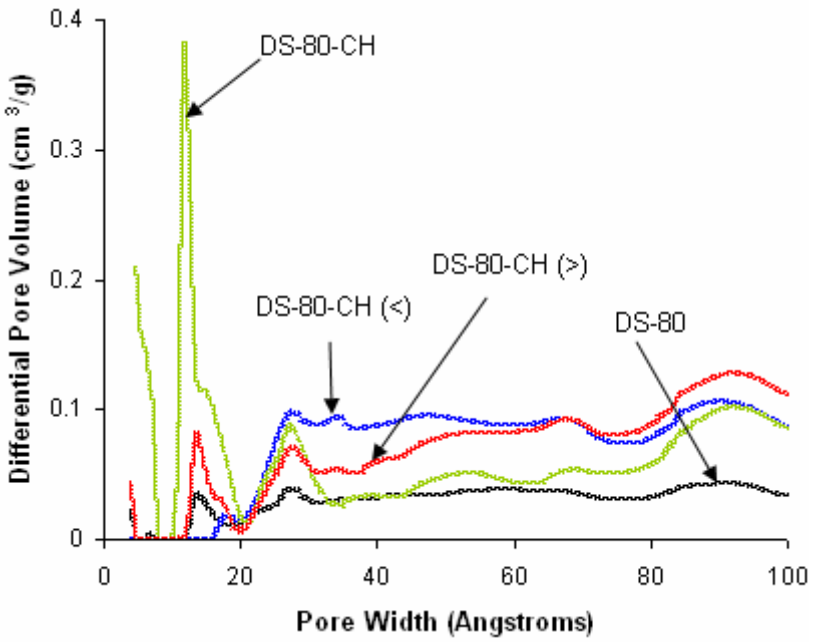

Figure 5- 13: Variation of nitrogen pore volume with pore width for the samples milled with different amounts of the solvent cyclohexene (DS-80-CH (<), DS-80-CH and DS-80-CH (>)) and with no cyclohexene (DS-80).

The UVR of DS-80, DS-80CH(<) , and DS-80CH(>) show subtle differences (Figure 5- 14). The G peak position of and DS-80CH(>) is at a higher frequency than the other materials and outside deviation, suggesting added cyclohexene decreases sp^2 clustering [88] and leads to a more polymeric material. The D:G ratio for DS-80 is slightly higher than the other samples, but within experimental error. UVR did not provide substantial information on the formation of cross-links in the structure.

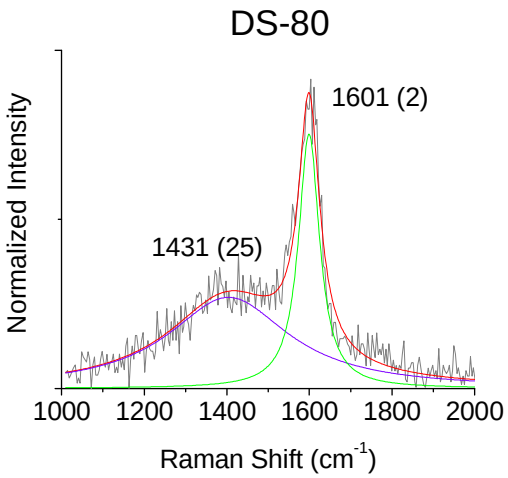

(a)

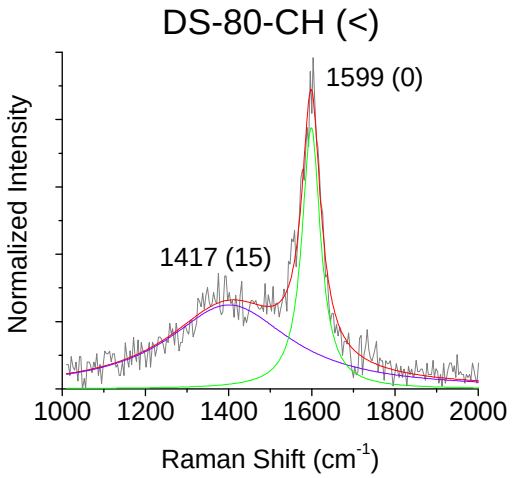

(b)

Sample	FWHM		I(D)/I(G)
	D	G	
DS-80	468 (153)	58 (6)	0.4 (0.1)
DS-80-CH (<)	431 (64)	50 (4)	0.3 (0.0)
DS-80-CH	246 (24)	59 (6)	0.3 (0.0)
DS-80-CH (>)	377 (145)	59 (6)	0.3 (0.0)

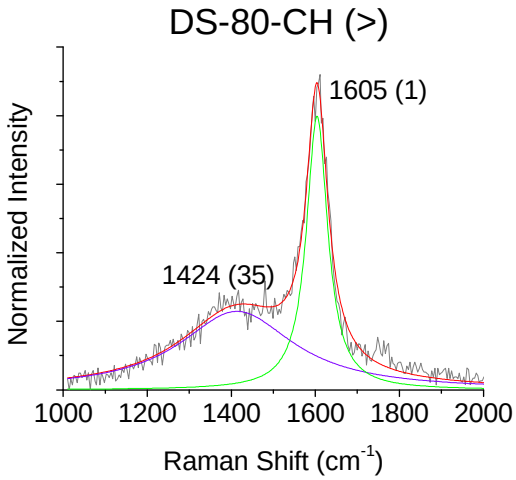

(c)

Figure 5- 14: UVR for samples with varying amounts of cyclohexene, with results from Lorentzian fitting of the peaks tabulated in the inset. DS-80-CH has been included in the table for comparison.

Cyclohexene is playing a crucial role in the structural changes induced by ball milling. Milling in cyclohexene leads to materials that oxidize at higher temperatures, and the differences cannot fully be accounted for by differences in metal content. An interesting correlation between the presence of gamma phase carbon in XRD and swelling results is noted; but it is not clear the role of ball milling versus simple cyclohexene addition in these effects. Subtle variations in UVR suggest that added cyclohexene may lead to a more polymeric carbon form. Changes for surface area and porosity are drastic upon ball milling in cyclohexene, with an indication the process is creating microporosity within the material. It is not clear whether the increased microporosity is due to chemical changes within the material or simple swelling upon the introduction of cyclohexene. Further sample preparations are needed to draw any conclusions regarding trends.

Summary and Conclusions

Demineralized Summit anthracite as heat treated at 1673 K to produce a more ordered structure with similar origin. DS, DS-HT, and G were ball milled in cyclohexene to determine the effect of structural order of the precursor in structural changes induced by ball milling. Cyclohexene dehydrogenated within the mill, as evidenced by hydrogen and benzene dehydrogenation products in TGMS.

Precursor order had a substantial effect on the structural changes seen by reactive ball milling in cyclohexene. Ball milling of graphite (G), the most ordered precursor, led to a heterogeneous structure consisting of both amorphous (TPO) and graphitic carbon (XRD, UVR). The graphite crystallites were an order of magnitude smaller (Lc and La in XRD) after milling. Amorphitization led to an increased surface area that was made up of primarily mesoporous carbon that swelled upon the addition of a solvent. The swelling was an indication of regions with a networked, three-dimensional structure.

The least ordered precursor, DS, formed ‘gamma-phase’ carbon in the ball mill that still had some three-dimensional order, evidenced by XRD. Ball milling led to increased clustering (chain-like carbon) as evidenced by the G-peak position in UVR and La in XRD. The increased clustering may have been due to either reactions with

cyclohexene or graphitization. There was no evidence of low temperature oxidation characteristic of truly amorphous carbon in TPO. Ball milling of DS led to the most significant increase in surface area, with significant microporosity. Swelling increased upon ball milling, indicating a three-dimensional networked structure.

Annealing DS prior to milling reduced the effect of milling, likely due to lowering the mobility of carbon fractions within the structure. Similar to graphite, DS-HT-80CH had evidence for amorphous carbon in TPO, an increased surface area relative to its precursor that was made up of pores that were both micro- and mesoporous.

DS-80CH retained more hydrogen than G-80CH. For DS-80CH, the hydrogen evolved at temperatures below 200 °C and did not mirror cyclohexene and benzene evolution, even after extensive storage prior to the measurement. Low temperature hydrogen evolution from ball milled graphite mirror cyclohexene and benzene evolution. The hydrogen retained for long periods in DS-80CH that evolved at low temperatures may be a function of the microporosity, the gamma-phrase carbon indicating an expanded turbostratic structure. The high temperature hydrogen evolution from DS-80CH follows that seen previously for hydrogenated graphite that was attributed to hydrogenation of terminal carbon in nanostructured carbon entities. The role of hydrogen trapping and the observation of gamma-phase carbon will be discussed as possible future work.

The changes in carbon structure as a function of cyclohexene addition and milling time were more subtle, and it is not clear if the trends surpass variations in sample preparation.

Chapter 6

Summary and Conclusions

Project 1: Structural Transformations with Ball Milling

TPO studies of the samples indicated a change in the carbon reactivity because of structural changes upon acid and base treatment (samples with '-AB'). This was more prominent in the samples which were heat treated (samples with 'HT-AB'). Also the formation of carbon of lesser reactivity (more ordered) upon the acid and base treatment was seen in all the heat treated samples but mDBMT-HT-AB suggesting that metals were crucial to the presence of the high temperature TPO peak (~ 600 ºC).

X-ray diffractograms confirmed the formation of iron carbides on ball milling and subsequently heat treating the samples. In contrast metal peaks were more prominent in the samples without a thermal anneal. Heat treatment was critical to the formation of iron carbides. Subsequent treatment with HCl brought about a reduction in the intensity of the iron carbide/iron peaks as seen from the XRD results of the heat treated samples. Upon treatment with NaOH, the XRD spectra were masked with calcite peaks which resulted because of the contamination in the de-ionized water used. Some iron carbide peaks of lesser intensity were still observed.

UVR characterization performed on the '-AB' samples showed the presence of a small peak in the diamond region (1332 cm^{-1}) for the mBMT-HT-AB sample. This can be due to structural changes leading to the formation of sp^3 carbons.

In conclusion, it was shown that ball milling introduces metals, and subsequent heat treatment leads to the formation of iron carbide. Treatment with HCl and NaOH leads to the formation of carbon of different reactivities and ordering. It is probable that nano-diamond might be a product of the process as was indicative of the UVR results. Further studies are warranted.

Project 2: Structural Transformations and the Evolution of Hydrogen

The results conclusively showed that ball milling leads to structural changes in carbon and that cyclohexene dehydrogenates within the mill. The precursor order influences the mechanism of structural changes that occur during ball milling. For graphite, crystallite diameter is reduces with amorphitization. For DS anthracite coal, La increases, clustering increases, gamma-phase carbon is formed and the resulting material has significant microporosity. Milled DS anthracite coal differs substantially from milled graphite. Notably, milled DS anthracite coal had low temperature hydrogen evolution that surpasses trends that mirrored cyclohexene and benzene evolution. Low temperature hydrogen evolution from milled graphite followed cyclohexene evolution.

Chapter 7

Suggestions for Future Work

Project 1: Structural Transformations with Ball Milling

The scope of the work was to investigate the formation of nano-diamond. Previous nano-diamond observation was made through Transmission Electron Microscopy (TEM) studies. It is hence recommended that TEM characterization is performed on the sample in which sp^3 hybridized carbon presence was indicated by UVR studies. Further the XRD spectra were masked to a large extent by calcite peaks which were present in the de-ionized water used in the studies. Future studies should take the precaution of ascertaining the quality of the de-ionized water used. It is also recommended that a more homogenous carbon sample is used as precursor along with a ball mill that does not contaminate the sample during the course of its preparation. The reactions can also be explored independently to determine if the formation of nano-diamond is possible.

Project 2: Hydrogen Evolution

The results indicated no evidence of any significant low temperature hydrogen evolution. Since in this study demineralized coal was used as opposed to non-demineralized coal in the previous study where hydrogen storage and trapping was reported by Lueking et al., It is recommended that the role of metals and metal carbides on the process be investigated. Also, in this study the samples were not tested as a function of time because of technical problems encountered with the equipment. Future work may be done so as to study the process of hydrogen storage and trapping as a function of time. Apart from sample age, the variability in the preparation sequence is also recommended for investigation. This is important since milling leads to a gradual breakdown of the bowl and the balls. Hence the samples lower down in the sample preparation order are more susceptible to contamination. This may in part be responsible for the behavior of the sample. In addition to that, the role of the coal structure on the hydrogen evolution properties can be explored. Since high porosity was observed in the

surface area and porosity analysis, the investigation of the process for the activation of anthracites for the preparation of activated carbon is recommended. The correlation of the gamma phase (observed in the XRD studies) with the hydrogen trapped in the samples is another aspect which can be further investigated. In particular more studies should be focused on the hydrogen evolution from samples where a more pronounced gamma peak is observed to check if the presence of aliphatic side chains (which is indicated by the gamma phase) contributes to greater hydrogen storage and trapping and subsequent evolution.

Appendix A

Coal Selection and Sample Preparation

Five anthracite coals, before and after demineralization, were screened to assess the order and 'graphitizability' of the coals upon ball milling. The objective was to anticipate the degree of ordering or structural change that may occur during the ball milling process. TPO and XRD were used during the initial coal selection process. As described in Chapter 3 the five coals were LCNN, Summit, AFM 800, AFM 2600 and PSOC 1515. The demineralized coals will be referred as D-LCNN, DS (for demineralized summit), D-AFM 800, D-AFM 2600 and D-PSOC 1515, respectively. The information about the coals has been presented in Table A- 1.

Table A- 1: Proximate Analysis of the five coal samples

Property	Summit	PSOC 1515	AFM2600	AFM800	LCNN
Ash (dry wt %)	17.6	29.5	10.2	6.8	6.7
VM (dry wt %)	11.1	8.4	4.9	3.5	4.5
FC (dry wt %)	71.2	62.3	84.9	89.7	88.3
VM (daf wt %)	13.5	11.9	5.4	3.8	4.8
FC (daf wt %)	86.5	88.1	94.6	96.2	95.2

The TPO results for the 5 coals have been shown in Figure A- 1. In each case, the thermal anneal (dotted lines, Figure A- 1) led to a higher oxidation temperature compared to the precursor coal (solid lines, Figure A- 1). In general, higher oxidation temperatures are indicative of carbon materials with greater ordering, as discussed in Chapter 2. Increased ordering with heat treatment is consistent with the behavior expected for 'graphitizing' carbons (as defined by Franklin [57]). Strong cross-links hinder the process of graphitization as discussed also in Chapter 2.

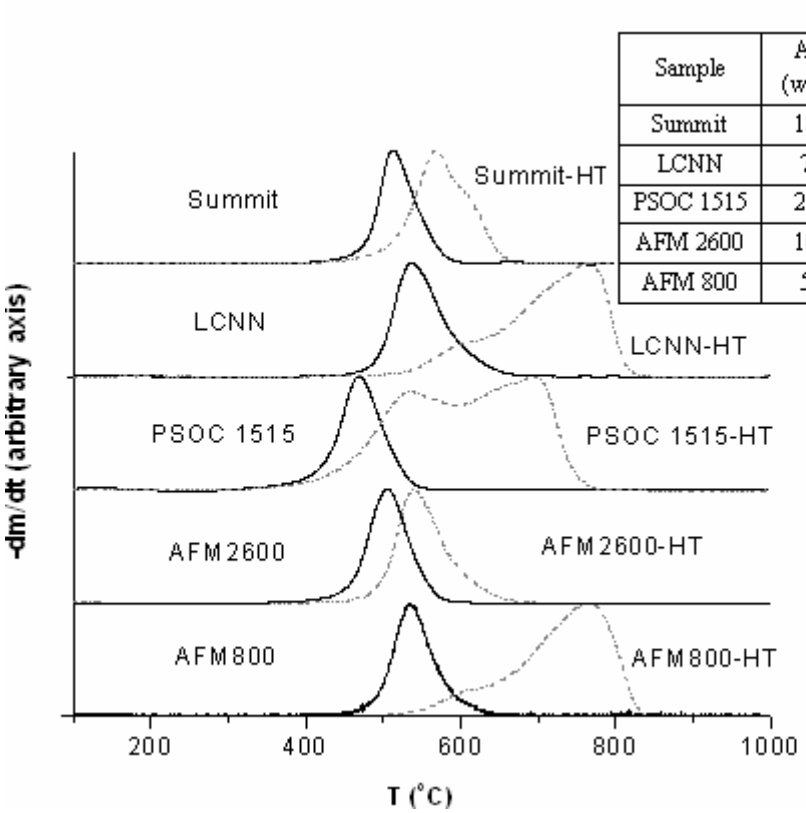

Sample	Ash (wt. %)	Sample	Ash (wt. %)
Summit	18.6	Summit-HT	8.8
LCNN	7.0	LCNN-HT	21.8
PSOC 1515	25.9	PSOC 1515-HT	32.2
AFM 2600	10.0	AFM 2600-HT	7.0
AFM 800	5.7	AFM 800-HT	5.7

Figure A- 1: Temperature Programmed Oxidation (TPO) profiles and ash contents of the 5 coals. Samples omitting and including the high-temperature (HT) anneal are represented by solid and dotted lines, respectively.

The amount of the temperature shift upon heat treatment was dependent upon the coal precursor and the inherent structural properties of a particular coal. It gives an indication on the structural rearranging of the coal upon heat treatment. The shift to higher oxidation temperature upon thermal anneal is most pronounced for AFM 800, PSOC 1515 and LCNN. For AFM 800, the temperature shifts from ~535 ºC to ~750 ºC (with a shoulder ~ 600 ºC), for PSOC 1515 it shifts from ~470 ºC to ~700 ºC (with a shoulder ~ 530 ºC) and for LCNN-HT, it is from ~540 ºC to ~770 ºC (with a shoulder around ~ 600 ºC). Interestingly, all three of these coals exhibit somewhat of a bimodal oxidation profile, suggesting regions of differing reactivity. Coals with a lesser shift in the oxidative reactivity upon thermal anneal suggest the presence of a relatively more crosslinked structure. For example, the oxidation of Summit coal shifts only 60 ^{o}C (from a temperature of ~510 ºC to ~570 ºC) while the shift for AFM-2600 is only 40 C (with a

shift from ~500 ºC to ~540 ºC). Both Summit and AFM-2600 have no significant shoulders, suggesting more uniform carbon reactivity after thermal anneal. The shift in Summit and AFM-2600 suggests a low degree of graphitization at the heat treatment temperature of 1673 K.

Changes in ash content upon thermal anneal provide an indication of whether volatile matter is lost during the heat treatment step or whether metal carbides are formed. If volatile matter is lost, the residual ash content is expected to decrease, whereas an increase in ash content is indicative of the formation of metal carbides as discussed by Lueking et al. [43]. The residual ash contents of PSOC 1515 and LCNN increase on heat treatment from 25.9 to 32.2 % and 7.0 to 21.8 %, indicating a loss of volatile matter upon thermal anneal. For AFM 800 it remains stable at 5.7 %, suggesting little volatile matter in the coal and no real formation of carbides. Summit and AFM 2600 decrease in residual ash content upon thermal anneal from 18.6% to 8.8% and 10.0 % to 7.0 % respectively; these changes are significant and above 'sampling error' and suggest formation of metal carbides.

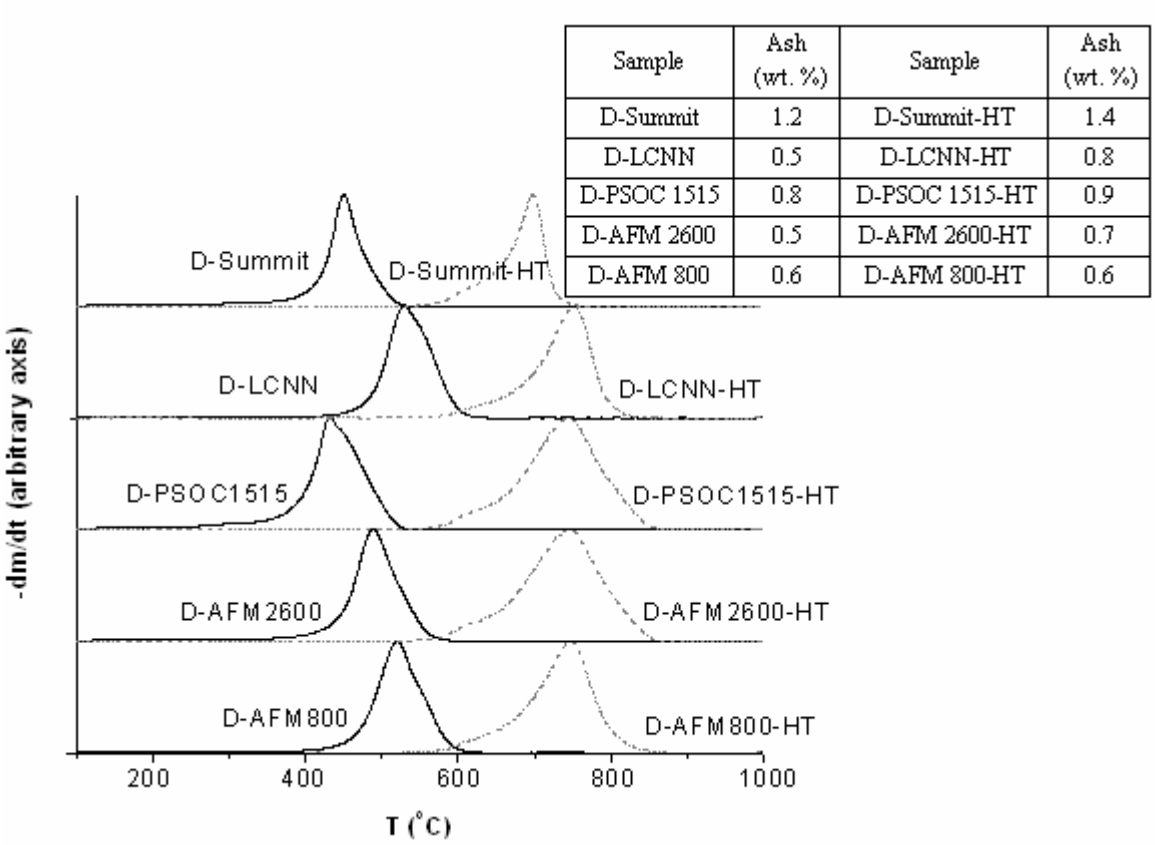

Sample	Ash (wt. %)	Sample	Ash (wt. %)
D-Summit	1.2	D-Summit-HT	1.4
D-LCNN	0.5	D-LCNN-HT	0.8
D-PSOC 1515	0.8	D-PSOC 1515-HT	0.9
D-AFM 2600	0.5	D-AFM 2600-HT	0.7
D-AFM 800	0.6	D-AFM 800-HT	0.6

Figure A- 2: Temperature Programmed Oxidation (TPO) profiles and ash contents of the 5 demineralized coals. Samples omitting and including the high-temperature (HT) anneal are represented by solid and dotted lines, respectively.

The TPO results of the demineralized coals have been shown in Figure A- 2. The following shifts in the thermal anneal are observed upon heat treatment of the demineralized samples: D-PSOC 1515 (from ~430 ºC to ~750 ºC), DS (~450 ºC to ~700 ºC) D-LCNN (~530 ºC to ~750 ºC) AFM 2600 (~490 ºC to ~750 ºC) and AFM 800 (~520 ºC to ~750 ºC). In contrast to the results for the 'as-received' coals in Figure A- 2, heat treatment now leads to a significant shift in the oxidation temperatures of Summit and AFM 2600. Demineralization has also led to a significant reduction in the mineral matter of the coal. In addition, the removal of mineral matter prior to thermal annealing has led to a change in the number of coals exhibiting an increase of residual ash upon thermal annealing. Now, four coals increase residual ash upon thermal annealing, but the relative change in ash content is much less pronounced and likely within experimental error for

all samples. Demineralization has also removed the low temperature shoulders observed with the thermally annealed PSOC-1515, AFM-800 and LCNN coals. This indicates that those peaks might be due to the catalytic effect on the oxidation by the minerals.

The XRD results of the raw coals with and without the thermal anneal are shown in Figure A- 3. Prior to thermal anneal, the coals generally exhibit broad diffraction beaks at ~26° and ~40-45°, which are attributable to the characteristic [002] and [10] peaks for graphite. However, the presence of additional diffraction peaks indicates the presence of minerals. Thermal annealing leads to a more ordered structure, as evidenced by an increased intensity of the [002] and the [10] peaks attributable to graphite. It is observed that the raw coal samples with comparatively higher residual ash contents namely PSOC 1515 and Summit with 25.9 % and 18.5 % respectively (Figure A- 1, inset) are indicative of more mineral peaks in the XRD profile (Figure A- 3c and a respectively).

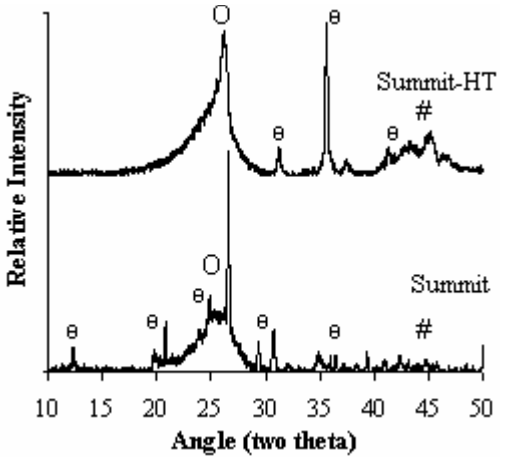

(a)

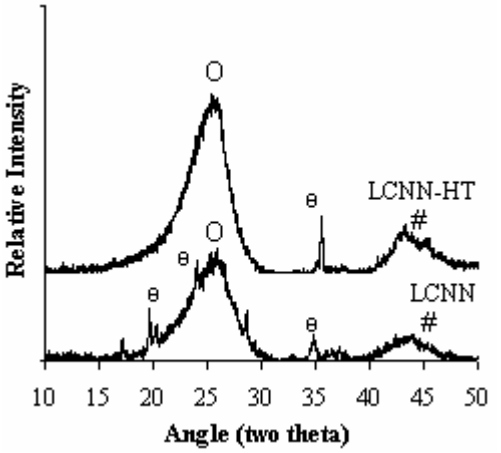

(b)

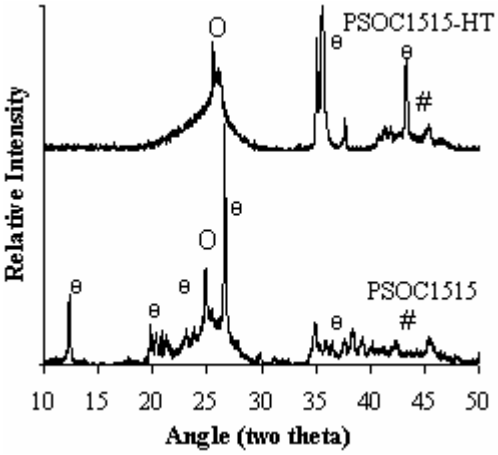

(c)

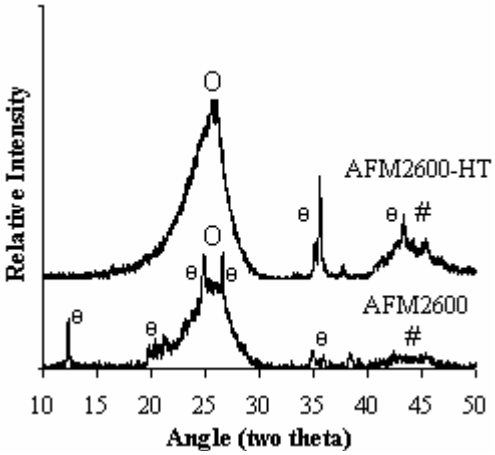

(d)

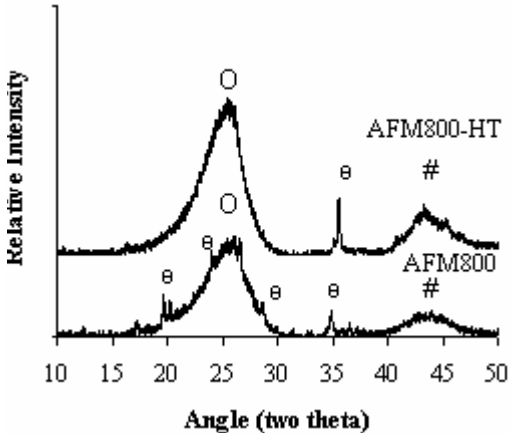

(e)

Figure A- 3: X-ray diffraction spectra of the 5 coal samples (a to e) with and without the thermal anneal. The samples with a thermal anneal have been denoted by a 'HT' in their name. (O represents the [002] graphitic peak, #, the [10] peak and ɵ, the peaks due to the different minerals.

The initial plan for coal selection was to select two or more coals that differed in their ability to undergo structural changes. However, the complexities apparent in the TPO and XRD studies suggested that variation of the coal would lead to complexity in subsequent ball milling studies. Therefore, it was decided that one coal would be chosen for the study. Demineralized Summit and its heat treated analog (DS-HT) were chosen for the following studies. The reasons for this choice are as follows: (1) Summit anthracite was readily available and previously characterized by Pappano [63]; (2) the mineral matter of Summit was easily removed via demineralization (from 18.6 to 1.2 %); (3) the TPO profiles of DS vs. DS-HT suggested a high reactivity upon thermal annealing and further suggested the ability of DS to 'graphitize'; (4) the TPO and XRD results of Summit compared to Summit-HT suggested that the carbon structures included in this coal readily formed carbides during heating.

Sample Preparation

The samples were prepared in the following order and the same ball milling equipment (bowl and balls) was used throughout the series of the samples: G-80-CH, DS-80-CH, DS-HT-80-CH, DS-80, DS-160-CH, DS-20-CH, DS-80-CH (<) and the final sample prepared was DS-80-CH (<).

The samples were collected from the Ball Mill in an inert atmosphere into two vials. One of them was sealed and stored at a temperature of ~ 5 ºC for TGMS tests to be performed whenever the equipment was available. The second vial was used for the other characterization tests. The TGMS tests were performed on the ball milled samples roughly around twelve months after the preparation of the samples. However the due to technical difficulties, the sealed vials were opened 3-4 months before the TGMS tests were performed.

Appendix B

Profile fitting of the XRD spectra

DS-80-CH

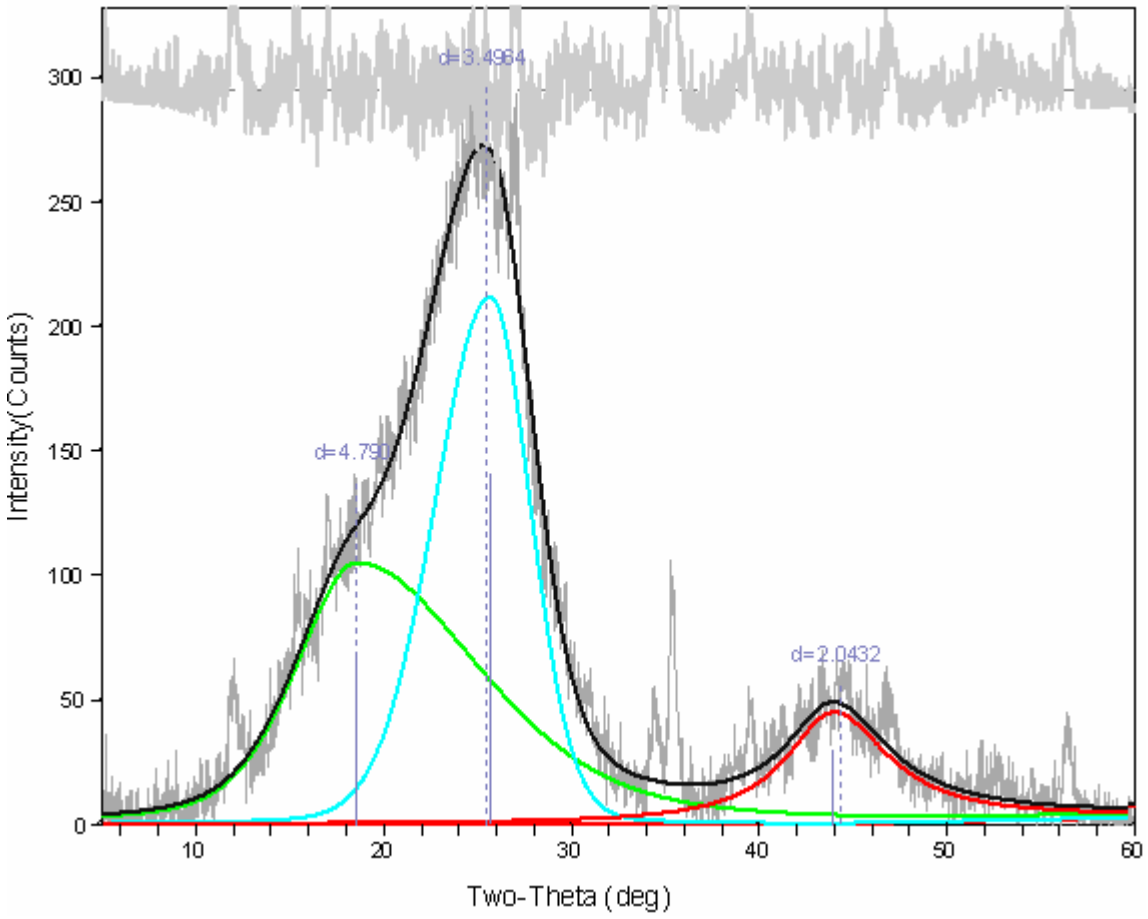

Figure B- 1: Profile fitting of the XRD peaks

The XRD profiles were fitted using the software JADE + Version 8.0. Following the work presented by Lu et al. [66], the [002] peak was fitted for the presence of two peaks whenever an asymmetry was seen as shown in Figure B- 1. The peak ~ $2\theta = 20°$ has been attributed to the presence of a gamma (γ) phase which is associated with the packing distance of saturated structures such as aliphatic side chains

Appendix C

TPO of the raw coal (BMT) and demineralized BMT (DBMT)

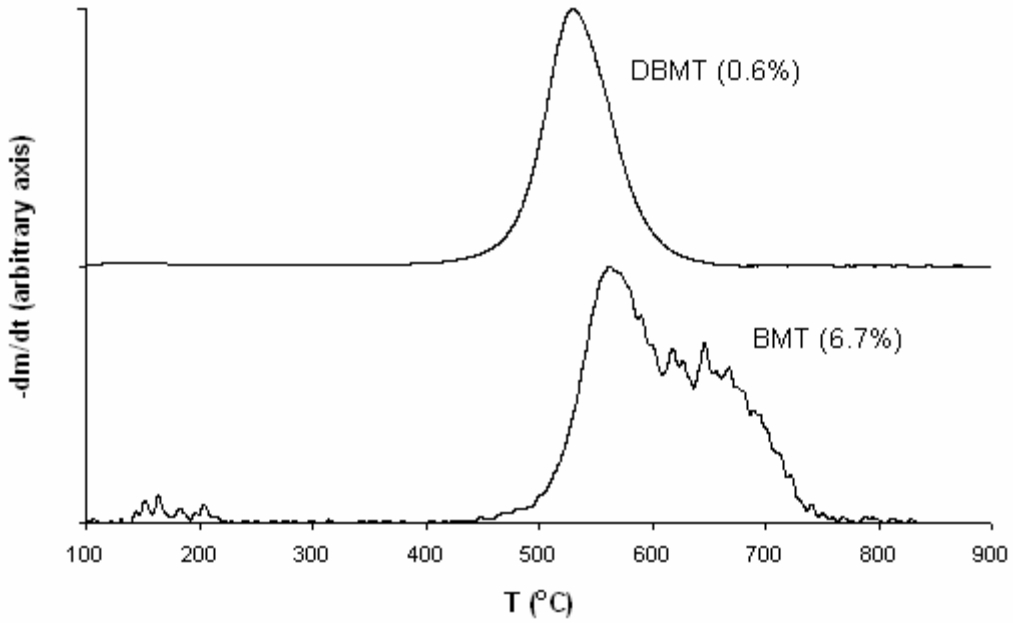

Figure C- 1: Temperature Programmed Oxidation profile of BMT and demineralized BMT (DBMT)

Demineralization of BMT led to a decrease in the ash content from 6.7% (for BMT) to 0.6% (for DBMT). This was accompanied by an increase in the reactivity of the coal. The oxidation profile in the case of BMT displays multiple split peaks which are in the range of 570ºC to 670ºC. Demineralization leads to a uniform peak at 535 ºC. The amorphous carbon in the range of 100-200 ºC is also absent in the case of DBMT.

Appendix D

Analytical report of the de-ionized water

The following (Table D- 1) is the spectrochemical analysis report of the de-ionized water used in Project 1 (on structural transformations). A relatively high concentration of calcium is evident. This suggests that the observation of calcite in the XRD results of the samples is due to this high presence of calcium in the water. This water was used to prepare the NaOH solution of the correct strength.

Table D- 1: Spectrochemical analysis of the de-ionized water

Species	Ba	Ca	Fe	K	Mg	Na	Sr	Mn	Si
Concentration (ppm)	<0.02	31	<0.02	1.3	18	20	<0.02	<0.02	5.1

The samples were run on a Leeman Labs PS3000UV ICP (inductively coupled plasma emission spectrometer) by Henry Gong at the Materials Characterization Lab. of the Materials Research Institute. Synthethic standards from High Purity Standards were used to calibrate the results. Results in parts per million on an as-received basis.

Appendix E

TPO of FeC

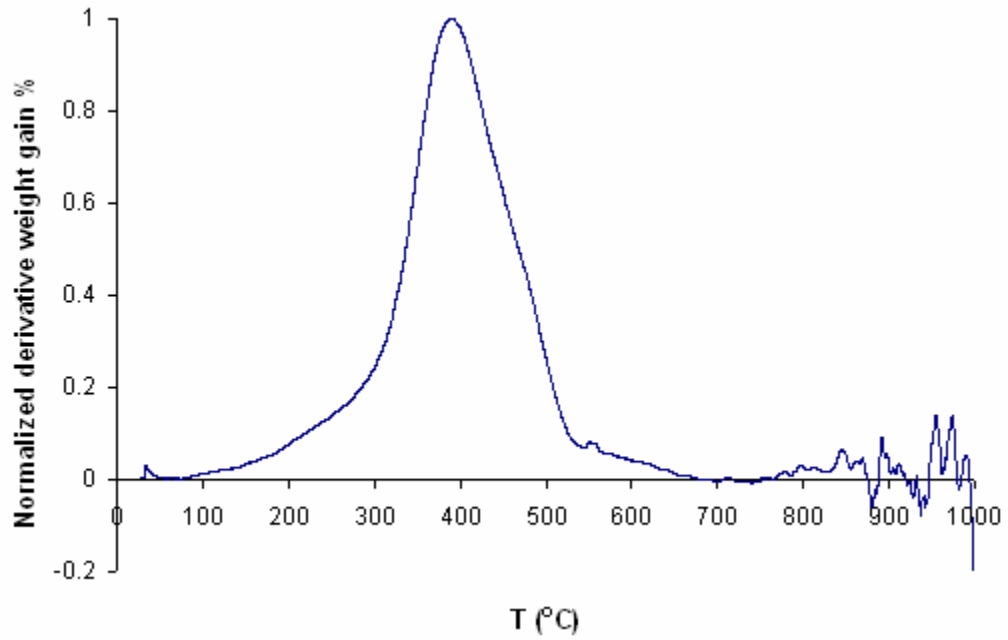

Figure E- 1: Temperature Programmed Oxidation (TPO) profile of Iron Carbide

The TPO curve of iron carbide shown in Figure E- 1shows that there is a net weight gain (31.8 wt %) of iron carbide upon oxidation unlike the coal samples which result in a net loss of weight. This can be due to the formation of iron oxides thereby resulting in a net increase in the molecular weight. The temperature of oxidation was seen to peak around 400 °C an the peak spread from ~ 100 °C to 675 °C.

UV-Raman of FeC (244nm)

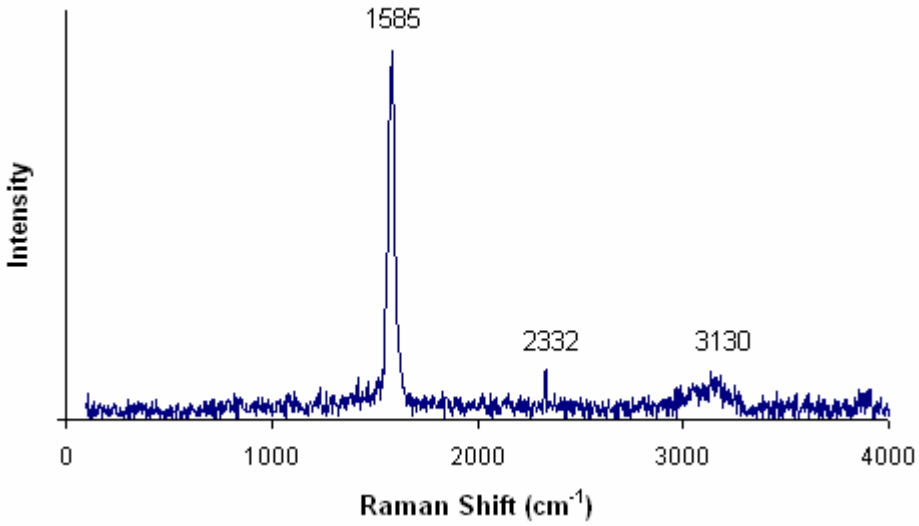

Figure E- 2: 244nm UV Raman spectra of Iron Carbide

UV Raman spectra of Iron Carbide at 244nm shows the presence of a G peak at ~ 1585 cm^{-1}, the second order reflection of the G peak at ~ 3130 cm^{-1} and the nitrogen peak at ~ 2330 cm^{-1}.

Appendix F

XRD analysis with Jade 8

The species were identified using the software Jade, version 8 as explained in Chapter 3 on Experimental Methods. To help with the identification process, the species which were expected to be present like iron, carbon, nickel, chromium etc. were often pre-selected to facilitate the characterization process. However the analysis was also done without any candidates pre-selected so that the software was able to search the entire database. All of the spectra were corrected for equipment error as mentioned in Chapter 3. Figures F 1-3 show the preparation sequence of the different samples of the study other than those of mBMT series which have been presented in Figure 4- 1. A list of the compounds (Table F- 1) that were identified in the samples has been included along with the XRD spectra of BMT and DBMT. A blown up image of the '-HT' samples in the 2θ range of 40-50º has been included to show the resemblance of mBMT-HT with mDBMT-SS-HT.

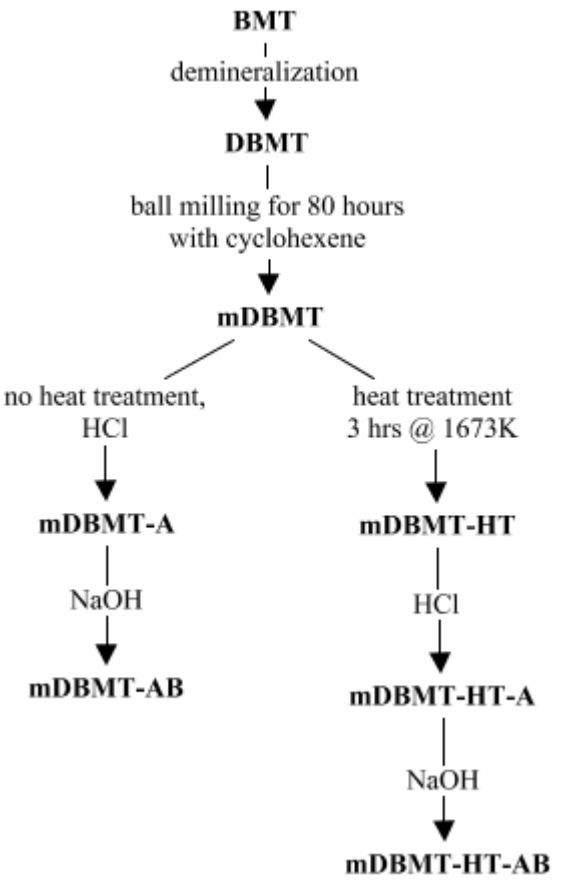

Figure F- 1: Preparation of the samples with the demineralized BMT anthracite coal, mDBMT series.

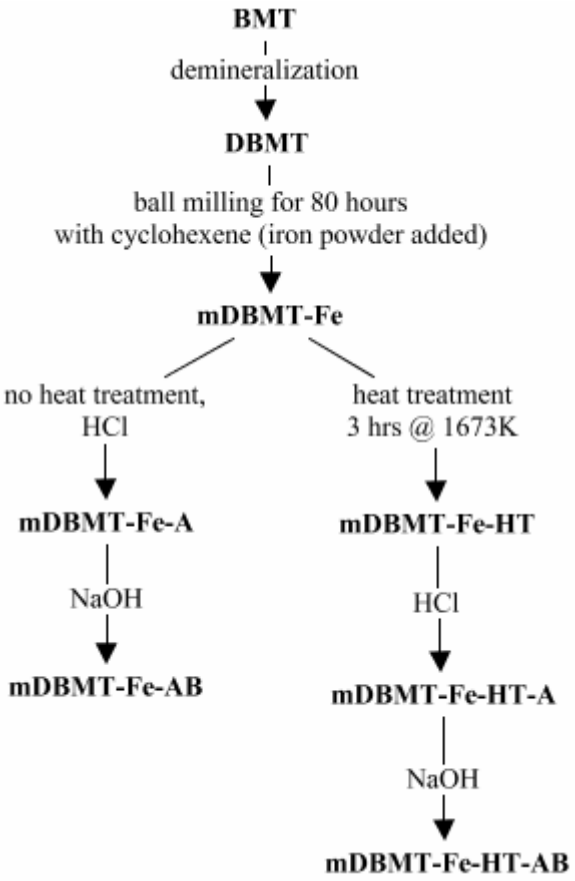

Figure F- 2: Preparation sequence of the samples with demineralized BMT coal ball milled with cyclohexene for 80 hours with iron powder (mDBMT-Fe)

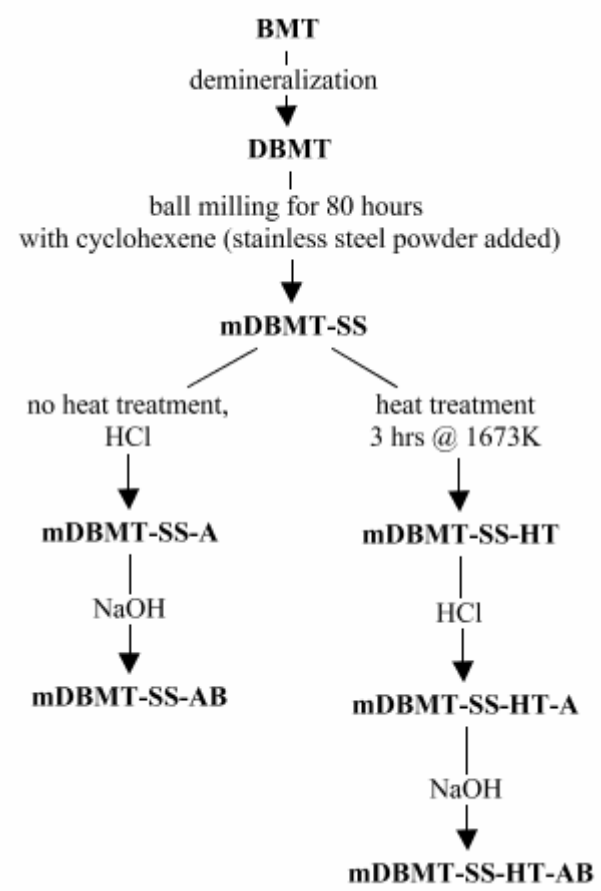

Figure F- 3: Preparation sequence of the samples with demineralized BMT coal ball milled with cyclohexene for 80 hours with stainless steel powder (mDBMT-SS)

Table F- 1: Reference Numbers of the compounds identified with JADE

Sample	Reference Numbers of the identified Compounds
mBMT	04-004-2474
mBMT-A	97-004-4724, 97-003-9175
mBMT-AB	01-083-1762, 97-002-3445
mBMT-HT	06-006-0686, 04-003-5514, 03-065-7251, 04-004-8327, 04-003-2430, 04-002-7519
mBMT-HT-A	03-065-4664, 03-065-7752, 00-017-0333
mBMT-HT-AB	97-001-6941, 97-006-8680, 04-003-2411
mDBMT	04-003-0399, 04-008-8265, 04-002-1483
mDBMT-A	04-008-8265, 00-044-1290
mDBMT-AB	97-003-0486, 97-002-3445
mDBMT-HT	04-008-1991, 99-003-1403, 01-076-1877
mDBMT-HT-A	97-002-7998, 98-000-0057
mDBMT-HT-AB	97-001-6941, 01-089-2867, 00-005-0586
mDBMT-Fe	97-003-7655, 04-003-5068, 03-065-7752
mDBMT-Fe-A	00-044-1290
mDBMT-Fe-AB	97-005-9629, 00-005-0586
mDBMT-Fe-HT	04-008-1991, 01-089-2867, 04-002-8935
mDBMT-Fe-HT-A	97-002-7998, 98-000-0057, 97-003-3283
mDBMT-Fe-HT-AB	97-000-0548, 99-000-0796, 00-044-1292
mDBMT-SS	04-006-0191, 03-065-7775
mDBMT-SS-A	00-041-1487, 00-037-0999
mDBMT-SS-AB	01-072-1652, 00-041-1487
mDBMT-SS-HT	04-002-1032, 04-006-2180, 03-065-9130, 04-002-1061, 04-003-2411, 00-046-1200, 00-017-0333
mDBMT-SS-HT-A	04-004-5110, 06-006-0686, 97-004-1168
mDBMT-SS-HT-AB	97-002-3445, 01-083-0578, 01-089-1304

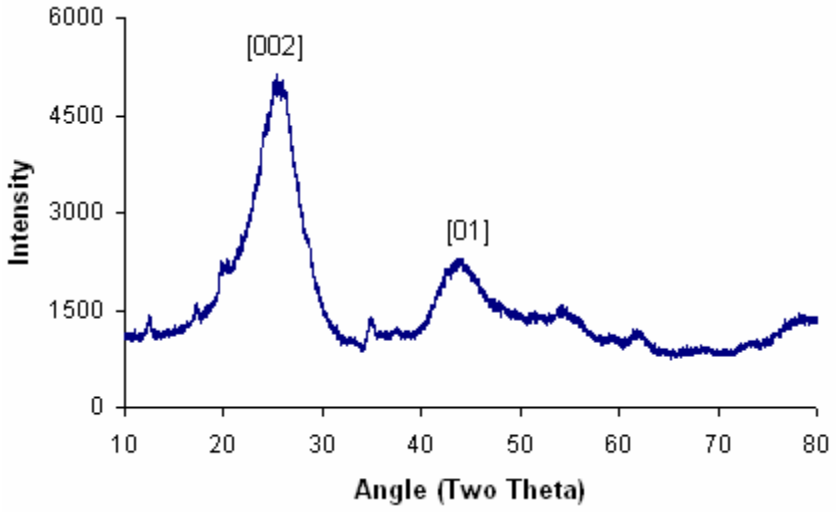

Figure F- 4: XRD for BMT anthracite coal, as received (from *Narayanan, D.L., The Pennsylvania State University, Masters Thesis, 2006* [32])

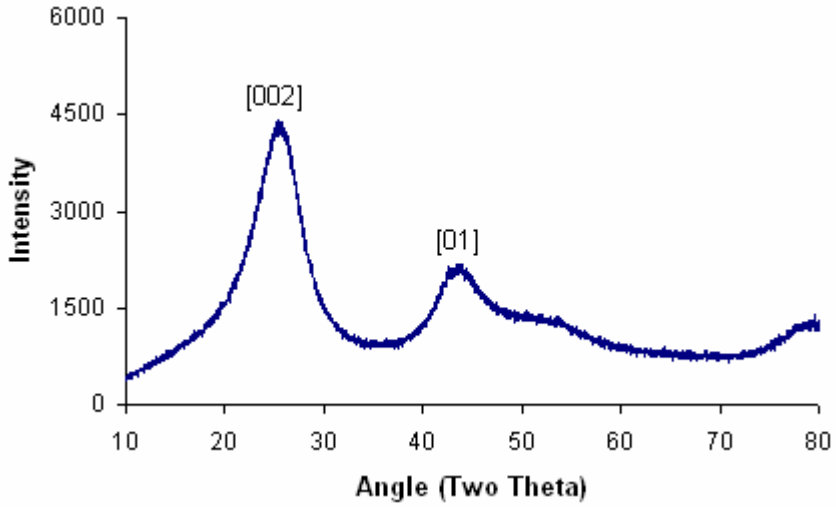

Figure F- 5: XRD for demineralized BMT anthracite coal (DBMT)

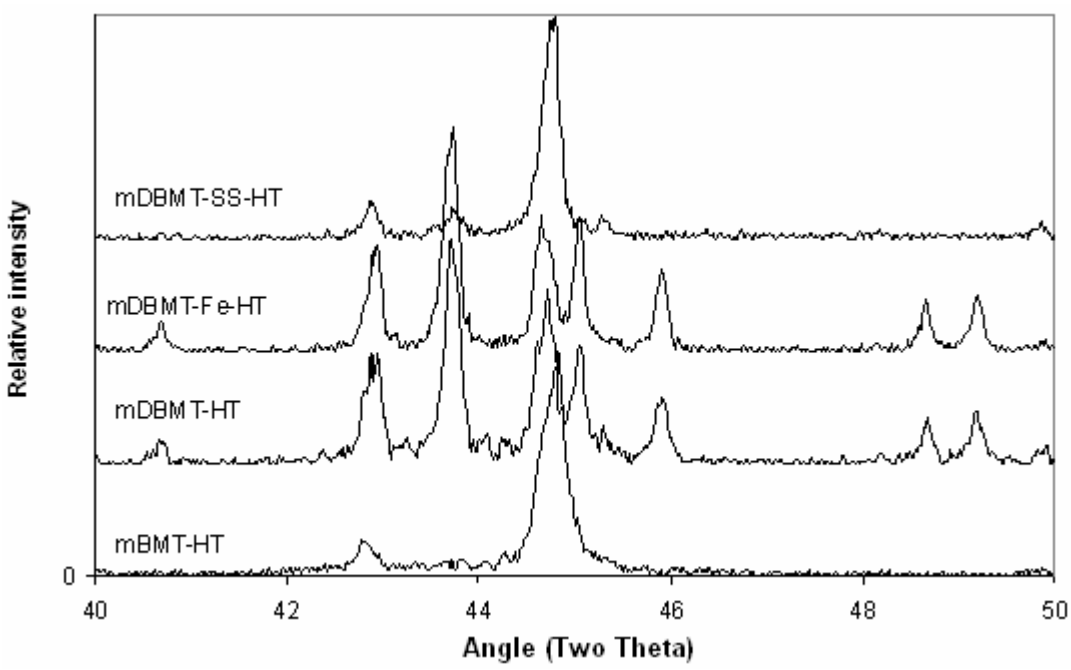

Figure F- 6: XRD of the four different ball milled samples after a thermal anneal in the region of 40-50°. mBMT-HT is seen to resemble mDBMT-SS-HT.

Appendix G

TGMS results of the samples

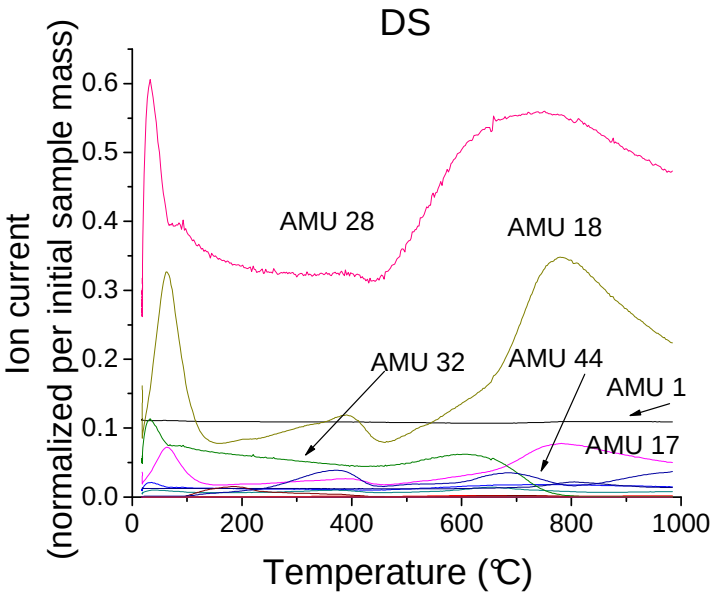

(a)

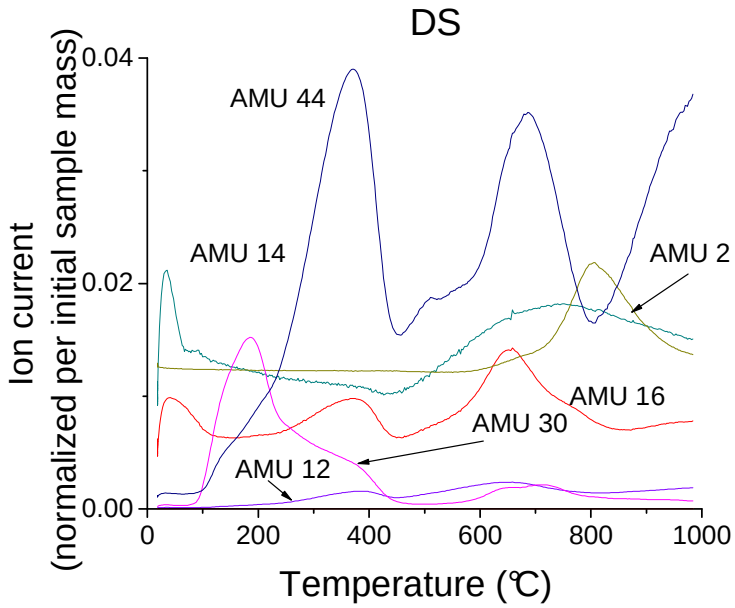

(b)

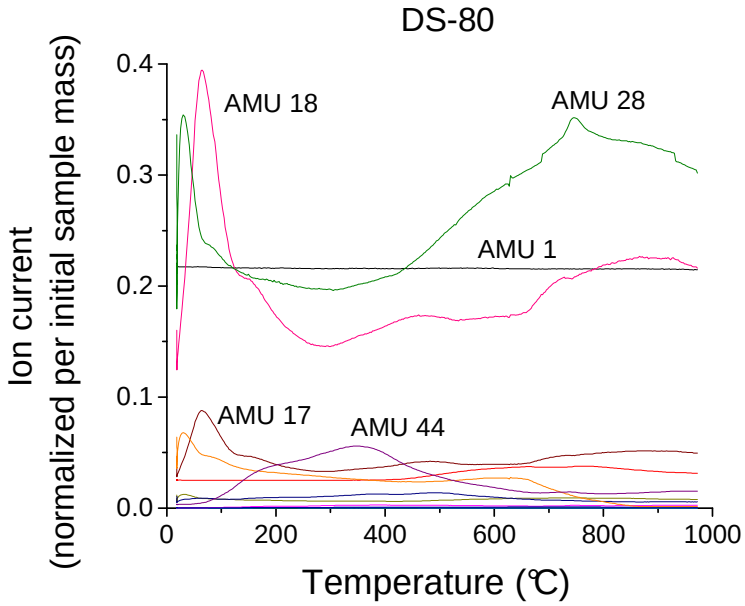
DS-80
Ion current
(normalized per initial sample mass)
0.4
0.3
0.2
0.1
0.0
AMU 18
AMU 28
AMU 1
AMU 17
AMU 44
0
200
400
600
800
1000
Temperature (℃)

(c)

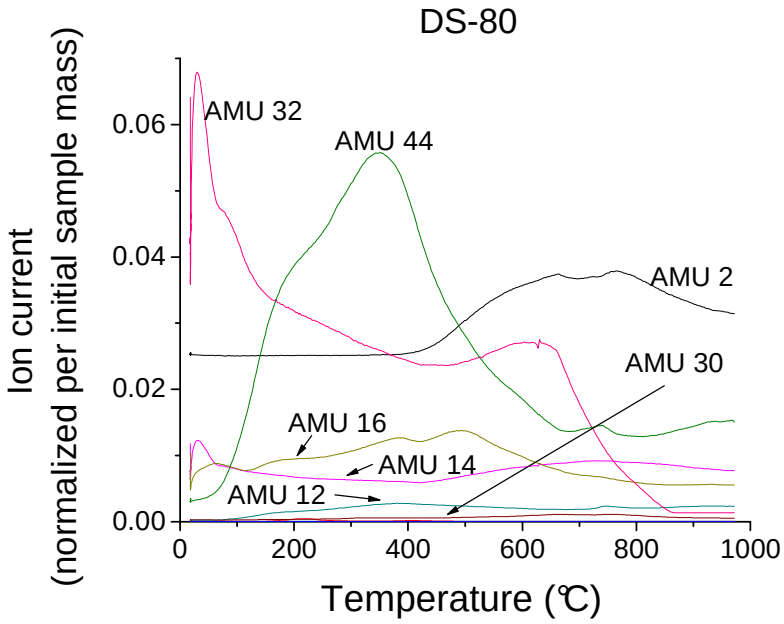
DS-80
Ion current
(normalized per initial sample mass)
0.06
0.04
0.02
0.00
AMU 32
AMU 44
AMU 2
AMU 30
AMU 16
AMU 14
AMU 12
0
200
400
600
800
1000
Temperature (℃)

(d)

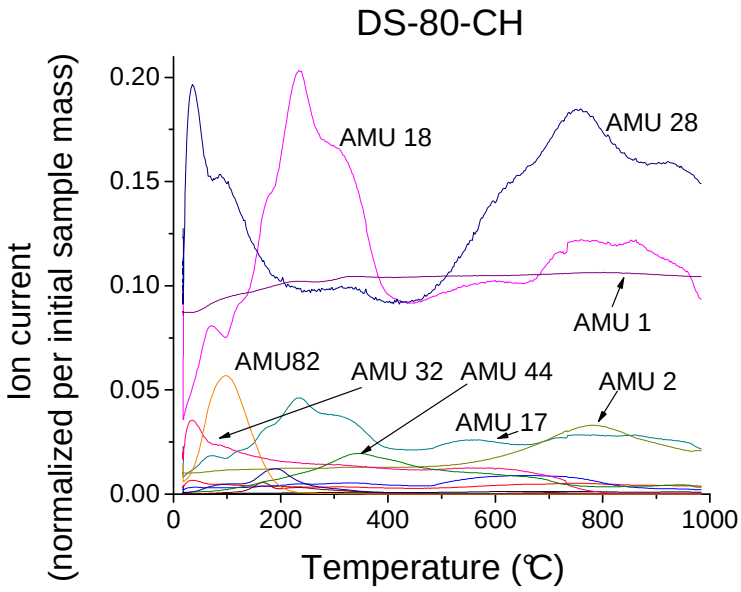
DS-80-CH
Ion current
(normalized per initial sample mass)
0.20
0.15
0.10
0.05
0.00
0
200
400
600
800
1000
Temperature (℃)
AMU 18
AMU 28
AMU 1
AMU82
AMU 32
AMU 44
AMU 2
AMU 17

(e)

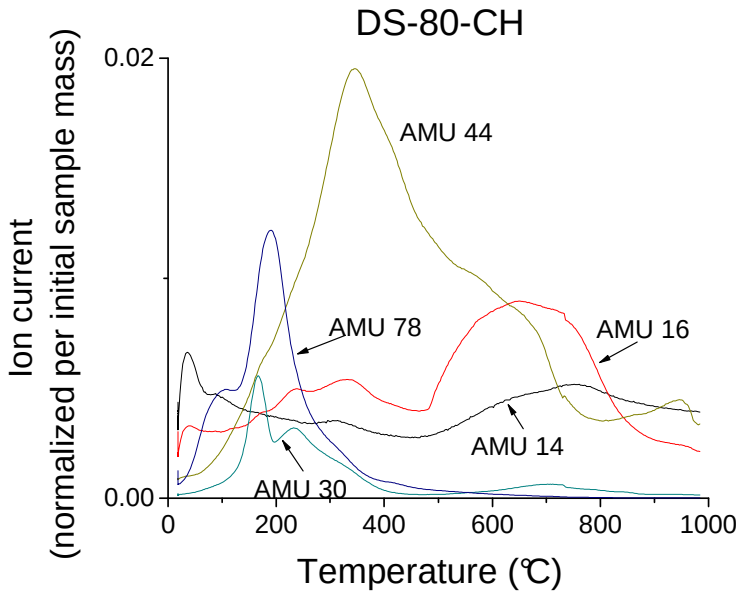
DS-80-CH
Ion current
(normalized per initial sample mass)
0.02
0.00
0
200
400
600
800
1000
Temperature (℃)
AMU 44
AMU 78
AMU 16
AMU 14
AMU 30

(f)

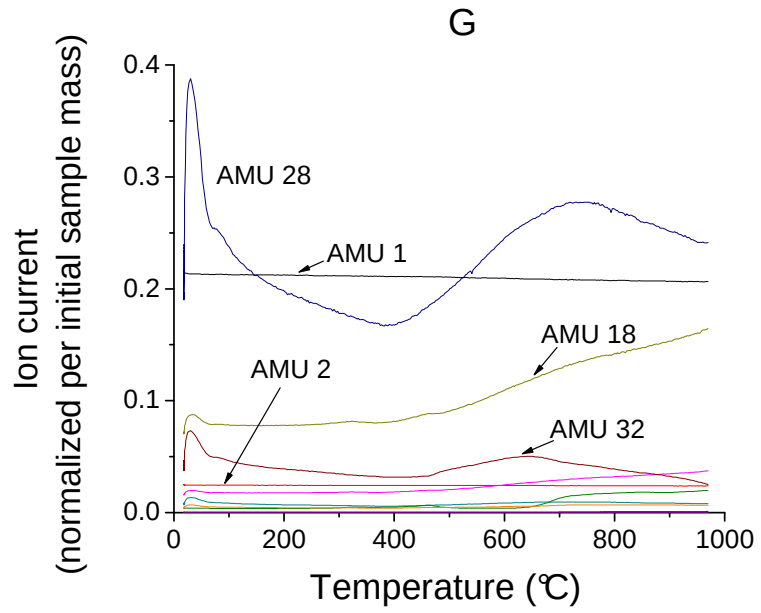
G
Ion current
(normalized per initial sample mass)
0.4
0.3
0.2
0.1
0.0
AMU 28
AMU 1
AMU 18
AMU 2
AMU 32
0
200
400
600
800
1000
Temperature (℃)

(g)

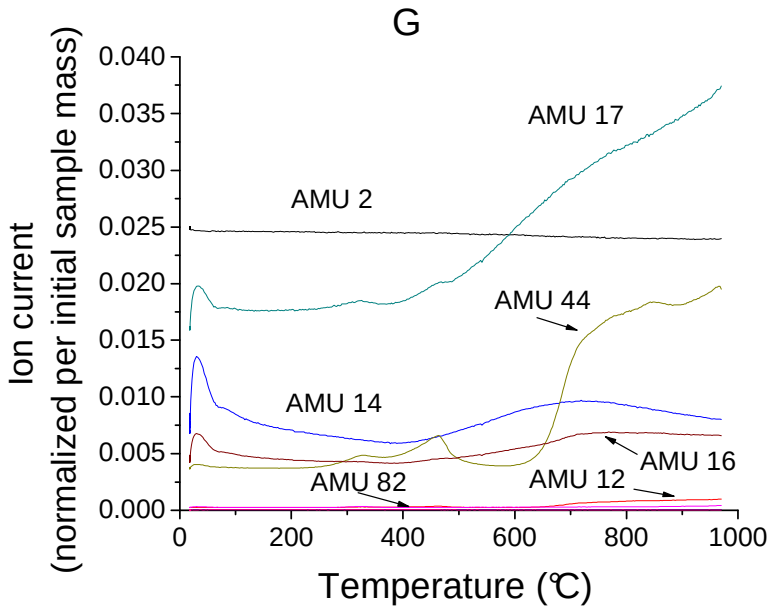
G
Ion current
(normalized per initial sample mass)
0.040
0.035
0.030
0.025
0.020
0.015
0.010
0.005
0.000
AMU 17
AMU 2
AMU 44
AMU 14
AMU 16
AMU 82
AMU 12
0
200
400
600
800
1000
Temperature (℃)

(h)

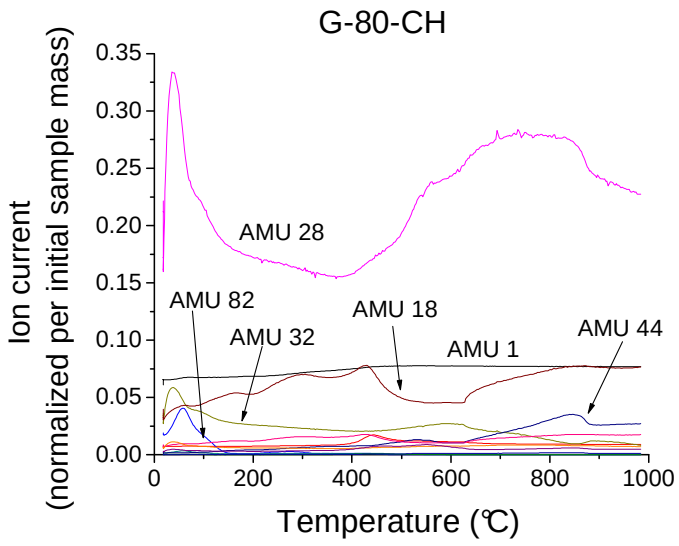

(i)

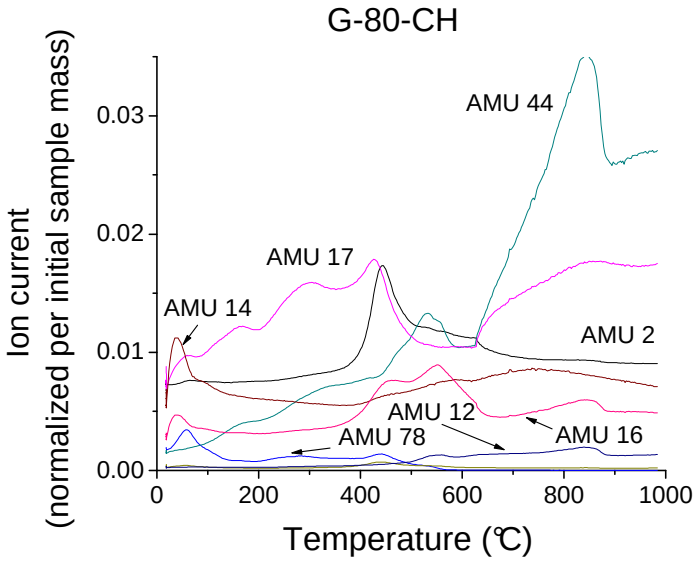

(j)

Figure G- 1: Thermo-gravimetric mass spectrometry results (TGMS) of the samples DS (a,b), G (c,d), DS-80 (e,f) DS-80-CH (g,h) and G-80-CH (i,j). Figures (b), (d), (f), (h) and (j) are plotted to zoom in on the signals with low ion currents. Ion signals for AMU 1 (hydrogen atom), AMU 2 (hydrogen molecule), AMU 14 (nitrogen atom), AMU 16 (oxygen atom), AMU 17 (hydroxyl ion), AMU 18 (water), AMU 28 (nitrogen molecule), AMU 30 (carbon monoxide), AMU 32 (oxygen molecule), AMU 44 (carbon dioxide), AMU 78 (benzene), AMU 82 (cyclohexene) have been plotted.

Bibliography

1. Lueking, A.D., et al., *Combined Hydrogen Production and Storage with Subsequent Carbon Crystallization.* J. Am. Chem. Soc., 2006. **128**(24): p. 7758-7760.
2. *DOE Annual Energy Outlook.* Available online at: http://www.eia.doe.gov/oiaf/aeo/ , last accessed 6th August, 2007, 2007.
3. *DOE Office of Science Basic Research Needs for the Hydrogen Economy.* Available online at: http://www.sc.doe.gov/bes/hydrogen.pdf, last accessed 6th August 2007.
4. *DOE Office of Energy Efficiency and Renewable Energy Hydrogen, Fuel Cells and Infrastructure technologies Program Multi-Year Research, Development and Demonstration Plan. Available online at* http://www.eere.energy.gov/hydrogenandfuelcells/mypp, last accessed 6th August, 2007, 2007.
5. *DOE Hydrogen Program Posture Plan.* Available online at: http://www.hydrogen.energy.gov/pdfs/hydrogen_posture_plan.pdf, last accessed 6th August 2007.
6. *Inventory of U.S. Greenhouse Gas Emissions and Sinks: 1990-2005, USEPA #430-R-07-002.* Available online at: http://www.epa.gov/climatechange/emissions/usinventoryreport.html last accessed 7th August 2007, April 2007.
7. *Pricewaterhouse Coopers, 2006 Fuel Cell Industry Survey,* Available online at: *http://www.pwc.com/extweb/pwcpublications.nsf/docid/25582836BD5E736A852570CA00178BC7, last accessed 7th August 2007.* 2006.
8. *U.S. DOE National Hydrogen Roadmap.* Available online at: *http://www.hydrogen.energy.gov/pdfs/national_h2_roadmap.pdf last accessed August 8, 2007.*
9. *International Energy Agency Report on 'Hydrogen Production and Storage-R&D Priorities and Gaps.* Available online at: *http://www.ieahia.org/pdfs/Hydrogen_Gaps_and_Priorities.pdf, last accessed August 8, 2007.* 2006.

10. Sastri, M.V.C., B. Viswanathan, and S. Srinivasa Murthy, *Metal hydrides - fundamentals and applications.* Narosa Publishing House, India, 1998: p. 189.
11. Dillon, A.C., et al., *Storage of hydrogen in single-walled carbon nanotubes.* Nature, 1997. **386**: p. 377-379.
12. Hirscher, M., et al., *Hydrogen storage in sonicated carbon materials.* Applied Physics A, 2001. **72**: p. 129.
13. Lueking, A.D. and R.T. Yang, *Hydrogen storage in carbon nanotubes: residual metal content and pretreatment temperature.* AICHE Journal, 2003. **49**: p. 1556.
14. Lueking, A.D. and R.T. Yang, *Hydrogen spillover from a metal oxide catalyst onto carbon nanotubes-implications for hydrogen storage.* Journal of Catalysis, 2002. **206**: p. 165.
15. Lueking, A.D., et al., *The effect of HCl and NaOH treatment on structural transformations in a ball-milled anthracite after thermal and chemical processing.* Carbon, 2007. **45**(11): p. 2297-2306.
16. Jain, P., *Catalyzed Nanocarbons for Hydrogen Storage: Experimental and Theoretical Study of the Spillover Phenomenon, PA, USA: The Pennsylvania State University, MS Thesis, 2006.*
17. Ichikawa, T., et al., *Hydrogen storage properties on mechanically milled graphite.* Materials Science and Engineering B, 2004. **108**(1-2): p. 138-142.
18. Orimo, S., et al., *Hydrogen desorption property of mechanically prepared nanostructured graphite*. 2001, AIP. p. 1545-1549.
19. Hirscher, M., et al., *Are carbon nanostructures an efficient hydrogen storage medium?* Journal of Alloys and Compounds, 2003. **356-357**: p. 433-437.
20. Hirscher, M., et al., *Hydrogen storage in carbon nanostructures.* Journal of Alloys and Compounds, 2002. **330-332**: p. 654-658.
21. Maurice, D.R. and T.H. Courtney, *The Physics of Mechanical Alloying: A First Report.* Metallurgical Transactions A, 1990. **21A**: p. 289-303.
22. Eckert, J., et al., *Structural and thermodynamic properties of nanocrystalline FCC metals prepared by mechanical attrition.* Journal of Materials Research 1992. **7**(7): p. 1751-1761.

23. Chen, X.H., et al., *Generation of curved or closed-shell carbon nanostructures by ball-milling of graphite.* Journal of Crystal Growth, 2000. **218**(1): p. 57-61.
24. Fecht, H.J., et al., *Nano-crystalline materials prepared by high-energy ball milling.* Metallurgical Transactions A-Physical Metallurgy and Materials Science, 1990. **21**(9): p. 2333-2337.
25. Fukunaga, T., et al., *Structural change of graphite subjected to mechanical milling.* Journal of Non-Crystalline Solids, 1998. **234**: p. 416-420.
26. Salver-Disma, F., et al., *Transmission electron microscopy studies on carbon materials prepared by mechanical milling.* Carbon, 1999. **37**(12): p. 1941-1959.
27. Shen, T.D., et al., *Structural disorder and phase transformation in graphite produced by ball milling.* Journal of Nanostructured Materials, 1996. **7**(4): p. 393-399.
28. Janot, R. and D. Guerard, *Ball-milling: the behavior of graphite as a function of the dispersal media.* Carbon, 2002. **40**(15): p. 2887-2896.
29. Janot, R. and D. Guerard, *Ball-milling in liquid media: Applications to the preparation of anodic materials for lithium-ion batteries.* Progress in Materials Science, 2005. **50**(1): p. 1-92.
30. Ong, T.S. and H. Yang, *Effect of atmosphere on the mechanical milling of natural graphite.* Carbon, 2000. **38**(15): p. 2077-2085.
31. Narayanan, D.L. and A.D. Lueking, *Mechanically milled coal and magnesium composites for hydrogen storage.* Carbon, 2007. **45**: p. 805-820.
32. Narayanan, D.L., *Exploratory Study of Exfoliated Graphite Nanofibers and Milled Anthracite-Metal Composites for Hydrogen Storage, PA, USA, The Pennsylvania State university, Masters Thesis, 2006.*
33. Imamura H, et al., *Hydriding–dehydriding behavior of magnesium composites obtained by mechanical grinding with graphite carbon.* International Journal of Hydrogen Energy, 2000. **25**(9): p. 837–843.
34. Rouquerol, F., J. Rouquerol, and K. Sing, *Adsorption by powders and porous solids: principles, methodology and applications.* Academic Press, 1999: p. 467.

35. Jeloaica, L. and V. Sidis, *DFT investigation of the adsorption of atomic hydrogen on a cluster-model graphite surface.* Chemical Physics Letters, 1999. **300**(1-2): p. 157-162.
36. Letardi, S., et al., *Atomic hydrogen adsorption on a Stone-Wales defect in graphite.* Surface Science, 2002. **496**(1-2): p. 33-38.
37. Orimo, S., et al., *Hydrogen interaction with carbon nanostructures: current situation and future prospects.* Journal of Alloys and Compounds, 2003. **356-357**: p. 716-719.
38. J., B.D., et al., *Studies into the storage of hydrogen in carbon nanofibers: proposal of a possible reaction mechanism.* Nanoletters, 2002. **2**: p. 201.
39. Chen, J. and F. Wu, *Review of hydrogen storage in inorganic fullerene-like nanotubes.* Applied Physics A: Materials Science & Processing, 2004. **78**(7): p. 989-994.
40. Orimo, S., et al., *Hydrogen in the mechanically prepared nanostructured graphite.* Applied Physics Letters, 1999. **75**(20): p. 3093-3095.
41. Orimo, S., et al., *Hydrogen desorption property of mechanically prepared nanostructured graphite.* Journal of Applied Physics, 2001. **90**(3): p. 1545-1549.
42. Shindo, K., T. Kondo, and Y. Sakurai, *Dependence of hydrogen storage characteristics of mechanically milled carbon materials on their host structures.* Journal of Alloys and Compounds, 2004. **372**(1-2): p. 201-207.
43. Narayanan, D.L. and A.D. Lueking, *Mechanically milled coal and magnesium composites for hydrogen storage.* Carbon, 2007. **45**(4): p. 805-820.
44. Imamura, H., et al., *Carbon nanocomposites synthesized by high-energy mechanical milling of graphite and magnesium for hydrogen storage.* Acta Materialia, 2003. **51**(20): p. 6407-6414.
45. Atria, J.V., F. Rusinko, and H.H. Schobert, *Structural Ordering of Pennsylvania Anthracites on Heat Treatment to 2000-2900 C*. 2002. p. 1343-1347.
46. Schobert, H.H., *The chemistry of hydrocarbon fuels.* Butterworths, 1990: p. 348.
47. Hirsch, P.B., *X-Ray Scattering from Coals.* Proceedings of the Royal Society of London. Series A, Mathematical and Physical Sciences, 1954. **226**(1165): p. 143-169.

48. Schobert, H.H. and F.J. Rusinko, *Novel approach to the production of anthracite from graphite.* First Quarterly Report, PEDA Grant No. 9103-4019, Dec. 1992.
49. Atria, J.V., *Novel approach to the production of graphite from anthracite.* Masters Thesis, The Pennsylvania State University, 1995.
50. (IUPAC), I.U.o.P.a.A.C., *Manual of Symbols and Terminology for Physico Chemical Quantities and Units.* Butterworth, London, 1972.
51. Iino, M., *Network structure of coals and association behavior of coal-derived materials.* Fuel Processing Technology, 2000. **62**: p. 89-101.
52. Takanohashi, T., M. Iino, and M. Nishioka, *Investigation of Associated Structure of Upper Freeport Coal by Solvent Swelling.* Energy and Fuels, 1995. **9**: p. 788-793.
53. Iino, M., et al., *Extraction of Coals with Cs2-N-Methyl-2-Pyrrolidinone Mixed-Solvent at Room-Temperature - Effect of Coal Rank and Synergism of the Mixed-Solvent.* Fuel, 1988. **67**(12): p. 1639-1647.
54. Larsen, J.W., et al., *A Method for Counting the Hydrogen-Bond Cross-Links in Coal*. 1996. p. 1269-1272.
55. Painter, P.C., *Some Comments on the Paper of Larsen et al. and the Nature of Cross-Linking in Coal*. 1996. p. 1273-1275.
56. van Krevelen, D.W., *Coal Typology-Chemistry-Physics-Constitution.* Elsevier Scientific, New York, 1981.
57. Franklin, R.E., *Crystallite growth in graphitizing and non-graphitizing carbons.* Proceedings of the Royal Society of London. Series A, Mathematical and Physical Sciences, 1951. **209**(1097): p. 196-218.
58. Lueking, A.D., et al., *The effect of HCl and NaOH treatment on structural transformations in a ball-milled anthracite after thermal and chemical processing.* in press.
59. Francke, M., et al., *Modification of carbon nanostructures by high energy ball-milling under argon and hydrogen atmosphere.* Carbon, 2005. **43**(6): p. 1204-1212.

60. Majer, G., E. Stanik, and S. Orimo, *NMR studies of hydrogen motion in nanostructured hydrogen-graphite systems.* Journal of Alloys and Compounds, 2003. **356-357**: p. 617-621.
61. Isobe, S., et al., *Catalytic effect of 3d transition metals on hydrogen storage properties in mechanically milled graphite.* Journal of Physics and Chemistry of Solids, 2004. **65**(2-3): p. 535-539.
62. Pennsylvania State University Coal Sample Bank Database, Available online at: (http://datamine.ei.psu.edu/sample_detail.php?sample_id=1468) last accessed August 2, 2007.
63. Pappano, P.J., *Graphitization Studies of Pennsylvania Anthracites.* Masters Thesis, The Pennsylvania State University, 2000.
64. Bishop, M. and D.L. Ward, *The direct determination of mineral matter in coal.* Fuel, 1958. **37**: p. 191 - 200.
65. Chiang, I.W., et al., *Purification and Characterization of Single-Wall Carbon Nanotubes*. 2001. p. 1157-1161.
66. Lu, L., et al., *Quantitative X-ray diffraction analysis and its application to various coals.* Carbon, 2001. **39**(12): p. 1821-1833.
67. Bustin, R.M., J.N. Rouzaud, and J.V. Ross, *Natural graphitization of anthracite: Experimental considerations.* Carbon, 1995. **33**(5): p. 679-691.
68. Huang, H., et al., *Density measurements of Argonne Premium Coal Samples.* Energy and Fuels, 1995. **9**(20-24).
69. Francke, M., et al., *Modification of carbon nanostructures by high energy ball-milling under argon and hydrogen atmosphere.* Carbon, 2005. **43**(6): p. 1204 - 1212.
70. Green, T.K., J. Kovac, and J.W. Larsen, *A rapid and convenient method for measuring the swelling of coals by solvents.* Fuel, 1984. **63**(7): p. 935-938.
71. Ravindran, T.R., B.R. Jackson, and J.V. Badding, *UV Raman spectroscopy of single-walled carbon nanotubes.* Chem. Mater., 2001. **13**: p. 4187-4191.
72. Villar, S.E.J. and H.G.M. Edwards, *Near-infrared Raman spectra of terrestrial minerals: relevance for the remote analysis of Martian spectral signatures.* Vibrational Spectroscopy, 2005. **39**(1): p. 88-94.

73. Dean, J.A., *Lange's Handbook of Chemistry (15th Edition)* 1999 McGraw Hill.
74. Ferrari, A.C. and J. Robertson, *Resonant Raman spectroscopy of disordered, amorphous, and diamondlike carbon.* Physical Review B, 2001. **64**(7): p. 075414.
75. Osswald, S., et al., *Control of sp(2)/sp(3) carbon ratio and surface chemistry of nanodiamond powders by selective oxidation in air.* Journal of Americal Chemical Society, 2006. **128**(35): p. 11635-42.
76. Ferrari, A.C. and J. Robertson, *Interpretation of Raman spectra of disordered and amorphous carbon.* Physical Review B, 2000. **61**(20): p. 14095-14107.
77. *Personal Communication.* Henry Gong to Angela D. Lueking, 19 March, 2008.
78. Ferrari, A.C. and J. Robertson, *Raman spectroscopy of amorphous, nanostructured, diamond-like carbon, and nanodiamond.* Philosphical Transactions of the Royal Society London A, 2004. **362**: p. 2477-2512.
79. Cody, G.D., J.W. Larsen, and M. Siakin, *Anisotropic Solvent Swelling of Coals.* Energy and Fuels, 1988. **2**: p. 340-344.
80. Suuberg, E.M., et al., *Coal Macromolecular Network Structure Analysis: Solvent Sweilling Thermodynamics and Its Implications.* Energy and Fuels, 1994. **8**: p. 1247-1262.
81. Nishioka, M., *Role of Solvation for Coal Swelling in Slurry.* Energy and Fuels, 2002. **16**: p. 1109-1115.
82. Milligan, J.B., K.M. Thomas, and J.C. Crelling, *Solvent Swelling of Maceral Concentrates.* Energy and Fuels, 1997. **11**: p. 364-371.
83. Flory, P.J., *Principles of polymer chemistry.* Ithaca, NY: Cornell University Press 1953.
84. Sperling, L.H., *Introduction to physical polymer science.* 2nd ed. New York: Wiley, 1992.
85. Takanohashi, T., et al., *Extraction and Swelling of Low-Rank Coals with Various Solvents at Room Temperature*. 1996. p. 1128-1132.
86. Polansky, T.S., H.J. Donald, and C.R. Kinney, *Structure of High-Rank Coals deduced from Helium Densities.* Nature, 1960. **186**(4727): p. 792-793.
87. Ergun, S. and V.H. Tiensuu, *Interpretation of the intensities of X-rays scattered by coals.* 1959. **38**: p. 64-78.

88. Casiraghi, C., A.C. Ferrari, and J. Robertson, *Raman spectroscopy of hydrogenated amorphous carbons.* Physical Review B (Condensed Matter and Materials Physics), 2005. **72**(8): p. 085401-14.
89. Chen, Y., et al., *Nanoporous carbon produced by ball milling.* Applied Physics Letters, 1999. **74**(19): p. 2782-2784.